2016

A Direct Study of 20Ne(alpha,p)23Na with the HELIcal Orbit Spectrometer (HELIOS)

Jianping Lai
Louisiana State University and Agricultural and Mechanical College

A direct study of ^{20}Ne(α,p)^{23}Na with the HELIcal Orbit Spectrometer (HELIOS)

A Dissertation

Submitted to the Graduate Faculty of the
Louisiana State University and
Agricultural and Mechanical College
in partial fulfillment of the
requirements for the degree of
Doctor of Philosophy

in

The Department of Physics and Astronomy

by
Jianping Lai
BS, Huazhong University of Science and Technology, 2010
August 2016

Acknowledgement

I received an exponentially scaled amount of support during my six year graduate study. The first data point of contribution is from my adviser, Catherine Deibel, not only because of her tremendous support and guidance over my research and study, also because of her kindness and patience in my thesis writing and in my impatience when experiments went wrong.

In addition to my advisor, Dr. Jeffrey Blackmon, Dr. Juhan Frank and Dr. Bradley Schaefer have given me invaluable suggestions. I also learnt a lot from Daniel and Melina. My colleague and also my good friend Kevin, has always helped my research and my beer selecting.

My thesis research was performed at Argonne National Laboratory and this work could not be finished without the help and advice from the ANL staff, including Calem Hoffman, Ernst Rehm, Birger Back and many others.

Finally, I can not thank my friends and families enough for their encouragement and believing. I give my special thanks to my girlfriend Chloe for prevent the thesis-writing from driving me mentally disordered. Without her, my computer could long be wrecked and this thesis would never be finished.

Table of Contents

List of Figures

List of Tables

Abstract

Type Ia Supernovae are thermonuclear explosions that occur on CO white dwarfs in binary systems, completely disrupting the system. While the exact progenitor of these events is unclear, there have been several studies exploring the nucleosynthesis that drives these stellar explosions. These studies have shown that a handful of reactions have a significant effect on Type Ia Supernova nucleosynthesis, specifically ^{12}C(α, γ), ^{12}C+^{12}C, ^{20}Ne(α, p), ^{20}Ne(α, γ), and ^{30}Si(p, γ).

While the ^{20}Ne(α,p)^{23}Na reaction has been shown to be one of the five most influential reactions, it has not been directly been measured at astrophysically relevant energies. We performed direct measurements of this reaction with multiple ^{20}Ne beam energies (100 MeV, 80 MeV and 31 MeV) in inverse kinematics.

The measurements were performed at Argonne National Laboratory using the HELIOS (HELIcal Orbit Spectrometer) beam line. This measurement is also a proof-of-principle test for a setup designed for reaction studies, using a cryogenic gas target and a fast position-sensitive ionization chamber (IC). This experimental setup especially targets reactions with radioactive ion beams and details of the commissioning runs for the gas target and the IC are discussed.

The data obtained was analyzed using a series of timing and particle identification cuts to determine the particle yields from the ^{4}He(^{20}Ne,p)^{23}Na reaction. Efficiencies were determined through a series of simulations using the Geant4 toolkit and the data were normalized using the ^{2}H(^{20}Ne,p)^{21}Ne and ^{4}He(^{20}Ne,^{4}He)^{20}Ne reactions. The yields were corrected for these efficiencies and normalized to determine the reaction cross section.

These newly measured cross sections are compared to the ones previously used for nuclear reaction sensitivity studies and the likely effects on Type Ia Supernova nucleosynthesis are discussed. Candidate reactions for future studies are listed and possible improvements are proposed.

Chapter 1
Introduction

1.1 Overview of Stellar Evolution

1.1.1 The Beginning of the Universe

It is generally agreed upon that the evolution of the universe started with immense energy at very high temperatures, where no particles existed: the Big Bang. Following this, the universe expanded and cooled. After less than a second, the temperature was low enough to allow the production of baryons, including protons and neutrons. Shortly thereafter the universe cooled even more and nuclear reactions could take place. This Big Bang Nucleosynthesis (BBN) [1] produced light elements up to ^{7}Be and ^{7}Li. Additional proton or neutron adding to ^{7}Be, produces only unstable isotopes, which immediately break apart resulting in a mass gap at A=8 (Fig. 1.1). This bottleneck can be bypassed by the triple-α process, which transforms three ^{4}He into ^{12}C. However this process is slow and requires higher temperatures and longer times than those present during BBN. Thus, the contribution to heavy nuclear elements is limited within minutes after the Big Bang. Additionally, ^{7}Be is unstable, and decays into ^{7}Li within days after formation. Thus, light elements up to ^{7}Li, and the lack of heavy elements are signatures of Big Bang Nucleosynthesis.

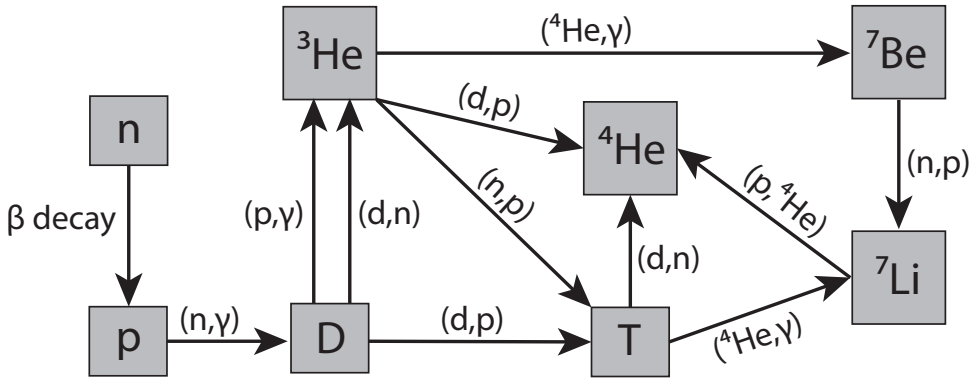

Figure 1.1: Schematic of reactions occurring during Big Bang nucleosynthesis. This figure is reproduced from [1].

1.1.2 Stellar Evolution

Most of the content in this section can be found in elementary astrophysics textbook such as Carroll et al. [1] and Iliadis et al. [2].

The interstellar gas and dust that formed as a result of BBN randomly coalesced into clouds. Once the size of a gas cloud surpasses the limit of the Jeans length :

$$R_j \simeq (\frac{15kT}{4\pi G\mu m_H \rho_0})^{1/2}, \tag{1.1}$$

where ρ_0 is the density of the cloud, m_H is the hydrogen molecular mass and μ is the mean molecular mass, the structure collapses. A more accurate limit, which includes the effects of external gas pressure, is given by the Bonnor-Ebert mass,

$$M_{BE} = \frac{c_{BE} v_T^4}{P_0^{1/2} G^{3/2}}, \tag{1.2}$$

where P_0 is the gas pressure, $v_T \equiv \sqrt{kT/\mu m_H}$ is the isothermal sound speed and $c_{BE} \simeq 1.18$ is a dimensionless constant.

This collapse forms a protostar, which is initially composed of hydrogen and helium. Once the energy created by gravitational contraction reaches a certain level, nuclear reactions are triggered (0.06 $M_\odot$ is enough to burn lithium and 0.013 $M_\odot$ for deuterium burning). However, the onset of nuclear reactions does not necessarily mean the start of main sequence evolution. For a protostar with mass less than 0.072 $M_\odot$, the energy produced by nuclear reactions is not strong enough to balance gravitational collapse and core temperatures do not become high enough to sustain hydrogen fusion, and the star ends up as a Brown Dwarf.

All main sequence stars begin with hydrogen burning. Depending on the initial mass, the major burning processes can be different. Most of the energy produced via nuclear processes in stars with masses less than 1.2 $M_\odot$ comes from the pp reaction chain, in which hydrogen fuses to ^{4}He through the series of reactions shown in Fig. 1.2. The chain is divided into sub-groups by the path of fusion into ^{4}He. Among all the reaction chains, the pp-1 and pp-2 branches contribute significantly more than the other possible sequences.

By contrast, in stars that form with enough metals and have initial masses higher than 1.3 $M_\odot$, the temperatures are higher and the CNO reaction cycle (Fig. 1.3) becomes the dominant proton fusion process, as this reaction cycle is highly temperature dependent and the rates of the CNO cycle reactions surpass those in the pp chain at higher temperatures. While the pp-chains and CNO cycles all fuse protons into ^{4}He, part of the CNO cycle also contributes to nuclear abundances of e.g. ^{13}C, ^{14}N.

After stars consume most of their hydrogen, the evolutionary track will again split, depending on the mass. If the mass of the star is not large enough to compress the core and reach the temperature necessary for ^{4}He burning (less than 0.5 $M_\odot$), the star will eventually exhaust hydrogen and become a helium white dwarf.

Stars with masses larger than $\sim$0.5 $M_\odot$ will go through the helium burning stage.

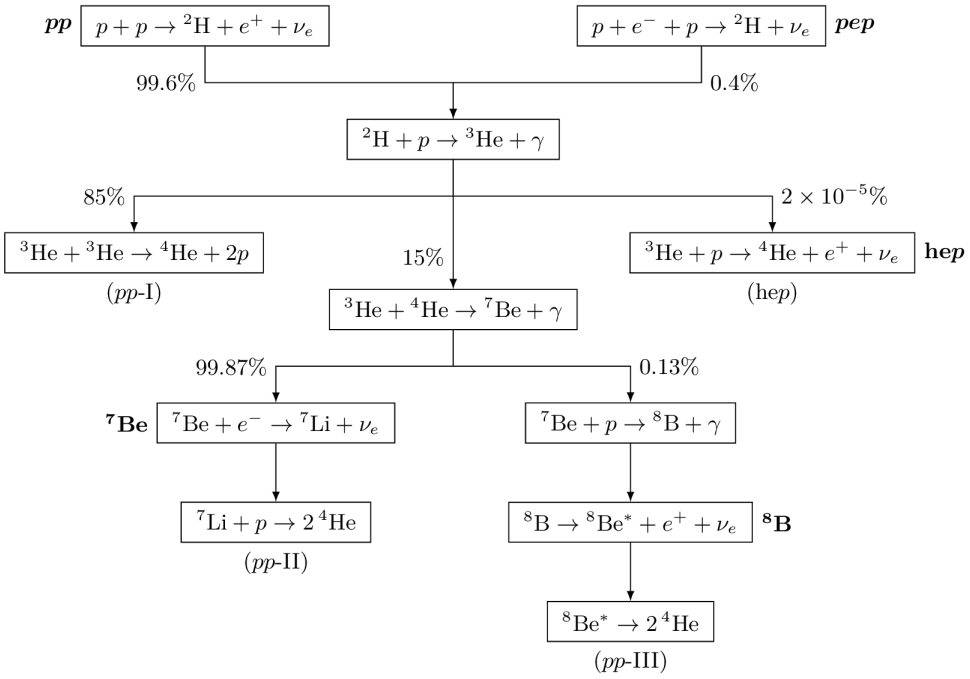

Figure 1.2: The nucleosynthesis schematic for the pp chains in the Sun, reproduced from [3].

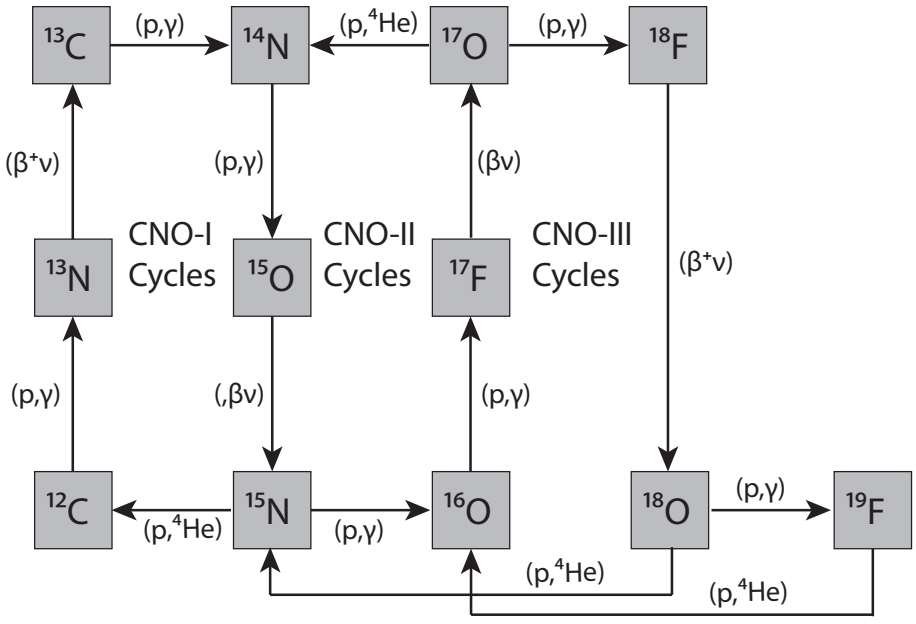

Figure 1.3: The nucleosynthesis schematic for the CNO cycles. Reproduced from [4].

Helium is mainly burned through the triple alpha process, which fuses alpha particles into ^{12}C:

$$^{4}_{2}\mathrm{He} +^{4}_{2} \mathrm{He} \rightarrow^{8}_{4} \mathrm{Be} \tag{1.3}$$

$$^{8}_{4}\mathrm{Be} +^{4}_{2} \mathrm{He} \rightarrow^{12}_{6} \mathrm{C}, \tag{1.4}$$

and the fusions of ^{12}C and ^{4}He into ^{16}O, which determines C to O ratio in the resulting CO core:

$$^{12}_{6}\mathrm{C} +^{4}_{2} \mathrm{He} \rightarrow^{16}_{8} \mathrm{O}. \tag{1.5}$$

For stars with masses less than 4 $M_\odot$ and larger than $\sim$0.5 $M_\odot$, the core of the star is formed from the ashes (carbon and oxygen) from He burning. The rest of the helium forms a shell surrounding the CO core and the helium shell remains degenerate until He burning is triggered by hydrogen burning in the shell surrounding the helium shell. This degenerate helium burning (Helium shell flashes) can produce convective instabilities and strong stellar winds, resulting in high rates of mass loss. The helium shell flash repeats multiple times, and these successive flashes gradually drive the envelope layer away. The inner carbon oxygen core is eventually exposed and becomes inactive, and a CO white dwarf is formed. A star like our sun needs $> 10^9$ years to become a white dwarf, thus a time scale of 1-2 $\times$ 10^9 years [5] is the time signature of the progenitors of the earliest Type Ia Supernovae, which involve at least one white dwarf and will be discussed later in this chapter. This evolutionary stage is also important as it is the site of the s process that synthesizes about half of the elements heavier than iron.

By contrast, stars with masses between 4 $M_\odot$ and 8 $M_\odot$ have an initial evolutionary track that resembles that of their lighter siblings; however, for these stars, the central temperature is high enough to burn carbon into neon and magnesium, but insufficient to fuse neon. Thus the remnant core will be composed of oxygen, neon and magnesium, producing a O-Ne-Mg white dwarf.

Stars heavier than 8 $M_\odot$ go through the sequences of core burning described above and then continue onto Ne, O and Si burning ending with an iron core. Beginning with carbon burning, the burning processes become so rapid that there is not enough time for the stage of repeating helium shell flashes. Once the iron core reaches the Chandrasekhar limit of 1.4 $M_\odot$, gravity overpowers electron degeneracy pressure, forcing electrons to combine with photo-disintegrated protons into neutrons. In the end, the core collapses, producing a core collapse supernovae, resulting in a neutron star or a black hole compact remnant. Typically, the time duration from the formation of a heavy star to this endpoint is $< 10^8$ years [5].

1.1.3 Nucleosynthesis in Stellar Evolution

Nuclear reactions are not only energy sources, but also important factories of heavy element production. Reactions of astrophysical interest, are categorized into different processes according to the specific astrophysical scenarios in which they occur and four major nuclear processes are described in this section.

The s process (slow neutron capture process) is a chain of reactions that involve neutron absorption and the beta decay of the radioactive nuclear isotopes produced. This process is characterized by neutron densities being high enough to produce neutron absorption products with significant abundances, but also low enough to give the radioactive products time to decay back to stability on time scales of ∼year. The s-process is important in producing nuclear abundances of elements heavier than iron. Potential s process sites include helium burning stages in stars with masses above 0.6 $M_{\odot}$. The majority of s-process products are produced by stars with masses between 1 and 2 $M_{\odot}$, and this leads to a signature time scale of 1-2 Gyr [5].

By contrast, the r (rapid neutron capture) process [2] involves much higher neutron densities so that, during the r process, a radioactive isotope will have high probability of absorbing another neutron before it decays. As a result, this process pushes the production of neutron-rich isotopes far from stability. As this process requires very high nuclear densities, potential locations include core collapse supernovae, where large amounts of neutrons are produced through electron capture, and neutron star mergers, where neutrons are already abundant.

Both the s and r processes create heavy elements above the iron peak, but the resulting relative isotope abundances are different between the two processes, especially at elements such as Xe, Te, Ba, Eu and Au (Fig. 1.4). The ashes of these processes are then incorporated into new stars and the ratios of isotopic abundances in stars are indications of different nuclear processes.

The p-process is a process responsible for producing proton-rich elements. Though details of this process are not understood, it is believed that this process starts with reaction seeds of heavy elements from the s and r processes. The majority of p-nulei are thought to be produced through neutron knock-out reactions (γ,n), followed by (γ,α) or (γ,p) reactions and subsequent β decays [6]. This process requires high environmental temperatures, so that photons have enough energy to knock out nuleons, and very short time scales so that most p-process products can survive. Researchers (e.g. [7]) point out that p-process elements come from different astrophysical sites: i. e. high temperature environments produce lower mass p-nuclei and low temperature environments produce high mass p-nuclei.

The rp-process (rapid proton capture process) is another process producing proton-rich nuclei. Different from the p-process production chain, elements are mainly produced through consecutive (p,γ) reactions and β^+ decays. Likely rp-process sites include classical novae and X-ray bursts (XRBs), where both temperatures and proton densities are high. Besides (p,γ) reactions and β^+ decays, the final nuclear abundances and energy output in the rp-process can be largely affected by (p,α) and (α,p) reaction rates. These (p,α) reactions close reaction cycles in the rp process, such as the NeNa cycle, while (α,p) reactions can compete with (p,γ)

reactions (e.g. ^{18}Ne(α,p), a break out reaction from the CNO cycle, and ^{30}S(α,p), which is a waiting point in XRBs and can affect the luminosity profile [8]).

Given the importance of (p,α) and (α,p) reactions, an experimental setup has been specially designed for measuring (α,p) reactions at Argonne National Laboratory. The success of the ^{4}He(^{20}Ne,p)^{23}Na reaction measurements presented in this thesis are proof-of-principle tests of this setup, which opens the door for future (α,p) reaction measurements of astrophysical interest.

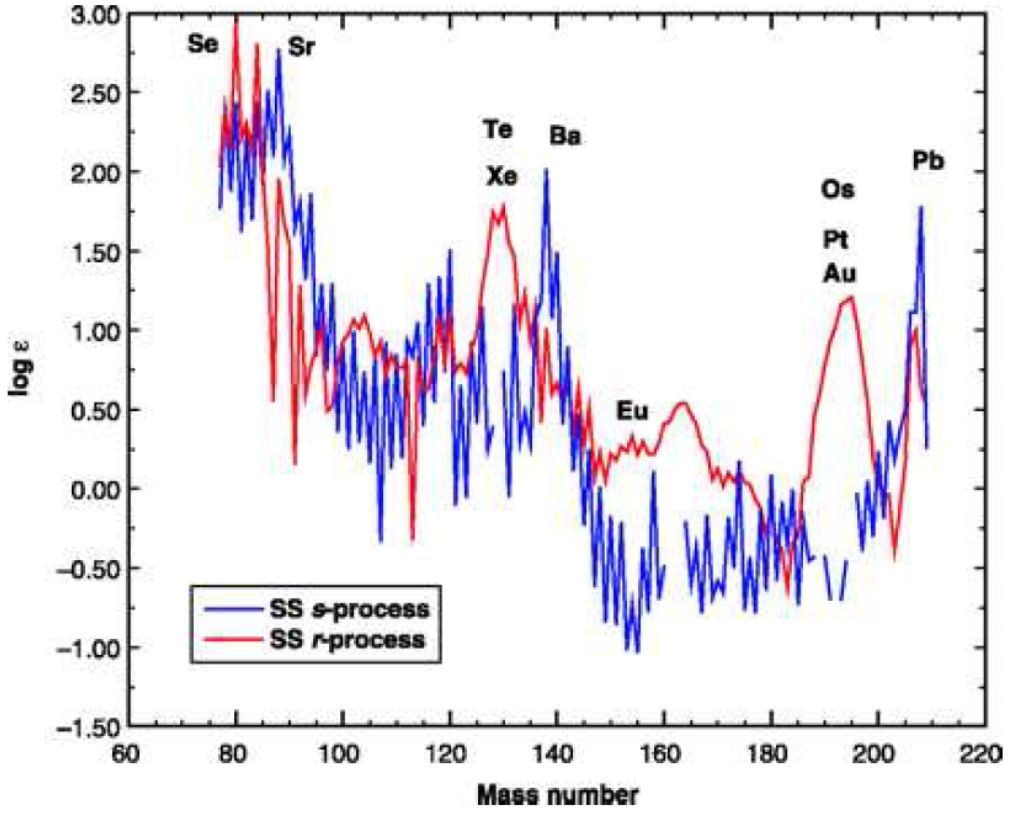

Figure 1.4: Abundance (ε) comparison between s process and r process isotopes in the Solar System (SS) [9].

1.2 Type Ia Supernovae

1.2.1 Overview of Type Ia Supernovae

In general, supernovae (SNe) are classified based on their optical spectra. In this classification, Type Ia Supernovae (SNeIa) do not exhibit any hydrogen lines and present a strong blueshifted Si II line at 615 nm (Fig. 1.5) [10]. Early stages of SNeIa spectra are characterized by lines from high velocity intermediate mass elements

from oxygen to calcium (Fig. 1.6). At later times, the spectra evolve into a stage dominated by P Cygni profiles [11] of iron lines. These spectral profiles illustrate the stages of nucleosynthesis and are used to validate hydrodynamic simulations [12].

SNeIa are believed to be associated with binary systems with at least one white dwarf. The white dwarf accretes mass from its companion until its mass exceeds the Chandrasekhar limit, at which point gravity overpowers the degenerate electron pressure, and this results in a catastrophic explosion. Different from core collapse SNe, during which the core collapses into a compact remnant (a neutron star or black hole), the explosion completely destroys the white dwarf and no compact remnant survives.

It is unanimously agreed that the accretor is a C-O WD in SNeIa, because of the following reasons: 1. the explosion of a He WD will inevitably eject He, which contradicts observations; 2. O-Ne WDs are not populous enough to produce the bulk of SNeIa. 3. Simulations involving O-Ne WD are more likely to produce a collapse [13].

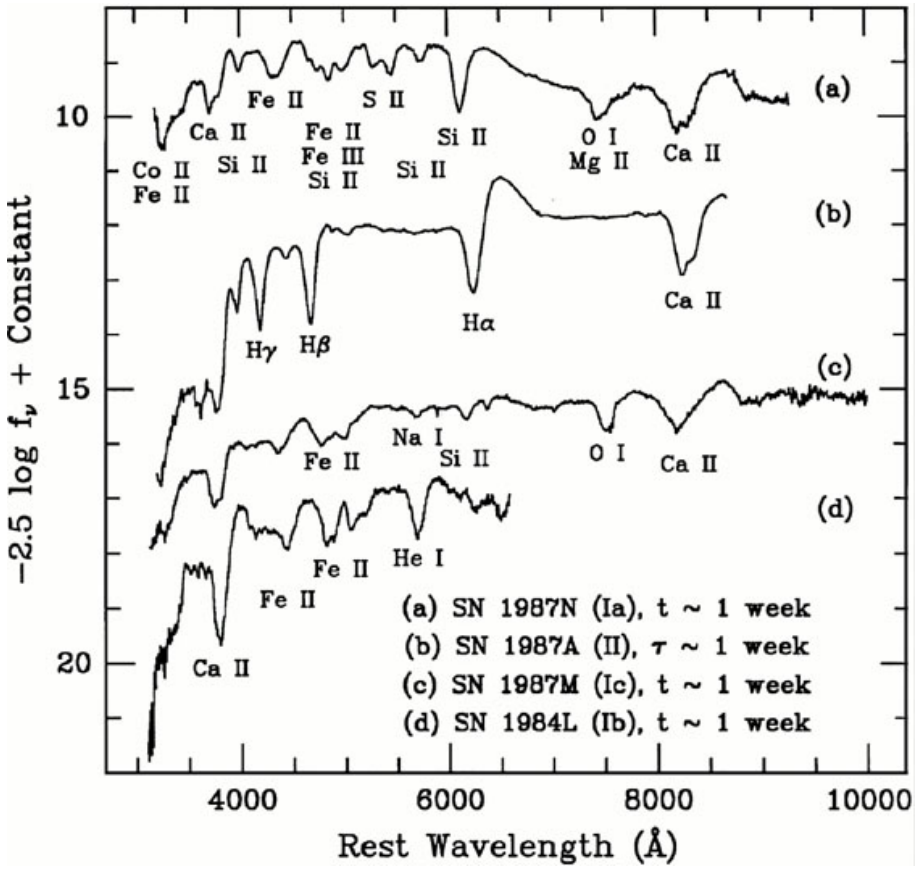

Figure 1.5: Spectra of different types of SNe. (Figure from[10])

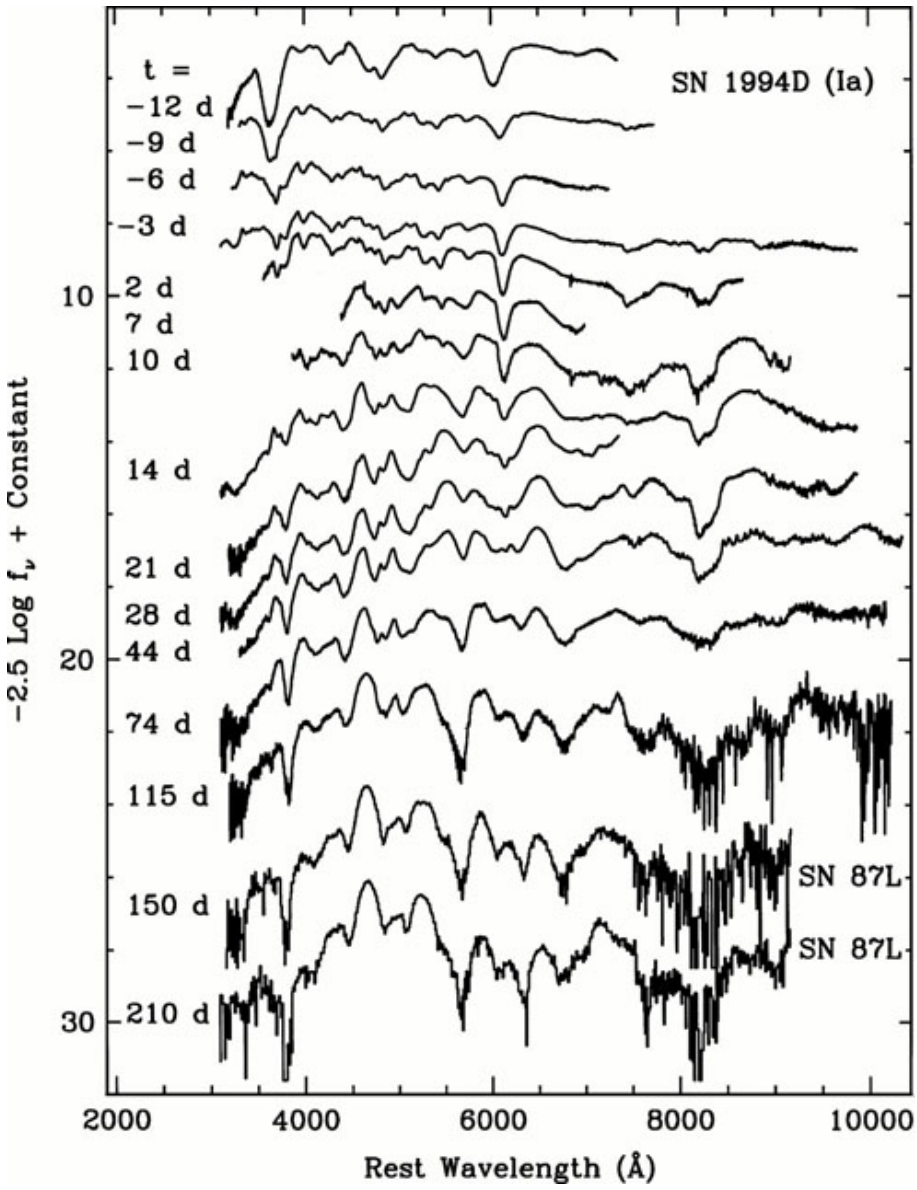

Figure 1.6: Spectra of SN Ia 1994D in NGC 4526 taken at different times relative to maximum brightness, and the last two spectra (labeled SN 87L) are of a similar SN Ia, 1987L. Figure is from [14].

1.2.2 Astrophysical Interest of SNeIa

Nuclear abundances produced in SNeIa are significantly different from AGB (Asymptotic Giant Branch, a late stage of hydrogen burning) stars and Type II SNe. AGB stars account for the production of elements with intermediate masses and s process products, and both Type II SNe and SNeIa are important contributors of iron peak interstellar elements [15]. Specifically, Type II SNe produce a large amount of intermediate mass elements from oxygen to calcium, whose abundances relative to iron surpass the solar system values by factors of 2-3. By contrast, the relative abundances of these intermediate mass elements are much less in Type Ia SNe. Detailed Galactic evolution models also show that SNeIa account for the production of more than half of the iron content [16] in the whole Galaxy and are the source for 65-70% of the iron content in the solar neighborhood [17]. A combination of models for these different SNe are used to interpret the decrease of α-element abundances at [Fe/H]$\gtrsim$-1, observed in multiple massive stars (Fig. 1.7 and Fig. 1.8): The elemental abundances were dominated by Type II SNe nucleosythesis process, which produces large amounts of α-elements, and the α-elemental abundances decrease after the introduction of SNeIa with [Fe/H]$\gtrsim$-1 [5].

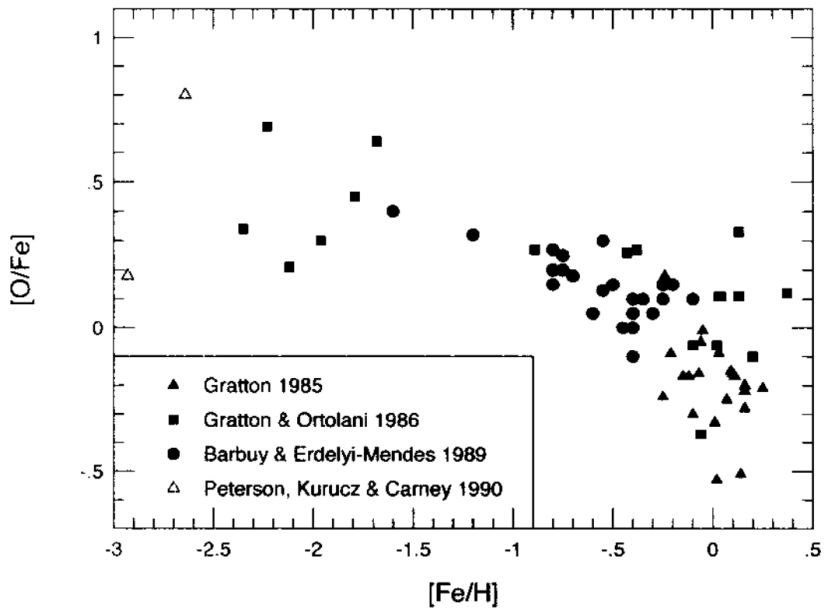

Figure 1.7: Observational data trend of oxygen to iron ratio vs iron abundance in massive stars [5].

Because of their extreme luminosities, SNe have been studied extensively as potential standard candles. Among all types of SNe, SNeIa have very high and consistent peak luminosities in the B band (Fig. 1.9), and are good candidates for standard candles. Though the raw peak luminosities in the B band, after reddening corrections, have a dispersion of $\sim$2 mag, the shape of the light curves can be corrected for different magnitudes as light curves with higher peaks decline more

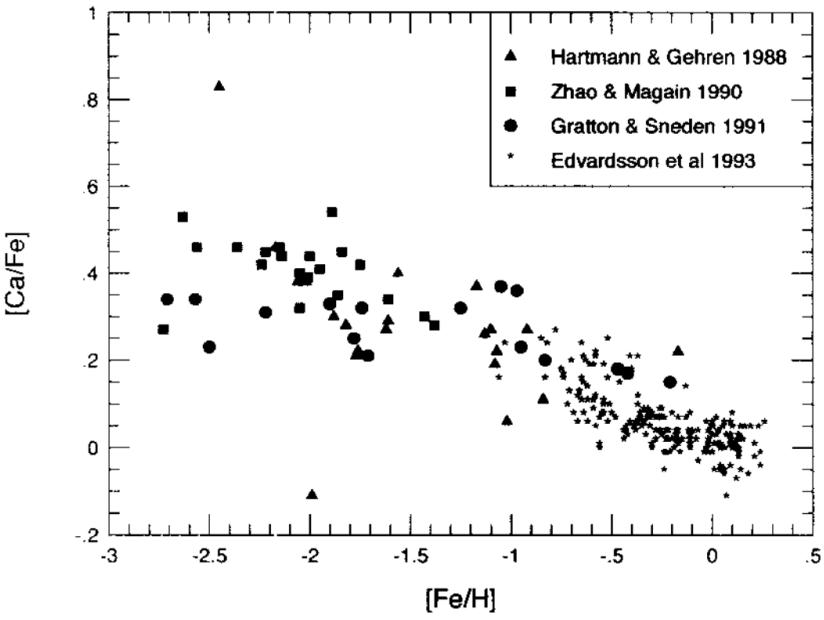

Figure 1.8: Observational data trend of calcium to iron ratio vs iron abundance in massive stars [5].

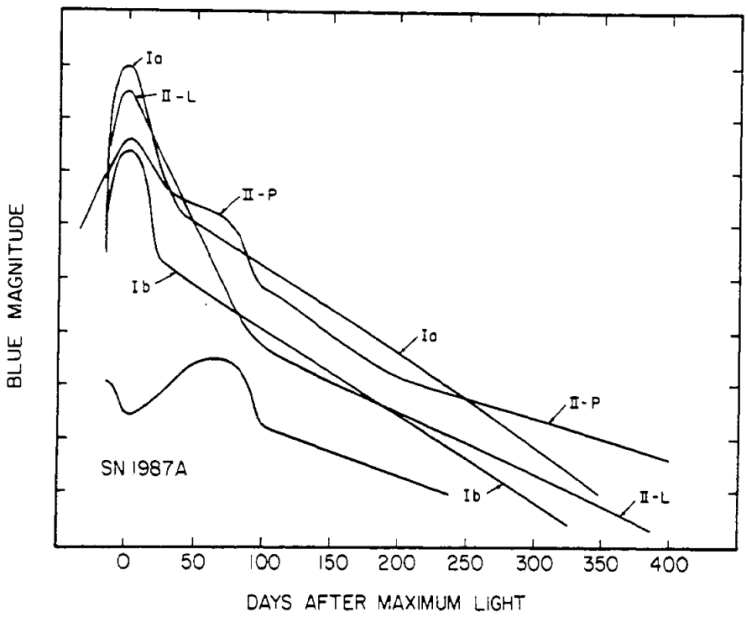

Figure 2. Schematic light curves for supernovae of Types Ia, Ib, II-L, II-P and SN 1987A.

Figure 1.9: A comparison of light curves between different types of SNe (Figure from [18]).

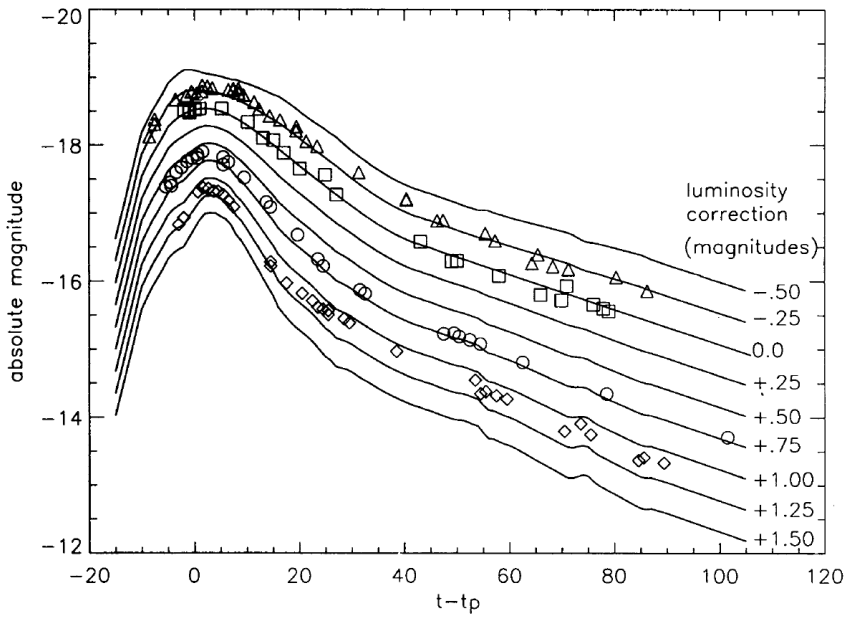

Figure 1.10: Markers represents observations of different SNeIa at different times after peak brightness: 91T (triangle); 81B (square); 86G (circle); 91bg (diamond). Lines are empirical fitting of visual band SNeIa light curves (Figure from [19]).

slowly (Fig. 1.10). The correction factors for the dispersion can be derived using $\Delta m_{15}(B)$, which is the total drop in luminosity from maximum to t=15 days in B band magnitudes [20]. The correction significantly improves the dispersion to 0.17 mag in B and 0.14 mag in V [21], and the adopted value of the corrected peak luminosity at the B and V bands is

$$< M_B > \simeq < M_V > \simeq -19.30(\pm 0.03) + 5\log(H_0/60), \tag{1.6}$$

where H_0 is the Hubble constant.

SNeIa with corrected peak luminosities are useful in cosmological measurements: 1. Nearby SNeIa (z<0.1) are used to measure the Hubble constant [22]; 2. A well observed distant SNeIa with large z is ideal for studying light curve distortion caused by time dilation [23]; 3. The whole SNeIa compilation was used to determine cosmological parameters (Ω_M and Ω_Λ) [24], whose results led to the conclusion that the so-called "vacuum energy density" accelerates the universe's expansion.

1.2.3 Progenitor Models of SNeIa

Despite the significant contributions SNeIa make to cosmology, the fundamental questions about their progenitor and the explosion mechanism are not thoroughly answered. The common progenitor models include the double degenerate model, which involves two WDs, and the single degenerate model, with one dwarf and one main sequence star. Each of the two model classes has its own strengths and

weaknesses.

The single degenerate model has been traditionally favored. In this model, the companion star gradually transfers its mass to the WD until the mass of the WD reaches the Chandrasekhar limit (1.4 $M_\odot$), and a Type Ia SNe occurs. Some research suggests that the elements synthesized via this progenitor scenario better fit Galactic chemical evolution [25] and point out the good agreement of early time spectra and light curves between simulations and observations [26]. Assuming there exists a WD steadily accreting mass from the donor, this model may be the most reliable for preserving the explosion point at $\sim$1.4 $M_\odot$, which could explain the homogeneity of the corrected SNeIa peak luminosities. In addition, recent observations studying the speed and the mass of the ejecta, suggest that all of the SNeIa in the sample burned similar masses [27]. Thus the single degenerate model naively fits the scenario well.

However, there are also clear weaknesses to this model: 1. As the WD explodes, some of the H and He accreted from its companion should be visible at some points, but most studies show no observations of H [28]. Nevertheless, some observations point to the possibility that some core collapse SNe, which have light curves similar to SNeIa, are actually SNeIa. Those studies argue that the H spectra are the result of the interaction between SNeIa ejecta and the circumstellar medium of the donor star [29] and those special cases are named "SNe1.5"; 2. Any surviving post companion should show a very high luminosity after being affected by the explosion, but studies point out that this is not what is observed [30]. However, given the uncertainty of the observations and the limited sample size, the single degenerate model should not be ruled out based on above arguments.

Besides the observational questions, single degenerate models also face theoretical problems. As the WD accretes mass from its companion, if the accretion rate is slow, hydrogen will build up on the surface and may trigger a classical nova at some point. This eruption can drive away more mass than the WD accretes. As a result, a Type Ia SNe will never happen. The situation is improved if the donor is a He rich star, as He burns at higher temperature. However, accumulated He may eventually ignite and will also result in a mass loss. Furthermore, the shock wave brought by a He detonation may ignite carbon inside the WD core and cause a sub-Chandrasekhar mass explosion. The sub-Chandrasekhar mass explosion itself is an independent Type Ia model, and this model agrees better with observations of so-called subluminous SNeIa [26].

Double degenerate models, where two CO WDs merge, are a natural explanation of the lack of H and He in SNeIa spectra. Some simulations show outstanding agreement with observational spectra [12]. As a WD is no longer evolving on the main sequence, the accretion process is driven by gravitational radiation, which gradually brings the two WDs closer. The lower mass WD will eventually be tidally disrupted. The number of double degenerate SNeIa progenitor candidates is enormous and this matches the statistical prediction of the rate of SNeIa: 10^{-3} per year for a $\sim 10^8$ year old Galaxy and 10^{-4} per year for a $\sim 10^{10}$ year old Galaxy [31]. Recent observations also show evidence of a lack of a companion star from one Type Ia site [32]. As companion stars from the single degenerate model are very likely to remain after the explosion, this lack of observation could be a strong statement that at least some

of the observations of the SNeIa are consistent with the double degenerate model.

Nevertheless, the theoretical models for the double degenerate scenario also have some serious questions. As the lighter WD donates its mass to its heavier sibling, the accretion rate is relatively unstable and this may trigger the ignition before the accreting WD reaches the Chandrasekhar limit. Therefore, this model has difficulties in explaining why the maximum luminosities of SNeIa are consistent. Furthermore, simulations show that double degenerate models are more likely to transform the CO WD into a O-Ne-Mg WD [33], which has a high chance undergoing a core collapse, instead of a thermonuclear explosion.

Compared with the single-degenerate model, most of the open questions for the double-degenerate model are on the theoretical mechanism. However, neither the single-degenerate nor the double-degenerate models can be completely confirmed or ruled out. At this time, it is also possible that different models account for different portions of SNeIa. Besides questions about the major classification of the progenitor model, other questions on the details of the explosion exist: e.g. does the burning start at the center or off axis? Furthermore, current simulations require an artificial burning process, where a delayed detonation is introduced. These models can accurately reproduce some of the observations [34], but the real mechanism is not understood. More accurate simulations and more detailed observations are required in order to solve the progenitor problem and answer other open questions.

1.3 Nucleosynthesis SNeIa

1.3.1 Nuclear Processes In SNeIa

The nuclear processes that drive SNeIa include thousands of reactions, and influential reactions are illustrated in Fig. 1.11. The key reaction flows are discussed in this section. The explosion itself is powered by nuclear reactions and typically starts with carbon and oxygen burning [35], e.g.:

$$^{12}\mathrm{C} + ^{12}\mathrm{C} \rightarrow (^{24}\mathrm{Mg})^{*} \rightarrow ^{23}\mathrm{Na} + p + 2.24\ \mathrm{MeV}(32\%) \quad (1.7)$$

$$\rightarrow ^{20}\mathrm{Ne} + \alpha + 4.62\ \mathrm{MeV}(66\%) \quad (1.8)$$

$$\rightarrow ^{23}\mathrm{Mg} + n - 2.6\ \mathrm{MeV}(2\%) \quad (1.9)$$

In the case of Eq. 1.9, the reaction chain ^{23}Mg(n,p)^{23}Na(p,α)^{20}Ne then converts the products into ^{20}Ne. Eventually ^{20}Ne and ^{4}He will combine into ^{24}Mg . There are also fusion reactions of ^{16}O+^{16}O, ^{12}C+^{16}O and ^{12}C+^{12}C. The combination of these and other reactions will loosely produce a chain of nuclei that are multiples of ^{4}He. The ^{4}He chain products are the so-called "α elements". At the top of the chain ^{56}Ni is produced, which is the most bound nucleus created through adding ^{4}He. Any further addition of ^{4}He can be neglected because of the higher Q value and Coulomb barrier.

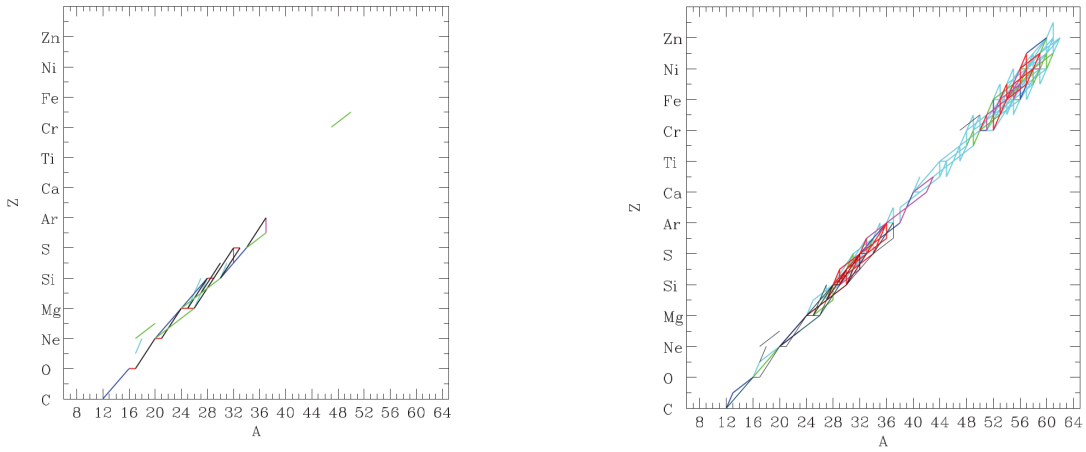

(a) (b)

Figure 1.11: (a) A reaction flow chart of reactions with >10% maximum influence on the final abundances of at least one species. Different types of reactions are marked with different colors: (n, γ) reactions in red, (p,γ) reactions in cyan, (p,n) reactions in magenta, (α,γ) reactions in blue, (α,n) reactions in black (α,p) in green; (b) A reaction flow chart of reactions with large mass flows. Colors represent mass flow levels: red for >0.5 $M_\odot$, magenta for >0.4 $M_\odot$, blue for >0.3$M_\odot$, green for >0.2 $M_\odot$, and cyan for >0.01 $M_\odot$.

This process does not last very long, as the temperature rises quickly and reaches a critical limit ($\sim 4 \times 10^9$ T) at which point newly formed nuclei will quickly be photo-disintegrated. As the elements break apart, they immediately start to form heavier nuclei again. This loop soon reaches an equilibrium, which is called nuclear statistical equilibrium (NSE). Elements inside NSE will forget the previous trajectory of nucleosynthesis, but the initial chemical abundances at the onset of NSE do affect the final chemical abundances. For example, research shows that the percentage of ^{22}Ne residue from the CNO cycle and helium burning through ^{14}N(α,γ)^{18}F(β^+,ν_e)^{18}O(α,γ)^{22}Ne, can affect the electron ratio Y_e and thus is linearly related to the mass ratio of ^{56}Ni [36]; other research also shows how the ratio of ^{22}Ne affects laminar flame speed [37] and other expansion states [38].

The whole WD also separates into different layers during the explosion (Fig. 1.12), where different nuclear processes occur. It is necessary to know the contribution from all of the reactions for a complete understanding of SNeIa.

1.3.2 Nucleosynthesis Studies

There are numerous simulations of SNeIa nucleosynthesis. The typical method of performing such a study is the following. Firstly a hydrodynamic simulation is executed to produce temperature and density trajectories, with a very limited num-

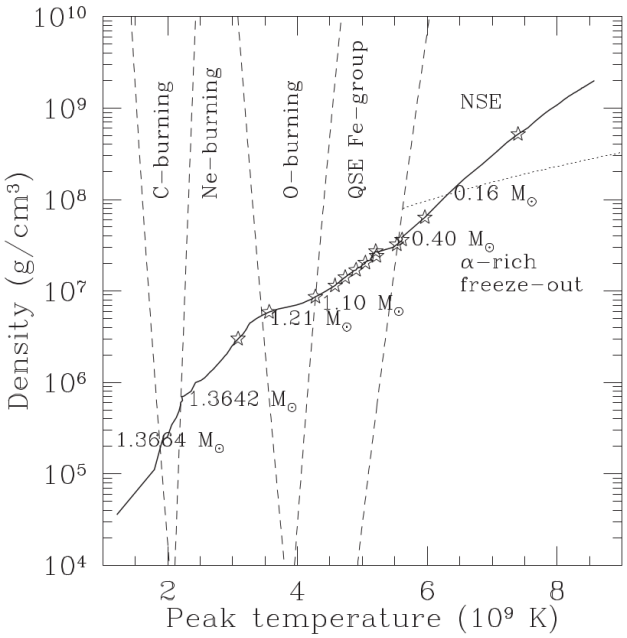

Figure 1.12: Profiles of peak temperatures and densities achieved at each mass shell (solid thick line) during a SNeIa (Figure from [39]). Stars mark different mass layers, separated for each 0.1 $M_\odot$.

ber of reactions (typically the α chain network), which have a significant impact on the nuclear energy released. Then the temperature and density trajectory is used for a postprocessing procedure. The postprocessing procedure includes more nuclear isotopes and a larger reaction network, and it calculates final chemical abundances. The synthetic spectrum can also be obtained with a radiative transport code. Reasonable spectra can be achieved, but large deviations exist at certain points without any fine tuning (Fig. 1.13).

The importance of accurate data in a reaction network is illustrated in one specific example. It was originally believed that simulations overproduced Ti and Cr. However, this conflict is resolved after including revised rates of weak interactions from more accurate measurements and the use of more recent 3D models [40].

However, obtaining experimental reaction data for all reactions in the relevant energy range requires an enormous amount of time and effort. It is therefore necessary to focus on the most important set of reactions for this long term objective. Recently, two research groups independently studied the contributions from each reaction in so-called sensitivity studies [39, 40]. They upscaled and downscaled each standard reaction rate by a factor of 10 individually for each iteration, and collected the reactions that had the largest effects on final elemental abundances. Though the detailed results are different, both studies agreed that ^{20}Ne(α,p)^{23}Na is among the most influential reactions, which also include ^{12}C+^{12}C, ^{12}C(α,γ), ^{20}Ne(α,γ), and ^{30}Si(p,γ). Among all of the reactions listed above, a significant amount of effort has been contributed to the study of ^{12}C+^{12}C (e.g. [41]), ^{12}C(α,γ)[42, 43] and

^{30}Si(p,γ)[44], but very little research has been performed on ^{20}Ne(α,γ)[45] and there have been no direct measurements of ^{20}Ne(α,p) in the astrophysically relevant energy regime, since measurements with gaseous targets are technically more difficult. Parikh et al. [40] specifically point out that the ^{20}Ne(α,p) reaction rate is not well constrained at astrophysical temperatures above 3.5 GK, because of a lack of experimental data. The ^{20}Ne(α,p)^{23}Na rates used in these studies [39, 40] are based on the REACLIB reaction rate library as discussed below.

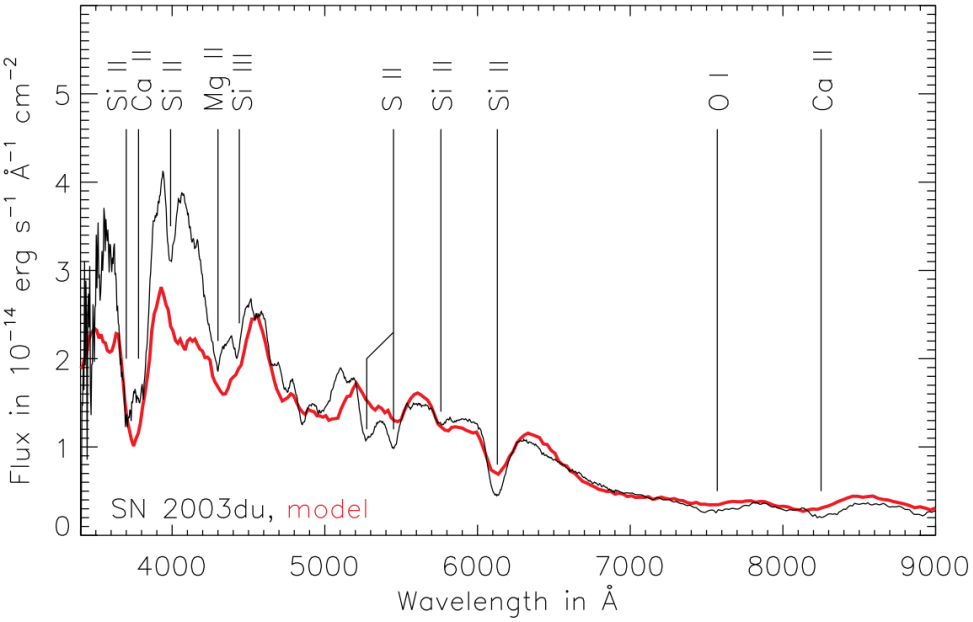

Figure 1.13: Comparison between simulated spectrum (red) and observational spectrum (black) (Figure from [12]).

1.3.3 Overview of Astrophysical Reaction Rates

A general expression for a reaction rate [2], folding the Maxwell-Boltzmann distribution and nuclear reaction cross section is given by:

$$N_A\langle\sigma v\rangle = (\frac{8}{\pi m_{01}})^{1/2}\frac{N_A}{(kT)^{3/2}}\int_0^\infty E\sigma(E)e^{-E/kT}dE \tag{1.10}$$

where E is the kinetic energy, m_{01} is the reduced mass of the two reaction particles, $\sigma(E)$ is the reaction cross section, k is the Boltzmann constant and T is the environment temperature. Assuming no interference between different components, the total reaction rate can be separated into several categories:

$$\langle\sigma v\rangle = \langle\sigma v\rangle_{\substack{\text{narrow}\\\text{resonance}}} + \langle\sigma v\rangle_{\substack{\text{broad}\\\text{resonance}}} + \langle\sigma v\rangle_{\text{nonresonant}} \tag{1.11}$$

The general cross section is given by $\sigma(E) \equiv \frac{1}{E}e^{-2\pi\eta}S(E)$, where $\frac{1}{E}e^{-2\pi\eta}$ ($\eta = \frac{1}{\hbar}\sqrt{\frac{m_{01}}{2E}}Z_0Z_1e^2$) is an approximation of the s-wave transmission probability at energies below the Coulomb barrier and contains all of the nuclear information. $S(E)$ is the S-factor and this value is relatively more constant than $\sigma(E)$ in the absence of resonances. Typically, a Taylor series to the 2nd or 3rd order can well reproduce $S(E)$.

Assuming a constant $S(E)$, the reaction rate of the nonresonant component peaks at

$$\frac{d}{dE}(-\frac{2\pi}{\hbar}Z_0Z_1e^2\sqrt{\frac{m_{01}}{2E}} - \frac{E}{kT})_{E=E_0} = 0 \tag{1.12}$$

, and the resulting peak profile is called the Gamow peak, where E_0 is the centroid of the peak. The Gamow peak represents the energy at which the reaction is most likely to occur at a specific temperature T.

Both the narrow resonant component and broad resonant component of the cross section can be described by the Breit Wigner formula,

$$\sigma_{EW}(E) = \frac{\lambda^2}{4\pi}\frac{(2J+1)(1+\delta_{01})}{(2j_0+1)(2j_1+1)}\frac{\Gamma_a(E)\Gamma_b(E)}{(E_r-E)^2+\Gamma^2/4}, \tag{1.13}$$

where J and E_r are the spin and energy of the resonance, $\Gamma_a(E)$ and $\Gamma_b(E)$ are the partial widths of the entrance and exit channels, and $\lambda = 2\pi\hbar\sqrt{2m_{01}E}$.

For a narrow resonance (Γ is small), substituting Eq. 1.13 for $\sigma(E)$ in Eq. 1.10 results in the reaction rate simplifying to:

$$N_A\langle\sigma v\rangle = N_A(\frac{2\pi}{m_{01}kT})^{3/2}\hbar^2e^{Er/kT}\omega\gamma \tag{1.14}$$

where $\gamma \equiv \Gamma_a\Gamma_b/\Gamma$, which are the widths at the resonance energy and are assumed to be constant since the width of the resonance is small, and $\omega \equiv \frac{(2J+1)(1+\delta_{01})}{(2j_0+1)(2j_1+1)}$. The quantity $\omega\gamma$ is called the resonance strength and Γ is the total width of the resonance.

When the kinetic energy is much higher than the particle threshold of the compound nucleus, the density of states of the compound nucleus becomes dense and a statistical model can be used with good accuracy.

By contrast, reactions at energies near the particle threshold are often characterized by isolated resonances. If the continuous reaction cross section is relatively small, resonance contributions can largely affect the overall reaction rate at lower energies. Thus, it is important to have accurate data, especially at lower energies.

Besides intrinsic properties of the nuclear reaction, the astrophysical reaction rate also needs to be modified by an electron screening factor, as all elements in the astrophysical environment are fully ionized and the space between nuclei is filled with free electrons. The Coulomb force must be corrected with a plasma model for low energy experiments. In the SNeIa energy regime, the Coulomb force is negligible.

Though the theoretical picture is straight forward, experimental measurements are needed to determine a number of factors: the factor for each term in the Taylor

series for fitting the nonresonant component (S factor of the nonresonant component), the resonant energies and strengths for each narrow resonance in Eq. 1.14, and all Γ terms and spins for both broad and narrow resonances in Eq. 1.13. It is worth noting that the nonresonant component is negligible at the energies relevant for this experiment.

Our experiments focus on measuring the cross section directly, instead of the resonance properties. The measurements can be illustrated using the general definition of a differential cross section,

$$\frac{\mathrm{d}\sigma}{\mathrm{d}\Omega} = \frac{\Delta N}{\varepsilon \Delta\Omega I \Delta t n l}, \tag{1.15}$$

where ΔN is the number of counts detected, $\Delta\Omega$ is the angular coverage, ε is the overall detection efficiency, I is the beam rate, n the target particle density, Δt is the duration of measurement and l is the target thickness. The detectors in our measurement cover reaction products over a specific angular range. With a beam intensity and target thickness determined, and the statistics obtained from each detector, the differential cross section at the angles measured in the experiment can be determined.

1.3.4 Current Reaction Networks for SNeIa

In order to supply the reaction networks needed for SNeIa simulations, reaction rates determined by previous measurements are compiled into libraries. A few common reaction libraries are described in this section.

A compilation by Angulo et al., commonly referred to as the NACRE compilation, is one of the most commonly used libraries [46]. The method of rate calculation is similar to what is described in the previous section, but only narrow resonance and non-resonance mechanisms are adopted for cross-section derivations. In this compilation, existing measurements of resonance parameters (E_r and $\omega\gamma$) at the same energy are weighted according to their uncertainties. For non-resonance measurements, S factors are fit with a polynomial series and extrapolated to obtain cross sections at low energy points. Upper and lower limits of cross sections are obtained by error propagation. When large uncertainties are associated with measurements or no measurements exist, a theoretical calculation is implemented. After those three steps, reaction rates can be calculated at temperatures up to a preset cut-off temperature. For temperatures higher than the cutoff temperature, theoretical rates from a Hauser-Feshbach (HF) model are used. However, at the cut-off temperature, the cross section calculated from the HF model may differ from what was extrapolated from points at lower temperatures. This will create a discontinuity in the cross section function. To solve this problem, a temperature dependent factor is applied to the HF results to force the two numbers to match at the cut-off temperature. Similar factors are obtained for the lower and upper reaction rate limits. This work also includes an enhancement factor from the electron screening effect, and cross

section calculations for excited target nuclei.

In Iliadis et al.'s compilation [47–50], the non-resonance cross section is calculated using a single-particle potential model and the reaction rates are estimated through a Monte Carlo approach. Each nuclear physics quantity is associated with a distribution and a set numbers for the nuclear physics quantities of interest are randomly generated and used for each iteration of reaction rate calculations. Eventually, a distribution of reaction rates is obtained. The upper rate, recommended rate and lower rate represent the 0.84, 0.5 and 0.16 quartiles of the accumulated rate distribution, respectively.

The above two compilations, however, cover a very small set of reactions and their use is limited. Recently, a more complete library, REACLIB [51], was developed and this library includes most previous experimental work. This compilation stores the overall reaction rate λ with a 7-parameter function for each reaction

$$\lambda = \exp\left[a_0 + \sum_{i=1}^{5} a_i T_9^{\frac{2i-5}{3}} + a_6 \ln T_9\right] \tag{1.16}$$

, regardless of the physics input. However, most reaction data involving short-lived radioactive elements are still absent. In this situation, a shell model calculation is adopted.

All of the above data compilations are still far from enough. In most cases, the rates at astrophysical energies are either extrapolated or theoretically calculated, and the rates include large uncertainties. Certain reaction rates at higher energies may not be well constrained, due to lack of quality measurements. Thus, it is necessary to provide more reliable experimental data and our measurement of ^{20}Ne(α,p)^{23}Na is one step along this journey.

1.4 Previous studies related to the ^{20}Ne(α,p)^{23}Na Reaction

Although no previous direct measurements have been performed for ^{20}Ne(α,p)^{23}Na at astrophysically relevant energies (one measurement exists at high energy regime [52]), the inverse reaction, ^{23}Na(p,α)^{20}Ne, has been measured multiple times (e.g. [53]) and the data compilation can be found in a number of publications [54, 55], as it is a critical reaction in the NeNa cycle in classical novae and also a useful probe in measuring excited states of ^{24}Mg. These previous measurements focused on measuring astrophysically relevant resonances and fully cover reaction energies from 5.5 keV to 2255.9 keV in the center mass frame (CMS), which almost covers the energy range of interest in SNeIa (Fig. 1.14). This set of measurements is compiled in the work of Iliadis et at. [55]. Measurements at higher reaction energy points are available, but the data are not complete for all resonances [56].

The ^{23}Na(p,α)^{20}Ne reaction is associated with highly excited states of the compound nucleus ^{24}Mg above $\sim$11.7 MeV (the proton threshold, above which ^{24}Mg can decay into p+^{23}Na). At high excitation energies, the density of excited states

is typically high and a statistical model is expected to reproduce the cross section. However, most resonances for the ^{23}Na(p,α)^{20}Ne reaction turn out to be very weak and strong resonances are sparse in the energy range important for SNeIa (Fig. 1.15).

With the differential cross section for the inverse reaction, the cross section for ^{20}Ne(α,p)^{23}Na can be determined via detailed-balanced by

$$\frac{\frac{\mathrm{d}\sigma}{\mathrm{d}\Omega}(a+b\rightarrow c+d)}{\frac{\mathrm{d}\sigma}{\mathrm{d}\Omega}(c+d\rightarrow a+b)} = \frac{|M_{if}|}{|M_{fi}|}\frac{p_f^2}{p_i^2}\frac{(2s_c+1)(2s_d+1)}{(2s_a+1)(2s_b+1)} \tag{1.17}$$

$$\approx \frac{m_3m_4}{m_1m_2}\frac{E_f^2}{E_i^2}\frac{(2s_c+1)(2s_d+1)(1+\delta_{12})}{(2s_a+1)(2s_b+1)(1+\delta_{34})}, \tag{1.18}$$

where s_i is particle spin, p is angular momentum and E is the kinetic energy. All parameters are in the CMS frame.

The conversion parameter from the inverse reaction cross section to ^{20}Ne(α,p)^{23}Na is 1.13. Given the small differential cross section of the inverse reaction (except for cross sections at strong resonances), we shall expect a cross section of $\sim$1 mb for the ^{20}Ne(α,p)^{23}Na reaction.

The results calculated from the inverse reaction only include cross sections for ground state to ground state transitions. Reactions populating excited states in ^{23}Na can also contribute to stellar reaction rates; however, they can not be calculated from the cross section of the inverse reaction. Figure 1.16 shows that our lowest energy measurement (5 MeV CMS and 31 MeV for the ^{20}Ne beam at the reaction point), which is in the range of astrophysical interest in SNeIa, can produce ^{23}Na at excitation energies up to 2.39 MeV.

Thus, given the uncertainties of weak resonances from measurements of ^{23}Na(p,α)^{20}Ne and the absence of ^{20}Ne(α,p)^{23}Na* cross sections, our measurements are needed to provide more accurate and complete cross section information on the ^{20}Ne(α,p)^{23}Na reaction for astrophysical models.

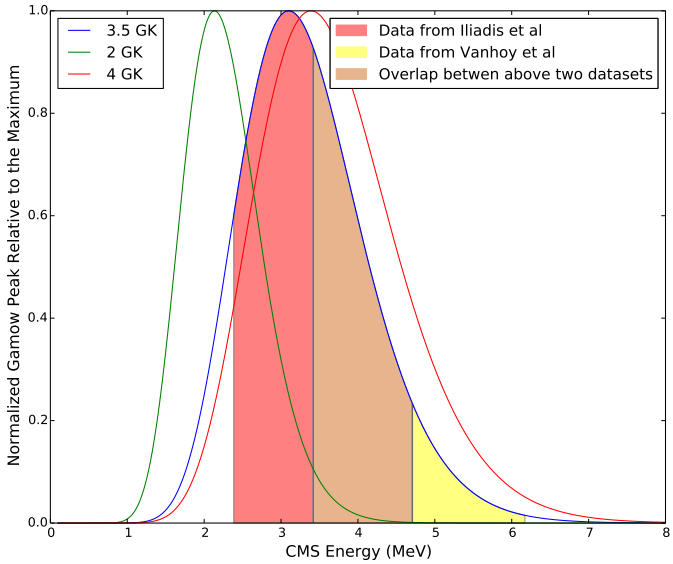

Figure 1.14: Rough estimation of Gamow Peak versus CMS energy for the ^{20}Ne+α reaction. The shaded areas represent the energy ranges that have been measured by various groups [53, 56].

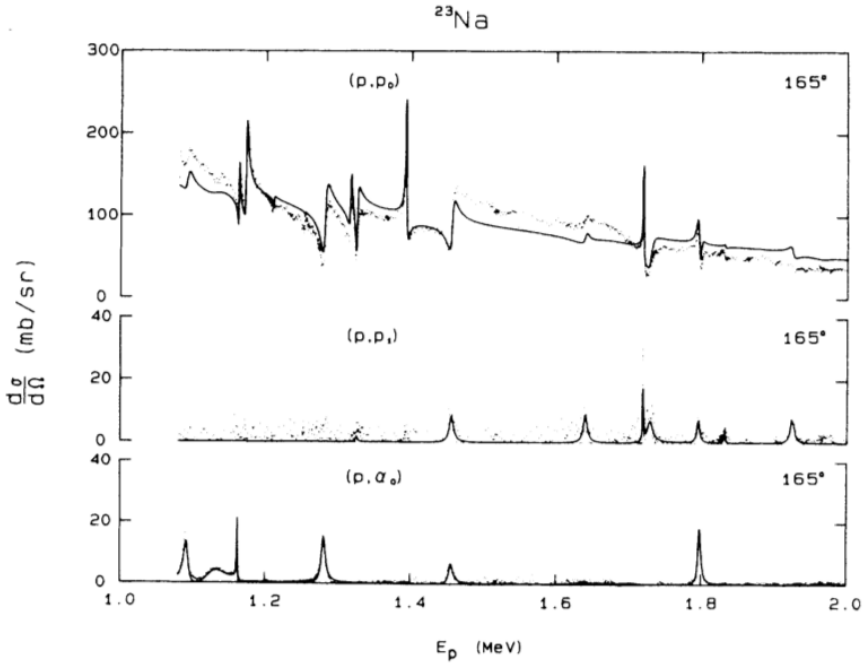

(a)

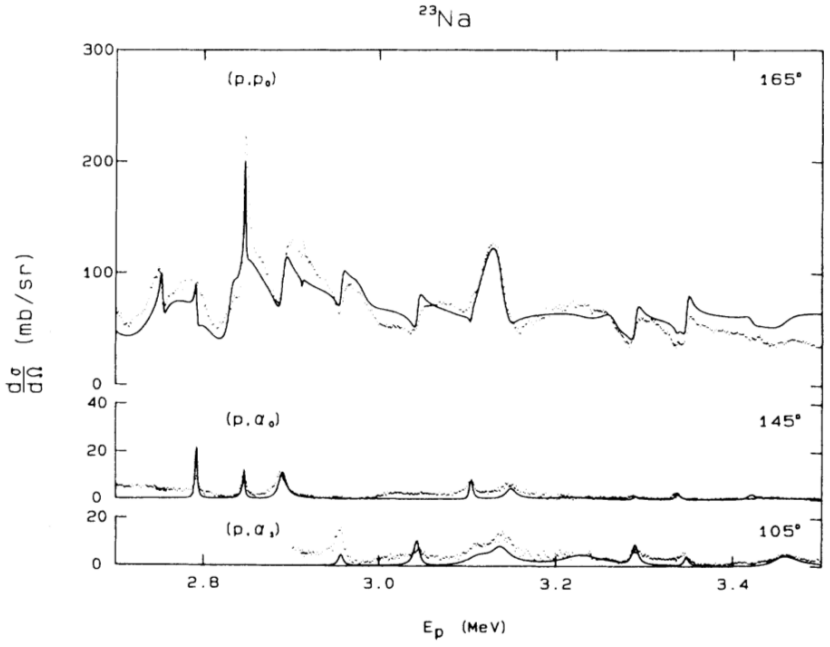

(b)

Figure 1.15: Excitation function for ^{23}Na(p,α)^{20}Ne with proton energies (a) from 1.08-2.7 MeV and (b) from 2.7-3.5 MeV [56].

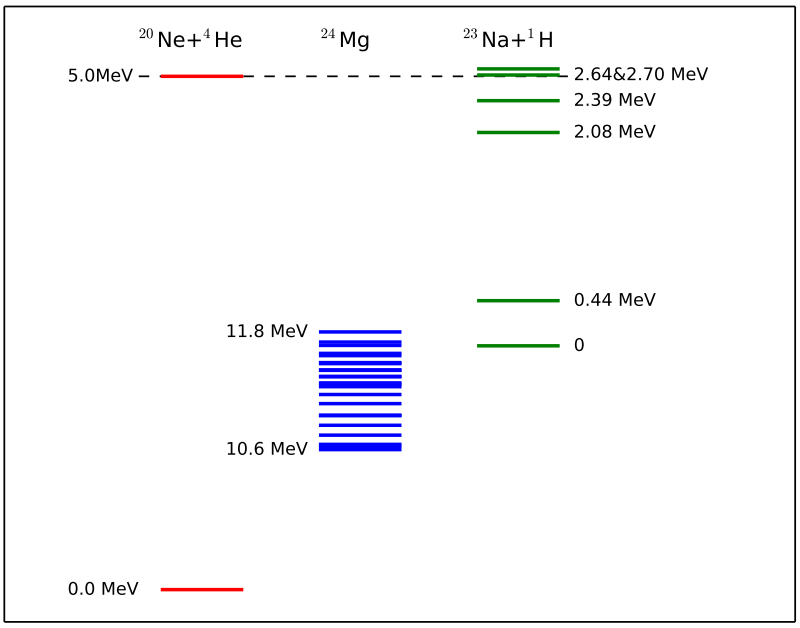

Figure 1.16: Level schematic for ^{20}Ne+α and ^{23}Na+p at different CMS energies, and ^{24}Mg excitation energies.

Chapter 2
Experimental Setup And Devices

We performed the ^{4}He(^{20}Ne,p)^{23}Na experiment at the ATLAS (Argonne Tandem Linac Accelerator System) facility at Argonne National Laboratory (ANL) [57], using the HELIcal Orbit Spectrometer (HELIOS) and a cryogenically cooled gas target. Protons from the reaction were detected in the HELIOS Si array in coincidence with ^{23}Na particles, which were detected by a high-rate ionization chamber. The details of the beam line and its associated detector systems are described below.

2.1 ATLAS

ATLAS is a superconducting linear accelerator located at Argonne National Laboratory that provides beams of projectiles heavier than the electron, and this Department Of Energy (DOE) user facility is open to scientists from institutes worldwide.

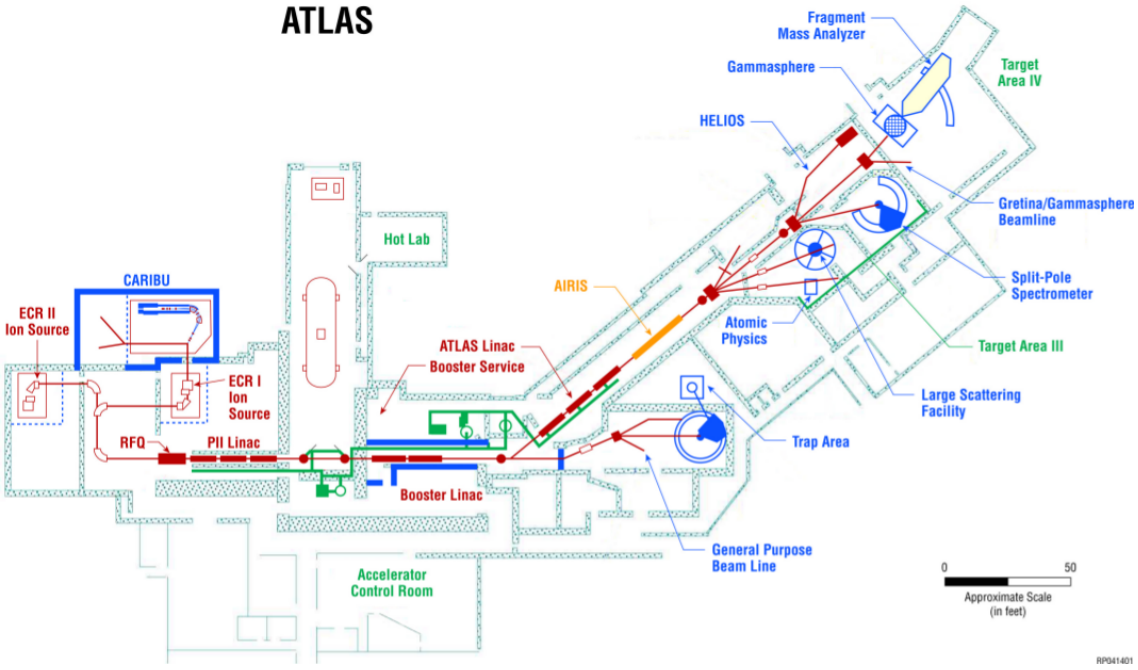

Figure 2.1: A schematic of ATLAS and all available beamlines (beamlines shown in red).

A schematic of the ATLAS floorplan is presented in Fig. 2.1. There are two ion sources:"ECR II Ion Source" and "ECR I Ion Source", which is combined with

CARIBU [58] (CAlifornium Rare Isotope Breeder Upgrade). In an ECR (Electron Cyclotron Resonance) ion source [59], neutral gases are ionized by a rapidly oscillating electromagnetic field. Charged ions are then injected into a series of superconducting RF (Radio Frequency) resonator cavities for acceleration. This technique is applicable for accelerating all stable and long-lived radioactive isotopes in gaseous states. Elements residing in solid materials can also be accelerated after being evaporated, for example by a high-power laser. To provide accelerated beams of short-lived radioactive elements at ATLAS, two methods may be used. 1. Certain neutron rich radioactive beams can be produced using the "ECR I Ion Source" combined with CARIBU if those isotopes are products of ^{252}Cf fission. 2. If requested beam species are close to stability, isotopes can be produced through the in-flight radioactive ion beam production technique [60]. The in-flight radioactive ion beam production technique starts with a heavy stable primary beam bombarding a light target, typically a cryogenically-cooled gas cell. Unstable beam particles are produced via one or two nucleon transfer reactions. The reaction products are further rebunched and the desired products are selected by tuning electric and magnetic field settings of downstream beamline elements.

Ion beams with energies up to 17 MeV/u can be delivered to multiple target areas, including HELIOS [61], the split-pole spectrometer [62], trap area [63] and Gammasphere [64]. The ^{4}He(^{20}Ne,p)^{23}Na reaction was studied in the HELIOS area.

The beam used for this experiment is ^{20}Ne, which exists as a stable gas at standard temperature and pressure. Thus, only ECR ion source II is needed for beam production. The beam purity was $\sim$100 % and the beam intensity requested in this experiment was not limited by the capabilities of the accelerator facility.

2.2 HELIOS

The HELIcal Orbit Spectrometer (HELIOS) is a device specially designed for studying heavy ion reactions in inverse kinematics [65]. The spectrometer itself is a repurposed MRI magnet. Figure 2.2 shows the schematic of the experimental setup for a typical measurement of a (d,p) transfer reaction in HELIOS [66] and Fig. 2.3 is a photograph of HELIOS (side view). The total length of the HELIOS chamber is 234.7 cm, and its inner bore diameter is 92.5 cm. HELIOS is a super-conducting magnetic solenoid, with a 2.86 T maximum central magnetic field strength. The accelerated beam from ATLAS is directed along the magnetic field axis of HELIOS and a target is placed in the middle of the magnetic volume. Light reaction products emitted at backward angles will follow helical trajectories to the central axis due to the magnetic field, and be detected by the Si array arranged upstream of the target (referred as setup 1). The Si array can also be placed at the downstream position relative to the target, in order to detect light particles emitted at forward angles (setup 2).

The absolute deviation of the magnetic field throughout the magnet's volume from the center averaged field is presented in Fig. 2.4 for both axial and radial com-

ponents. The deviations are defined as $B_{Axial}/B_{Average}$ and $B_{Radial}/B_{Average}$, where $B_{Average}$ is the average of measurements of the magnetic field at the central axis where $|z| < 50$ cm. Each data point for the magnetic field away from the central axis is an average of 36 measurements at evenly distributed ϕ angles. In Fig. 2.4, the magnetic field at $\rho < 40$ cm and $|z| < 50$ cm has a high degree of uniformity. Even at $\rho = 45$ cm, the largest deviation with $|z| < 40$ cm is only slightly larger than 2 % from ρ=0 cm, and for the magnetic field along the axis, the deviation is consistently less than 1 % until $|z|$ reaches 55 cm.

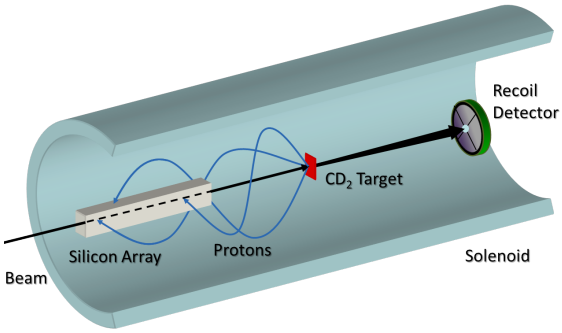

Figure 2.2: HELIOS schematic with a silicon recoil detector in use, adopted from [67]. This plot shows a beam impinging on a CD_2 target. Protons (blue lines) emitted at backward angle are curved back to the silicon array by the strong magnetic field. Because of their larger rigidity, heavy recoils (black lines after the red target) are forward focused and are detected by the silicon recoil detectors.

To study the potential effects on experimental yields brought about by the magnetic field variations, simulated proton trajectories from two reactions studied here [^{2}H(^{20}Ne,p)^{21}Ne and ^{4}He(^{20}Ne,p)^{23}Na] at a few selected energies are plotted on top of a 2D contour plot of the magnet field deviations in both of the radial and axial directions (Fig. 2.5). The simulations of proton trajectories do not include proton energy losses in target materials; therefore, the actual proton trajectories may be slightly smaller than the simulated ones. The figure presents the extremes of proton trajectories (reactions with higher beam energies or lower recoil excitation energies usually yield more dispersive trajectories) and shows that most of the proton trajectories fall into the region of good magnetic field uniformity. Specifically, the largest dispersions in the two experimental setups used for these measurements correspond to the ^{4}He(^{20}Ne,p)^{23}Na study with a 107-MeV ^{20}Ne beam energy (100 MeV at the reaction point) in setup 1 and ^{2}H(^{20}Ne,p)^{21}Ne with a 40-MeV beam energy (31 MeV at reaction point) in setup 2.

The core of HELIOS is a detector system that consists of an array of 24 rectangular silicon detectors. Each group of 6 detectors are glued to one side of an aluminum square frame. The aluminum frame is hollow, so that the beam is allowed to pass through it, and the inner diameter of the hole is 10 mm. The aluminum frame is attached to a support tube, which is mounted to an alignment ring. This design gives the freedom of translating the aluminum frame over a range of 400 mm axially

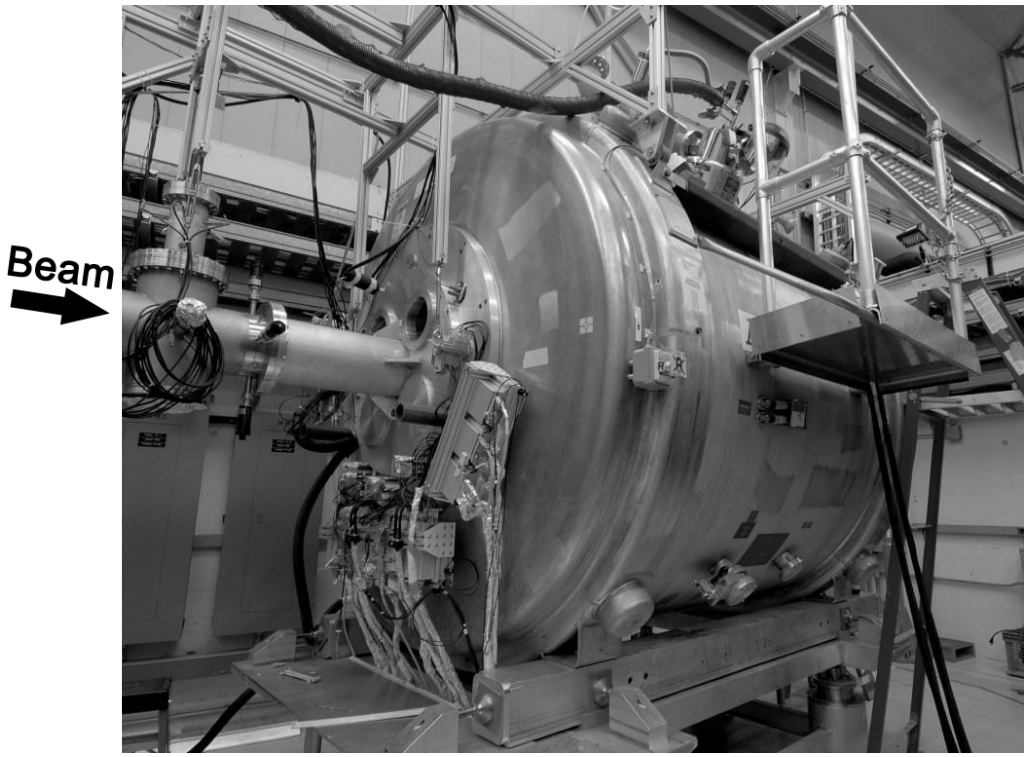

Figure 2.3: A photograph of HELIOS.

along the beam axis. The alignment ring provides precise adjustment of the angle of the aluminum frame such that the axis of the Si array can be aligned with the beam axis. There is an alignment ring at each end of HELIOS, so that the silicon array can be mounted on either side of the target, depending on experimental needs.

Each single silicon detector was produced by Canberra Industries and was originally designed for a previous experiment [68] as a nuclear reaction calorimeter. The size of each silicon detector (Fig. 2.6) is 12 mm $\times$ 56 mm, with a thickness of 700$\pm$15 μm. The active area is 9 mm $\times$ 50.5 mm. The wafers can be fully depleted at $\sim$+105 V reverse bias and can stop protons up $\sim$11 MeV and alpha particles up to $\sim$45 MeV with normal incidence. Two dead layers are introduced from a back ohmic contact and from a front junction contact, which are 500 Å and 1000 Å, respectively, in equivalent silicon thickness. This silicon detector is a resistive type detector. When a particle travels through the detector, it will create electron-hole pairs. Positive and negative charges will be collected by front and back sides of the Si detector, respectively. The amount of charge created during the process is proportional to the energy loss of the particle in the Si. As the front (junction) face of the detector is a resistive layer, the charge collected from the front side is shared by two electrodes and the sharing ratio is inversely proportional to the distance to each electrode. The back side signal is used to extract total particle energies and position information from the front side can be derived, using the following equation,

$$X = \frac{L}{2}[1 + \frac{X_{\text{far}} - X_{\text{near}}}{E_{\text{back}}}], \tag{2.1}$$

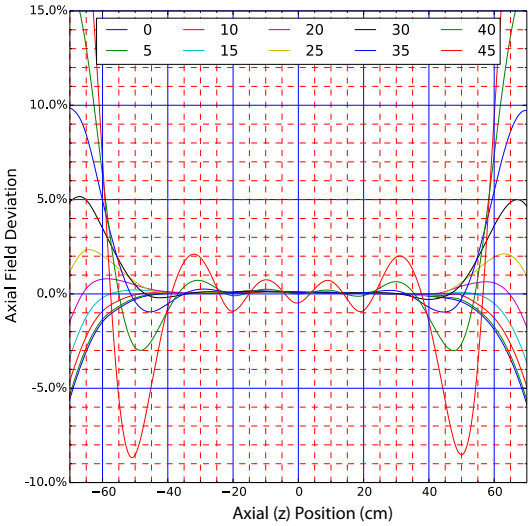

(a)

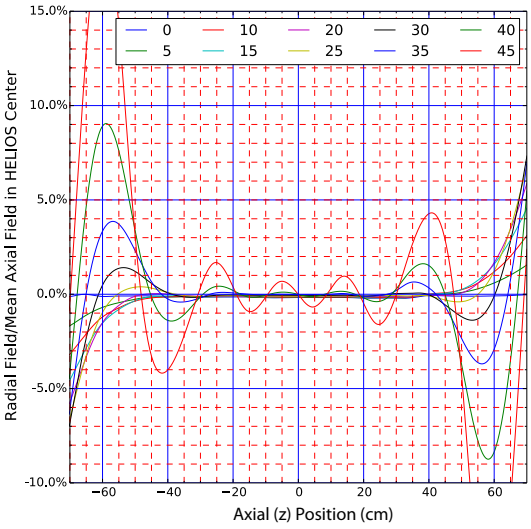

(b)

Figure 2.4: Measurements of (a) $B_{Axial}/B_{Average}$, and (b) $B_{Radial}/B_{Average}$ vs position along the axis. Each magnetic field measurement is an average of 36 measurements at 10° angle intervals in ϕ. The legends marked the radial positions of the measurements in cm.

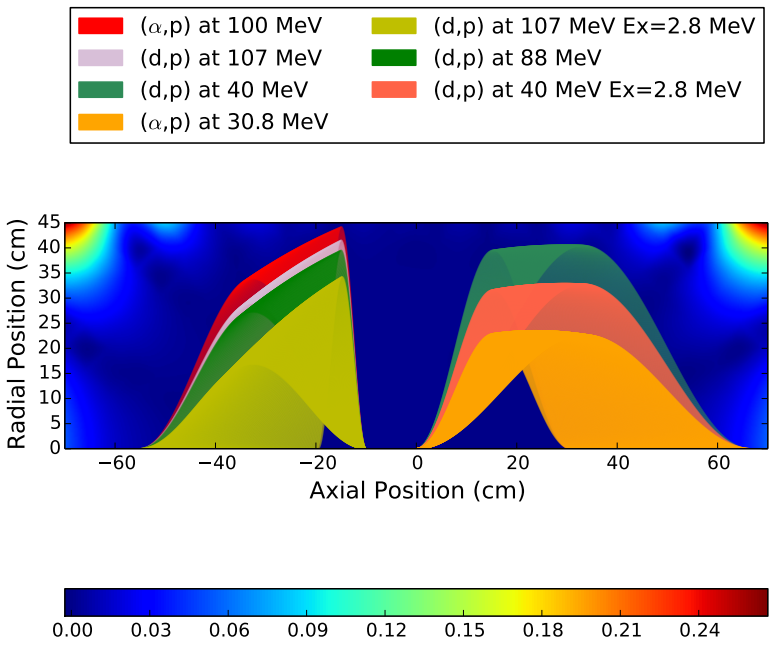

(a)

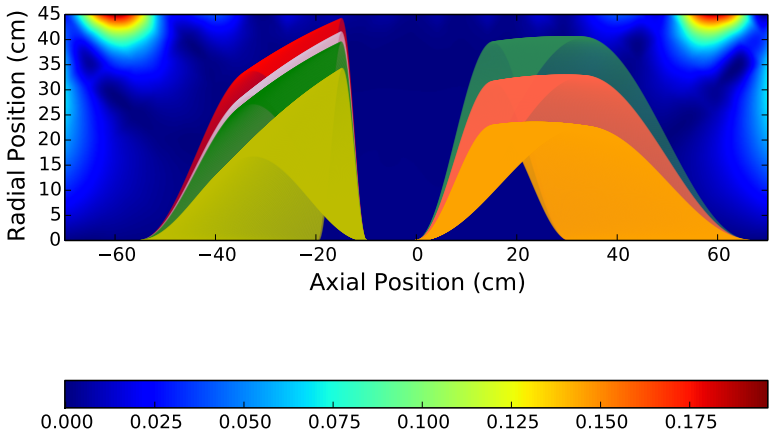

(b)

Figure 2.5: 2D magnetic field deviation distribution of both (a) axial and (b) radial components are plotted in the background. Proton trajectory lines are stacked for selected reactions measured during the experiment. The trajectory simulation does not include any proton energy losses after the reaction point. If an excitation energy is not specified, the trajectories of protons associated with the ground state of the residual nucleus are plotted. The value of the color bar is the ratio between the field deviation and the mean axial field.

where L is the length of one detector's active area, and X_{near}, X_{far} and E_{back} are charge collected for near, far and back side of the detector, respectively. Alternative methods are available, but the above function appears to be the most effective and has been successfully used in previous HELIOS measurements. The calibrated E_{back} signal is used to determine the total proton energy. The position resolution is tested to be between 0.5 mm and 1.2 mm FWHM and the intrinsic energy resolution is ∼50 keV (FWHM) [61].

Figure 2.6: Schematic of one silicon detector, attached to the array mount. Figure is taken from [61].

2.3 Target

The targets are mounted on a fan-like device, which can select the target to be aligned with the beam position by rotating about the beam axis. The target fan is mounted on a rail system, which is connected with a plastic chain and can be controlled by a rotating wheel on the downstream end of HELIOS. This system can translate the target fan along the axial direction. The translation range covers most of the axial length of HELIOS and the translation movement is accurately measured by a laser meter, which has a stated accuracy of ±2.5 mm. In addition to translational freedom, the target fan can also be rotated up to ±18° by a stepper motor. Each step of the stepper motor corresponds to 0.018° of target fan rotation, which is equivalently 0.14 mm arc movement of the targets. The rotation system is controlled by a LabView software program. The program records rotation position and the positions can be repeated by saving the recorded parameters. All components of both the translation and rotation systems are built from non-magnetic materials to operate in the high magnetic field region of HELIOS.

The target fan used in this study consists of two major parts (Fig. 2.7). The main, central piece is the cryogenic gas target, which is a modified version of a previous design [69] used in the split-pole spectrometer area at ATLAS. The cryogenic gas cell is shown in the middle of the gas target assembly shown in Fig. 2.7. The depth of the gas cell can be changed to 1 mm, 2 mm and 3 mm, by installing different flanges. The opening of the gas cell is 0.25″ in diameter for one side and 0.31″ for the other side. The geometry results in maximum angles of emittance of $\theta_{\text{lab}} \leq 72°$ and $\theta_{\text{lab}} \geq 94°$ for the 0.25″ and 0.31″ apertures, respectively, where $\theta = 0°$ is normal to the gas cell flanges, if a reaction happens in the center of the gas cell. Depending on the specific requirements of an experiment, different window materials can be used.

For this cryogenic gas target, Kapton and titanium foils have been tested. Due to the higher atomic number of Ti, experimental spectra obtained using titanium foils show more scattering, but fewer contaminants from fusion evaporation reactions. By contrast, experiments using Kapton foils experience less scattering, but there can be heavy contamination from fusion evaporation reactions in the energy ranges typically involved in HELIOS measurements. Because of the good thermal conductivity and higher melting point, titanium foils usually can tolerate higher beam currents. However, it is important to note that Ti foils can not be used in a hydrogen-rich environment, where Ti and H will form TiH_2 and this component will decompose at temperatures higher than 450°C.

Test experiments using the $^{2}H(^{14}C,p)^{15}C$ reaction, were completed to determine the performance of the gas target. In this experiment the gas target was filled with 500 Torr deuterium gas at room temperature and 1-mg/cm^2 Kapton foils were installed for both the entrance and exit windows (0.25″ for the entrance window and 0.31″ for the exit window). Comparison measurements were taken with a 488-μg/cm^2 solid CD_2 target. The experimental results are presented in Fig. 2.8, which shows the proton spectrum using the solid target with a resolution of ∼220-keV FWHM and the gas target spectrum with 260-keV FWHM resolution. This gas target was also used for a measurement of $^{3}He(^{14}C,d)^{15}N$, to show the feasibility of measuring (^{3}He,d) reactions using this gas target in the future.

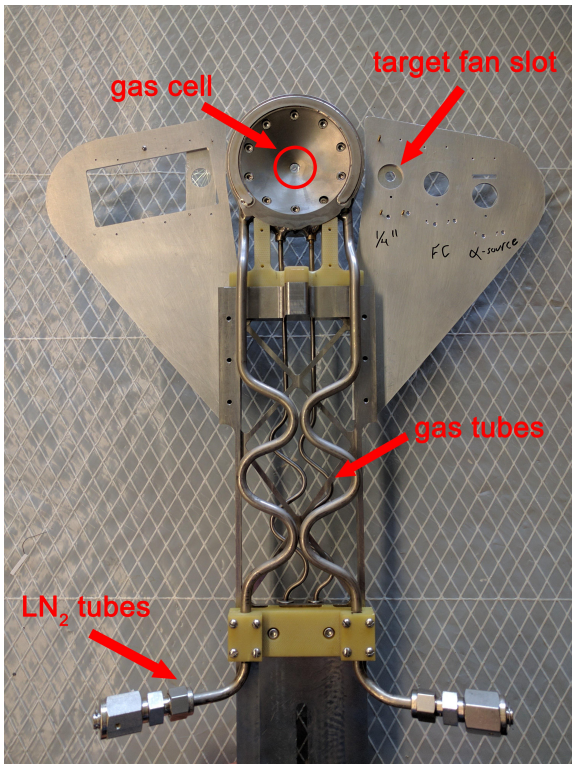

Figure 2.7: A picture of the cryogenic gas target, with two solid target fans installed on either side of the gas cell.

The gas cell in Fig. 2.7 is surrounded by a liquid nitrogen (LN_2) reservoir, which

is contained inside the metal flange. Liquid nitrogen provides cooling for the gas target cell and is circulated through copper lines, shown in the lower half of Fig. 2.7. This cooling system can keep the temperature of the gas cell constantly at ∼93 K. Cooled gas will have ∼3 times higher gas density than gas at room temperature. Specifically, cooled deuterium gas at 500 Torr gas pressure will have density of $3.45\times10^{-4} g/cm^3$ and the 1-mm deep gas cell filled with cooled deuterium gas at 500 Torr has an equivalent deuterium thickness to a 138.0 $\mu g/cm^2$ $(C_2D_4)_n$ solid target.

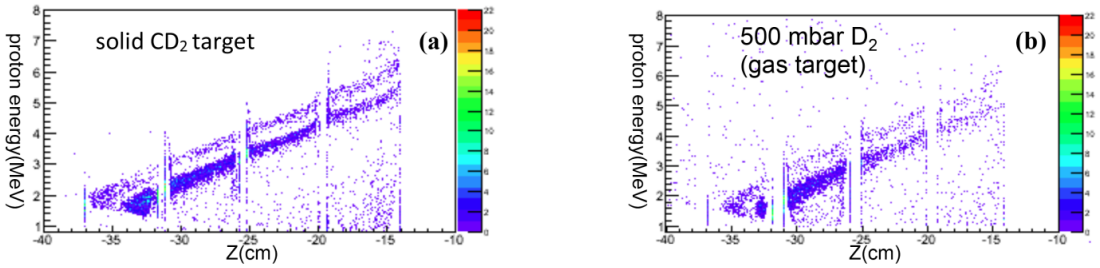

(a) (b)

Figure 2.8: Plots showing the proton spectra from the ^{2}H(^{14}C,p)^{15}C reaction, using (a) a 488-μg/cm^2 solid CD_2 target and (b) the gas target. A 1.0-mg/cm^2 Kapton foil was used for the gas cell windows. The two lines present in the spectra are associated with the ground and the 1st excited state of ^{15}C.

Though the energy spectra from the (d,p) reaction measurements using the gas target typically have worse resolution than measurements with solid targets and solid targets also have a much higher beam current tolerance, implementation of a gas target provides the feasibility of measurements using gaseous materials as targets, such as ^{3}He and ^{4}He, which is necessary for a direct measurement of ^{4}He(^{20}Ne,p)^{23}Na.

Additionally, there are two target fans, located on each side of the gas target assembly. A total of six target slots are available for solid targets. Each slot is 3/4″ in diameter and they are separated by ∼3 cm. On the left side of the target fan, three targets can be installed in the large slot, and there is empty space between each target frame. The empty space was used as a "blank" target during the experiment. For all the experimental runs, three of the slots were used for an alpha source, a Faraday cup and a collimator, respectively (as labeled in Fig. 2.7). The remaining slots contain deuterated polyethylene $(C_2D_4)_n$ targets, gold foils, Ti foil and Kapton foils, depending on the specific experimental setup. Targets used during this series of experiments include two layers of 1.3 mg/cm^2 Ti foils, 132 μg/cm^2 gold foil + 93 μg/cm^2 CD_2 target, 704 μg/cm^2 CD_2 target, 488 μg/cm^2 CD_2 target, 131 μg/cm^2 CD_2 target and two layers of 1 mg/cm^2 Kapton foils. These CD_2 targets were used for calibration purposes and to test the experimental setup using (d,p) reactions, while the Ti and Kapton targets were used to test scattering and fusion evaporation reactions resulting from the gas target windows.

2.4 Ionization Chamber (IC)

2.4.1 LSU IC overview and Design

A large amount of effort was devoted to the development of the fast, position-sensitive ionization chamber (IC), which was located at the downstream end of HELIOS for the detection and identification of heavy recoils and to monitor the ion beam at high counting rates.

The IC design is based on an existing detector described by Kimura et al. [70], where they introduced a new type of ionization chamber composed of multiple tilted parallel planes for electrodes. This IC was implemented for high-energy heavy ion detection at the RIKEN accelerator facility. This design significantly improves count rate ability and is proven to be effective in separating different particle species. As this IC does not use a Frisch grid and the electrodes are approximately perpendicular to the trajectories of incoming particles (i.e. the electric field is almost parallel to the particles' trajectories), it also has benefits such as being free of delay time and position dependence. Later, a similar design was adopted by Chae et al. [71] for low energy nuclear physics measurements with a new fast-counting ionization chamber, which was constructed and commissioned at Oak Ridge National Laboratory. In the modified design, electrode planes were replaced by grids to avoid the additional energy losses that occur when charged particles pass through the electrode planes. We adopted the merits from previous designs, but unlike the previous designs of Kimura et al. and Chae et al. that used a tilted-electrode design, the grids in the LSU design are normal to the beam direction, as shown in Fig. 2.9a. In addition, this new design includes the implementation of position sensitivity, which was not available in previous detectors. Our design was used for the development of a series of fast gas ionization chambers, which have been commissioned at the ATLAS facility at Argonne National Laboratory, the National Superconducting Cyclotron Laboratory (NSCL) at Michigan State University, and the John D. Fox Accelerator Laboratory at Florida State University, where the first IC of this series was built.

The inside of the IC is composed of a stack of parallel grids. The grids are alternatively grounded and positively biased, such that each anode is always sandwiched by two cathodes 2.9a. The grids are equally spaced in 2-cm intervals by plastic spacers, which keep the electrodes electrically isolated. Depending on the specific spatial requirements at each accelerator laboratory, the total number of grids varies from 21 - 27, resulting in an active detector length of 40 - 52 cm. The majority of the grids are circular with an inner diameter of 17.8 cm and an outer diameter of 21.6 cm (Fig. 2.9b). Parallel gold plated tungsten wires of diameter $0.0007''$ are equally spaced over the frame and attached using conductive epoxy. The average spacing is approximately 2 mm between the wires. Unlike the anode planes used by Kimura et al., the wire-grid design allows most low energy particles to travel through the detector without any additional energy loss; however, there is a small probability that incoming particles will be intercepted by the wires and be completely stopped, resulting in a loss of efficiency. For grids with 2-mm spaced wires, this loss of efficiency is $\sim$1% per grid. The anodes are grouped into several sections to provide

multiple energy loss signals.

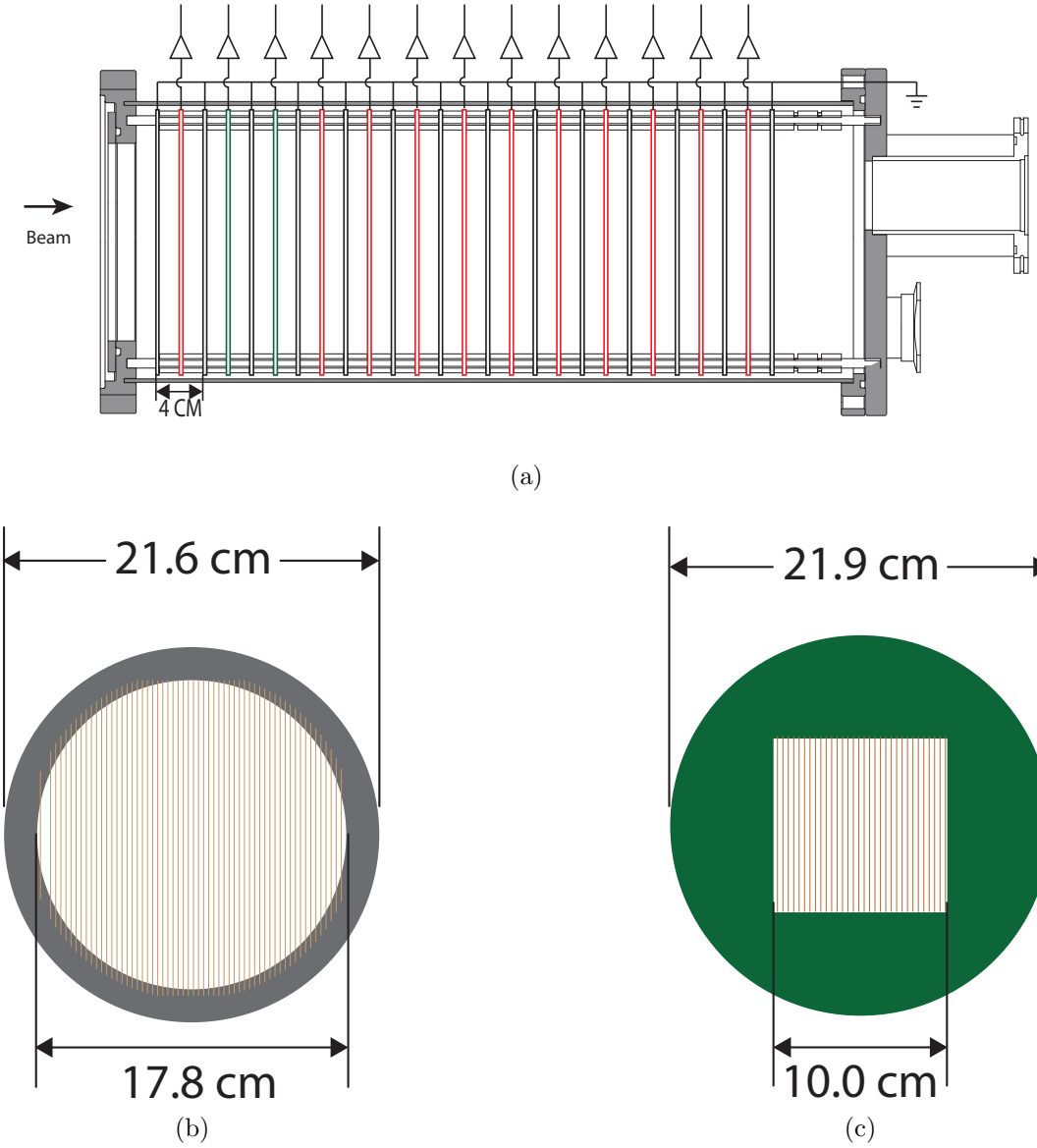

Figure 2.9: (a) The schematic for internal electrode connections in the IC. All of the cathodes are in grey, position sensitive grids are in green and regular anodes are in red. In the lower half of the figure, (b) a CAD drawing of a regular grid and (c) a CAD drawing of a position sensitive grid are shown. Average wire separations for regular grids and position sensitive grids are 2 mm and 3 mm, respectively.

A new capability for position sensitivity has been developed for these ionization chambers. In addition to the grids described above, two position sensitive grids with an inner square opening of 10 cm × 10 cm were fabricated from G-10 plastic circuit boards (Fig. 2.9c). A total of 32 gold-plated tungsten wires are soldered to pick up pads, evenly spaced at 3 mm. Signals from each of the wires are read out individually by a multichannel preamplifier. Two position-sensitive grids are

installed at the second and third anodes positions in the IC at Argonne, and are rotated about the beam axis by 90 degrees relative to each other in order to record both the x and y positions of the incoming particles.

The detector is filled with gas (typically isobutane or CF_4) and multiple flanges with aperture sizes varying from 3.5 to 6.5 inches in diameter for the entrance window were fabricated to accommodate reaction studies with a range of recoil ion angles. Depending on the size of the entrance aperture, the gas pressure of the ionization chamber, and the energy of the incoming particles, the Kapton material used for the IC window had a range of thicknesses from 7.5 μg/cm^2 - 25 μg/cm^2. For example, some typical pressures are 50 Torr for 7.5-μg/cm^2 Kapton when the 5$''$ aperture is used and up to 600 Torr when a 25-μg/cm^2 Kapton window is used with the 3.5$''$ aperture. However, high pressure will cause stretching of the Kapton material, which may lead to additional dead space (of up to 5 cm) before the active volume of the detector, and this distortion can be permanent. The distortion can be alleviated by adding a support grid. Experimental tests have shown that a 1.5-μg/cm^2 thickness mylar window with a support grid can hold 20 Torr of gas pressure for a $\sim$2$''$ aperture.

As discussed above, the grids in the LSU IC are positioned normal to the beam axis, unlike the electrodes in the original design by Kimura et al. One purpose of the original titled electrode design [70] is that the electric field produced is not aligned with beam direction and the field can pull away ion pairs from the beam trajectory, which may result in less columnar re-combination [72]. Though the idea of reducing re-combination is straight forward, neither direct experimental comparisons nor theoretical calculations were presented in [70, 71]. Given that the LSU ICs may also be used in or near strong magnetic fields as in the case here, a simpler non-titled design was adopted.

The magnetic field effect on electron trajectories can be briefly illustrated in a toy model. In the model, 10^5 m/s drift speed is used for electrons drifting towards electrodes, and all other parameters are chosen to be similar to the experimental setups (30° titled grids, 225 V bias voltage, 2 cm separation between electrodes and 0.5 T magnetic field, which is the fringe field of HELIOS in IC region). Electron motion in electric and magnetic fields can be decomposed into two components: normal drifting (in the direction of $\vec{E} \times \vec{B}$) and orbital motion. The orbiting component can be ignored as the electron orbiting radius is $\sim 10^{-8}$ m in a 0.5 T magnetic field (i.e. the fringe field at the position of the IC). The normal drifting component is perpendicular to both the magnetic field direction and electric field direction, and the speed is $\sim$3000 m/s, roughly 3% of the combined drifting speed. Consequently, normal drifting will result in a final radial electron position 2.4 mm away from beam axis with 2 cm separation between each pair of grids, before the electrons are collected by the anodes. This result is not significant when compared to the 1 cm drifting for electrons when the IC is operated in a non-magnetic environment. As the toy model shows no obvious differences between the electron trajectories with titled grids and nontitled grids in magnetic environments, it is expected that the recombination issue is not significantly improved with tilted grids. However, direct experimental comparisons of resolutions between the two designs under the same

environmental conditions are currently not available.

Kimura et al.'s design also may have a negative geometric impact on measurements in lower energy nuclear physics. For our purposes of detecting heavy recoils produced by reactions at low energies, the reaction products will be scattered away from 0 degrees. With tilted grids, this results in slightly different path distances of the ions in the gas for recoils at different ϕ angles and may cause poorer energy resolution (Fig. 2.10).

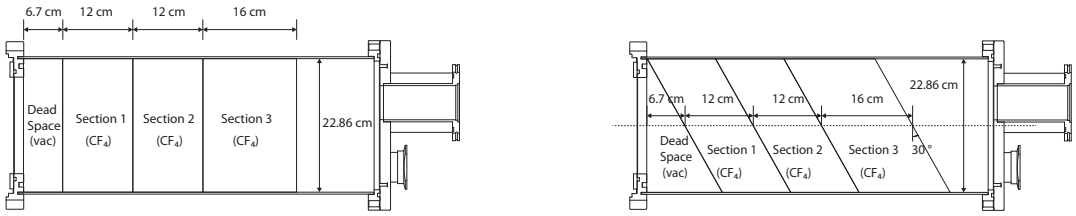

(a) (b)

Figure 2.10: (a) The cross sectional diagram for a non-tilted grid IC. The IC used in the simulation model discussed in the text consists of a 25-μm Kapton foil entrance window, a deadspace layer, which is under vacuum, and three sections of CF_4 gas. (b) The diagram for the tilted grids IC used in the simulation, which consists of the same layers as used in the non-tilted IC simulation. However, the downstream surface of deadspace layer and both surfaces of all three CF_4 sections are tilted by 30°.

A Geant4 simulation was performed, to study the impact from asymmetry in ϕ on the energy resolution of the particle groups. The simulation is constructed to mimic the HELIOS setup and geometry, where the target is placed ∼1 m away from the IC entrance window and data is produced using ^{28}Si(^{12}C,^{12}C)^{28}Si elastic scattering at 6 MeV/A. A uniform 2.85 T magnetic field is imposed on the entire simulation space and recombination effects are not included in the simulation process. Similar geometric designs are used for both ion chambers with tilted and non-tilted grids as shown in Fig. 2.10. Comparisons are studied under both magnetic and non-magnetic environments and the simulation results are presented in Fig. 2.11. In both magnetic and non-magnetic environments, the tilted grids design is observably worse in resolution and the difference is magnified in a magnetic environment, such as the HELIOS beam line. However, without a detailed study including both geometric effects and re-combination between ion pairs, it is not possible to reach a firm conclusion as to which design is superior.

2.4.2 IC performance

The detectors' performance was evaluated in a series of commissioning and science runs at ATLAS and FSU. The data described below were taken with the LSU-

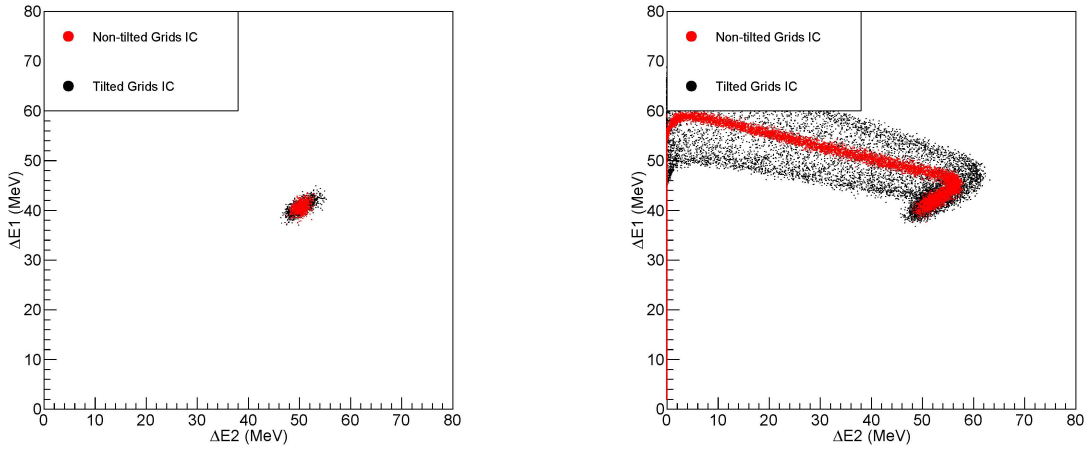

(a) (b)

Figure 2.11: (a) Simulation results comparing data from the non-tilted grid IC (red) with data from the tilted grid IC (black) in a non-magnetic environment. Data points from the titled grid configuration are distributed over a larger area, which indicates worse resolution. Magnetic effects are included in (b), where scattered particles from steeper angles are forced back towards the beam axis by the magnetic field, and the titled grid IC shows a much more disperse spectrum.

built fast ionization chambers in different configurations, which were chosen based on the energy and particle type of the beam. Data presented from IC tests using regular grids are from test experiments performed at the ATLAS HELIOS beam line and data from the position sensitive grids are taken from experiments executed at FSU. As mentioned previously, anodes can be grouped together in different combinations creating ΔE sections of different depths to best suit the experimental needs.

The first commissioning run of the IC built for the HELIOS beam line used a ^{28}Si beam at 6 MeV/A impinging upon a natural C target. Beam particles at 0° were blocked, and the most intense particle group was produced by scattered beam. Figure 2.12 is a typical spectrum of the energy loss in the first IC section (ΔE1) vs the energy loss in the second section (ΔE2) . On the left side of the scattered beam, there are a series of groups with the same ΔE1 value. Those groups are formed when incoming particles are stopped by the tungsten wires on one of the seven grids in the ΔE2 section. Similarly, vertical islands at ΔE2 = 0 are observed when particles stop within the ΔE1 section. The efficiency loss due to particles stopped by the wires is approximately 1 % per grid, as expected.

As the ^{12}C(^{28}Si,^{12}C) experiment was performed at ANL with a pulsed beam, particles detected in the IC can only be separated by multiples of the pulse period (82 ns). Therefore, only certain amplitudes can be formed due to pileup and discrete pileup islands are seen. Pileup is created by two particles detected very closely in time (a few times 82 ns), where shaped signals ($\sim$ 250 ns shaping time) will overlap, resulting in a bigger signal (Fig. 2.13). In the case of a direct current beam, a

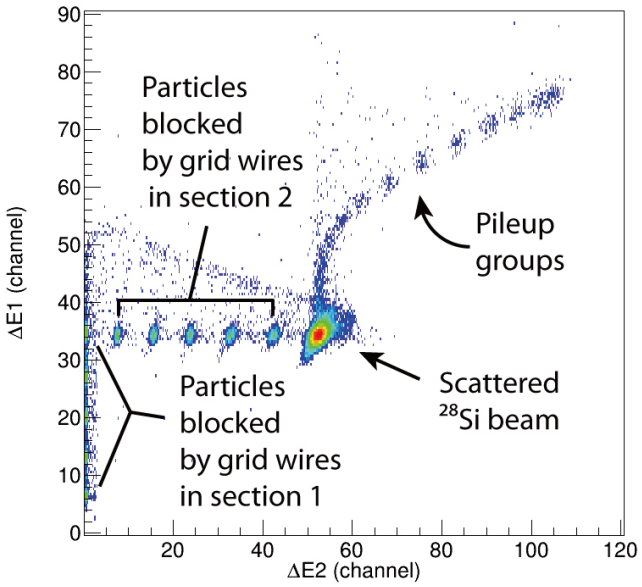

Figure 2.12: A typical IC spectrum, with a counting rate around 8 kHz.

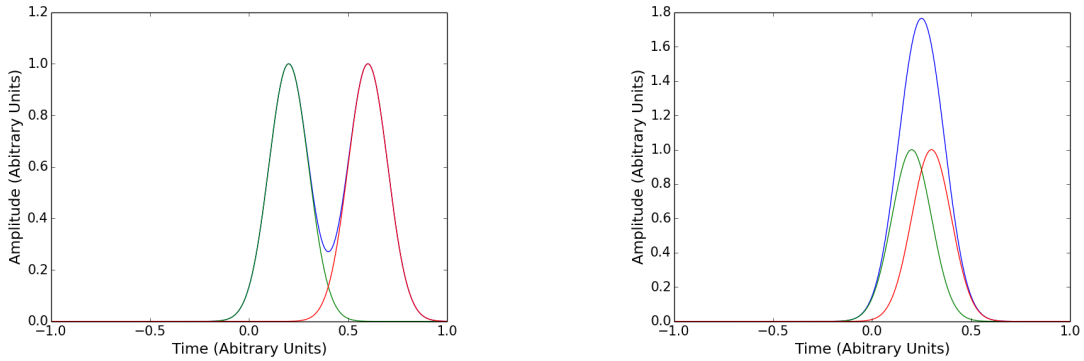

(a) (b)

Figure 2.13: An illustration shows the formation of pileup with two Gaussian peaks, where two consecutive detections (red and green) combine into a single signal (blue). In (a), the peak amplitude of final detection is equal to each of the original signals, and (b) at a smaller separation the two signals merge into a signal peak with a larger amplitude. Units are arbitrary.

continuous pileup band would be observed. The counts in each pileup group can be approximately calculated as

$$N_{pileup} = N_{scatt} * \frac{R_{beam}}{F_{beam}}, \tag{2.2}$$

where N_{scatt} is the integral of the full histogram, R_{beam} is beam rate inside the IC and $F_{beam} = 1/82$ Hz.

To illustrate the formation scheme of pileup, ^{12}C(^{86}Kr,^{12}C) scattering data is also presented. Figure 2.14 shows that pileup formed by large time separations can be eliminated by the pileup rejection function of the shaper module. Using the pileup rejection mode will relocate some pileup islands, which are formed by two signals separated by a relatively large time separation, to the position where the scattered beam group is located (this pileup rejection function can detect pileup from two particles with time separation $\geq 4\times82$ ns, according to Fig. 2.14). Yet, this function can not distinguish pileup between two signals with a very short time separation. Additionally, position sensitive data can be used to suppress pileup events and this method is not restricted to the length of time separation. Details of this technique (using position sensitive data to suppress pileup) will be discussed later in this section.

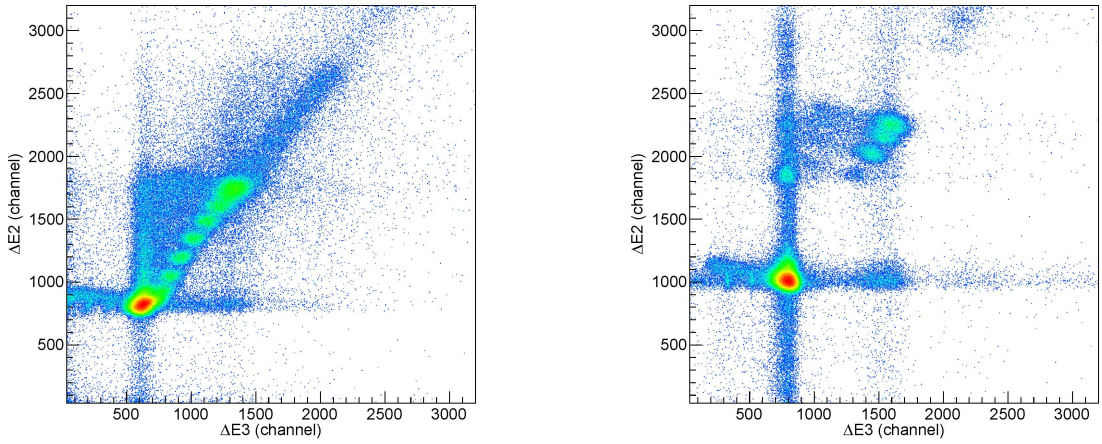

(a) (b)

Figure 2.14: The two IC spectra are obtained with an 860-MeV ^{86}Kr beam impinging on a 357-μg/cm^2 C target. In (a) both signals were collected with the pileup rejection function off, while in (b) the pileup rejection function was on for both ΔE2 and ΔE3 signals.

The energy resolution dependence on high voltage and beam rate can be studied with the ^{12}C(^{28}Si,^{12}C) data set. As mentioned previously, this experiment was performed at the ATLAS HELIOS beamline. As discussed in Section 2.2, HELIOS is a large magnetic solenoid, which has a strong residual magnetic field in the region of the IC that can potentially affect electron drift trajectories. Thus, the resolution

profile was studied both with and without the magnetic field applied. Due to straggling in the target and the window of the IC, energy detection for the last section of the IC typically has the worst resolution. For the purpose of measuring the intrinsic resolution of the detector system, the gas pressure inside the IC was intentionally lowered to enable detection in all three sections; however, only the signals from the first two ΔE sections will be used for the comparisons discussed here.

It is observed that the centroid position of each particle group drifts as the counting rate increases. Possible reasons include that higher signal rates increase the baseline and hence decrease the relative amplitudes of the signals, or that higher beam intensities increase the gas temperature resulting in a decrease in gas density. Calibrations were needed for each run to account for this position shift. The calibration used the average of the energy loss in each section from LISE++ simulation results with beam energies from 5.9 MeV/u to 6.3 MeV/u at 0.1-MeV intervals (Table 2.1). The purpose of calculating energy losses with a range of beam energies is to mimic the uncertainties from deadspace, as opposed to uncertainties of the beam energy itself. The energy range was chosen to minimize the residue of least squares regression between the measured centroids of islands (those which are produced by particles stopping at wires) and the calculated values. Only beam energies with a coefficient of determination from linear regression above 0.95 are included.

Beam Energy (MeV/A)	5.9	6.0	6.1	6.2	6.3
ΔE1(isobutane)	NA	NA	41.65	40.95	40.27
ΔE2(isobutane)	NA	NA	53.67	52.13	50.71
ΔE1(CF_4)	45.19	44.46	43.75	43.08	NA
ΔE2(CF_4)	57.71	56.71	55.42	54.11	NA

Table 2.1: The first column shows the section label and the gas used. The other columns list information of energy loss in MeV for each beam energy setting, which is given in the top row in MeV/A.

After calibration, peaks in the 1D spectra for ΔE1 and ΔE2 were fit using a skewed normal distribution and the full width half maximum was calculated from the fit. The associated FWHM uncertainty (90% Confidence Interval) is obtained using the Bootstrap method [73]. Figure 2.15 shows the resolutions for the ΔE1 and ΔE2 sections as a percentage with respect to the energy loss in each section. The detector was filled with 65 Torr isobutane gas and was biased at +225 V. The resolution deteriorates as counting rate increases. For counting rates above 150 kHz, pileup effects become significant ($\geq$12%) and start to severely distort the shape of the particle group. While the pileup rejection function can eliminate this effect, not enough data points were collected with the pileup rejection mode enabled.

It is worth noting that, though we use 1D spectrum fitting to present correlations between resolution and other parameters, the spectra are highly skewed by elastic scattering curves, particles stopping at wires and pileup effects. It is clear from the experimental work presented here that the ion chamber's ability to separate different particle groups is better realized when data are presented as 2 dimensional plots,

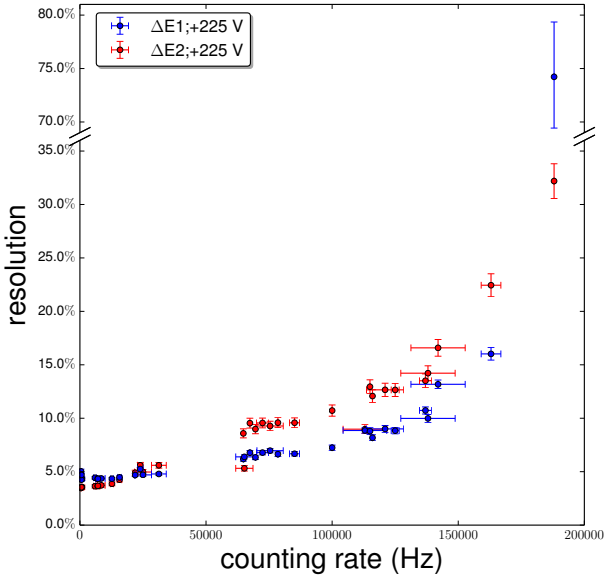

Figure 2.15: Resolution vs. counting rate, when the IC is biased with +225 V.

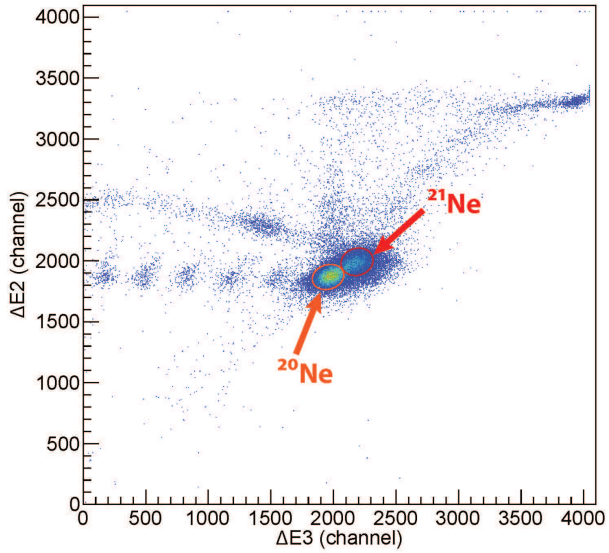

Figure 2.16: Particle ID spectrum for the ^{20}Ne(d,p) measurement. A beam blocker is installed to block the direct beam and counting rates averaged around 200 kHz. A rough timing cut between the IC and silicon array for protons is applied to enforce coincidence.

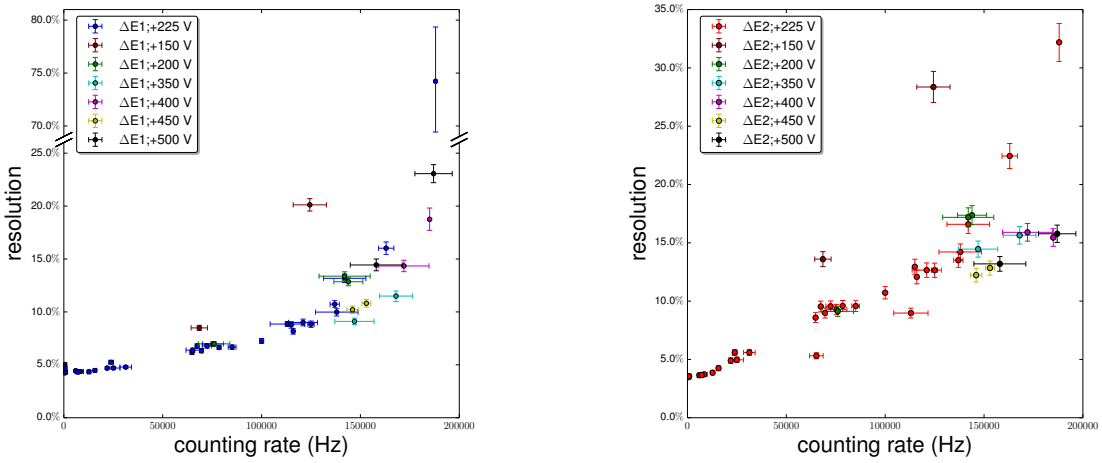

(a) (b)

Figure 2.17: Data from Fig. 2.15 are taken as a reference for comparing IC settings with different high voltage biases. Plots are for the (a) ΔE1 and (b) ΔE2 sections.

such as ΔE1 vs ΔE2. For example, the ion chamber was used for the ^{4}He(^{20}Ne,p) and d(^{20}Ne,p) experiments presented below at counting rates around 400 kHz, and the resolution was still good enough to separate the ^{20}Ne, ^{21}Ne and ^{23}Na particle groups (see e.g. Fig. 2.16).

The operating voltage should scale roughly with gas pressure and the effect of different biases with the IC filled with 65 Torr isobutane gas is shown in Fig. 2.17, where data points taken with IC biases from +150 V to +500 V are plotted with the detailed +225 V biased data in Fig. 2.15. Figure 2.17 shows that, with 65 Torr of isobutane gas, lower bias is associated with worse resolution, especially at high counting rates. For example, the resolution of data with a bias of +150 V is worse than at +200 V. However, the differences are less significant at higher voltage.

A Geant4 simulation was performed with the same configuration as the experimental setup to study effects from the the magnetic field of HELIOS. Simulation results are presented in Fig. 2.18. No differences in energy loss were observed with and without the magnetic field applied. Thus, the same simulated energy losses are adopted for calibration purposes for data sets with and without a magnetic field applied. It is important to note that the simulation only includes yields of the ^{21}Ne reaction products from the ^{2}H(^{20}Ne,p)^{21}Ne reaction with an 88-MeV ^{20}Ne beam in a 2 T magnetic field. Extra factors like divergence of beam spot, scattering off target frame, etc., are not included.

Figure 2.19 shows a detailed experimental study of magnetic field effects. The study was conducted during the same set of measurements of ^{28}Si scattering by a C target. During the study, the ion chamber was filled with 65 Torr of CF_4 gas and biased at +500 V. Measurements under a magnetic field of 2.85 T consistently produced better resolution than those without any magnetic field. The difference increases with higher counting rates. Possible reasons for this improved resolution

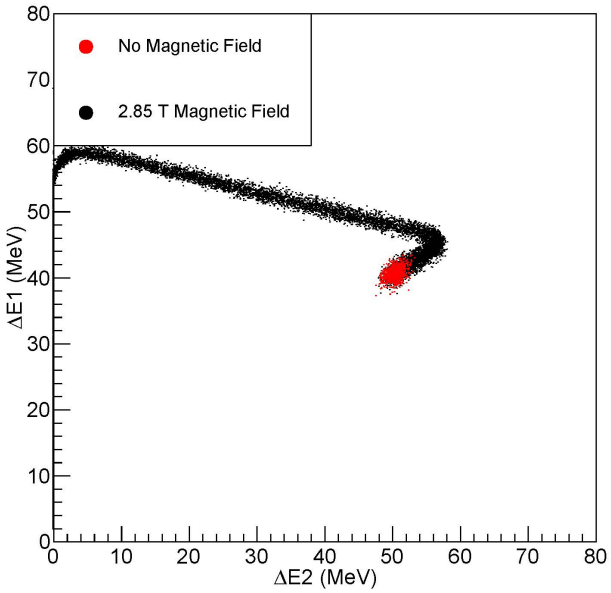

Figure 2.18: A Geant4 simulation comparing reactions yields with and without a magnetic field. An 88-MeV ^{20}Ne beam is used and only ^{21}Ne products from the ^{20}Ne(d,p) reaction are included in the simulation. In the simulation, a beam blocker is positioned between the target and IC.

with the magnetic field applied include that the beam is more focused due to the focusing effects of the magnetic field as shown in Fig. 2.20, which results in less scattering at large angles, and that the ionized electron-ion pairs are drifting in a highly guided trajectory towards the electrodes.

Though no systematic Z resolution test was performed, the ability of IC detectors to separate particle groups of different atomic numbers is well known [71]. As an example of particle identification, a spectrum from a ^{30}S beam production experiment is presented in Fig. 2.21. The IC was filled with 150 Torr of CF_4 gas and biased at +300 V. The ^{30}S beam was produced via the ^{28}Si(^{3}He,n)^{30}S reaction by bombarding ^{3}He gas with a 325-MeV ^{28}Si beam. The spectrum shows that ^{30}S is well separated from other components at a 4.5 kHz counting rate.

2.4.3 Position Sensitive Grids

One improvement in the LSU-built ionization chambers compared to previous designs by Chae et al. [71] and Kimura et al. [70] is the addition of position-sensitive grids, which have been used at the ANL, FSU and MSU accelerator facilities. The data presented in this section are from experiments at FSU. The reaction data is from the ^{1}H(^{25}Al,p)^{25}Al* scattering experiment, using a 2.05-mg/cm^2 CH_2 target. The position sensitivity is tested using the ϕ angle coincidence between the light

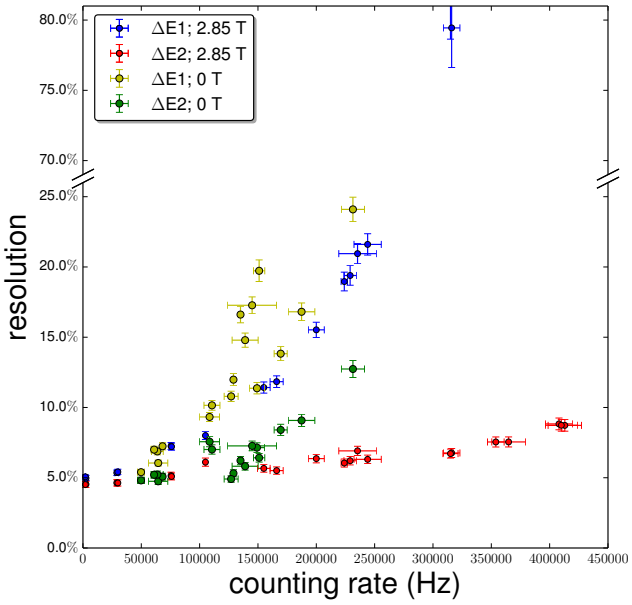

Figure 2.19: Comparison of resolutions of particle groups, with and without a 2.85 T magnetic field applied. The comparison includes peak fits from both ΔE1 and ΔE2 spectra.

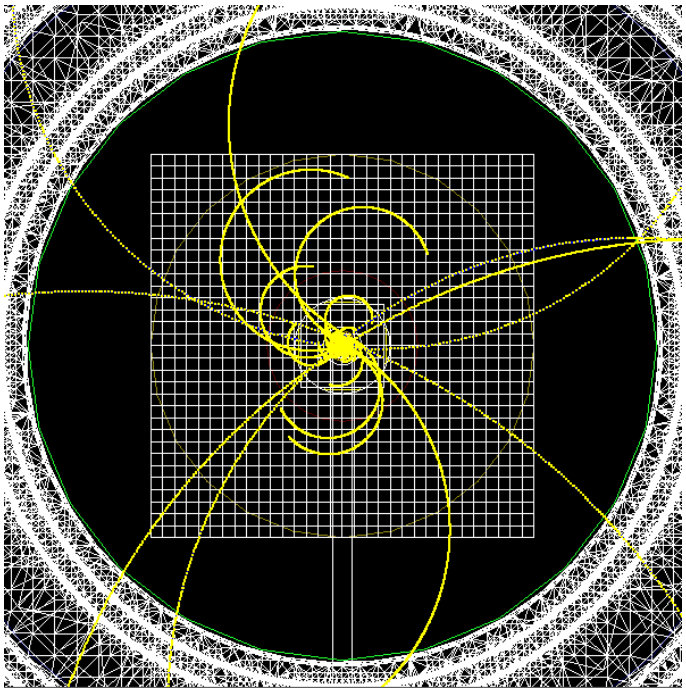

Figure 2.20: Simulation of particle trajectories from ^{12}C(^{28}Si,^{12}C)^{28}Si reactions in a magnetic field set at 2.85 T. Trajectories are focused back to beam axis to the magnetic field. The figure shows the view along the HELIOS axis from the downstream side.

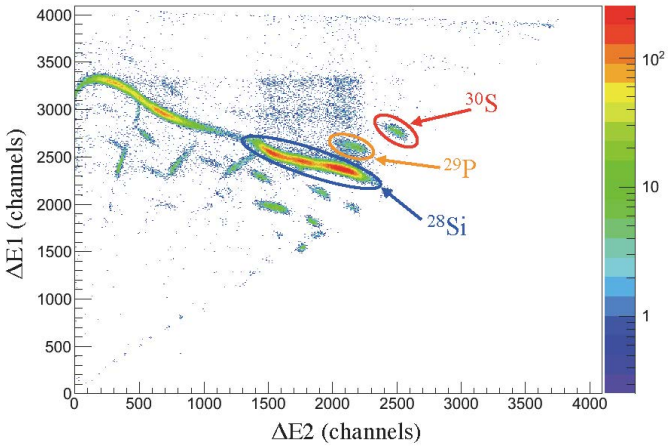

Figure 2.21: Particle ID spectrum from the ^{30}S beam production experiment. The ^{30}S beam is produced through the ^{28}Si(^{3}He,n) reaction. Particle groups of ^{30}S, ^{29}P and ^{28}Si are clearly separated and labeled.

and heavy ions as shown in Fig. 2.22.

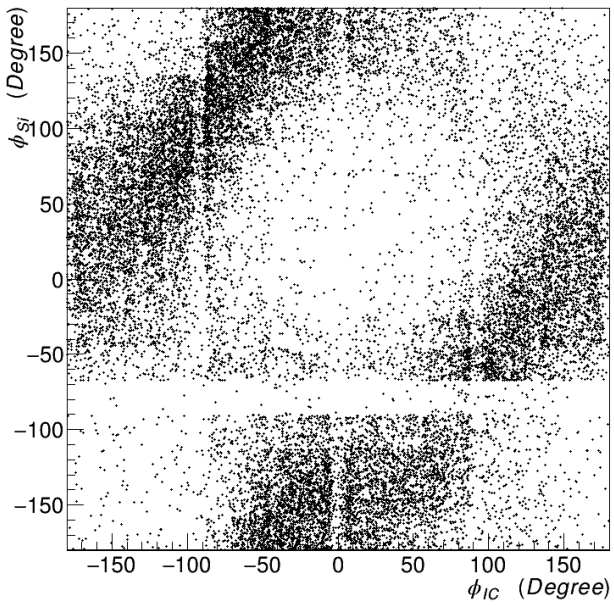

Figure 2.22: Linear correlation between the ϕ angle interpolated from position sensitive grids and ϕ angle detected by an annular silicon detector. These data are from the ^{25}Al(p,p)^{25}Al* scattering experiment at FSU. In the current algorithm, the detection position is obtained using a weighted average of the valid wire positions, which are adjacent and have output signals above threshold.

As mentioned previously, the position sensitive grids can also be used for suppressing pileup, which occurs when two events are detected very close in time. How-

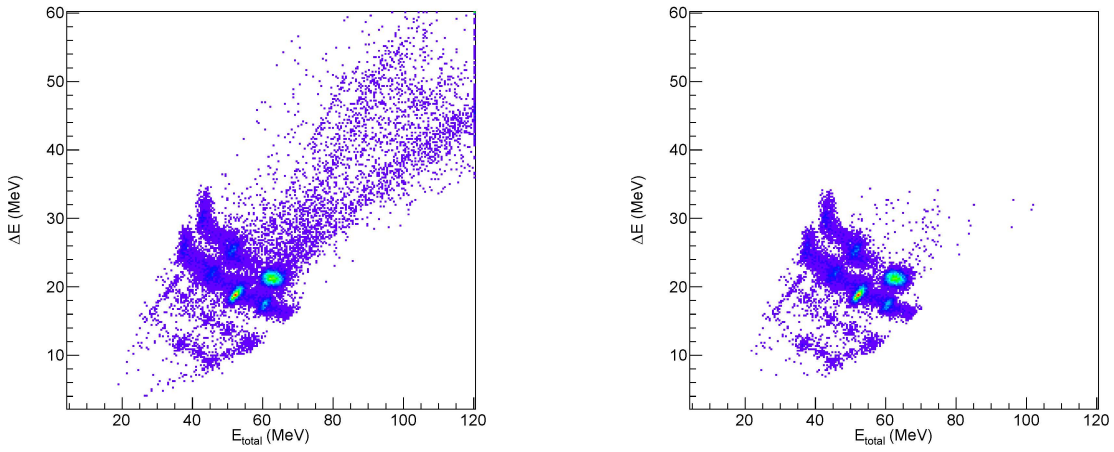

(a) (b)

Figure 2.23: Particle ID spectrum from the IC (a) without and (b) with cuts on data from position sensitive grids applied. The data are from an experiment at FSU measuring the ^{2}H(^{17}F,n)^{18}Ne reaction.

ever, if the two particles enter the chamber with a spatial separation larger than ∼6 mm in the XY plane, the position sensitive grids can be used to give information on multiple particle hits. Figure 2.23 is from a measurement of the ^{2}H(^{17}F,n)^{18}Ne reaction and shows that the cuts from the position sensitive grid data can effectively eliminate pileup.

The current algorithm and experimental procedures are described here. First, the calibration for each of the 64 channels comprising the X and Y position sensitive grids is performed by enforcing the same peak height voltage of each output signal with a pulser used for the input signal. When only one particle enters the chamber, the ionization charge due to this particle can be imagined as a thin cylinder with the axis lying along the particle's trajectory. Due to the finite dimension of the charge cylinder, it might cross multiple wires and, as a result, the charge is shared by several adjacent channels. Based on this physical model, the current algorithm looks for all signals above a certain threshold and sums up the adjacent signals. For a single particle detection scenario, only one result will be obtained and the summation should be proportional to the energy deposited by the particle. In the case of a pileup event, multiple ionization tracks will occur and the sum of all the charge collected will be approximately a multiple of the charge obtained for the one particle scenario.

This technique is useful in suppressing pileup for experiments detecting products from reactions in a non-magnetic environment, where recoils deviate from the beam particle trajectories by a few degrees. However, a magnetic field may refocus the recoil trajectories, which may cause poor spatial separation, and the technique may fail in a magnetic environment. This technique will also not be applicable in beam production tests and experiments detecting re-accelerated products, as all of the

particles follow the same trajectory (i.e. they are not spatially separated in x and y).

2.5 Electronics and Data Acquisition System (DAQ)

All energy signals pass through preamplifiers (shown as triangles in Fig. 2.24) and are further amplified and shaped into approximately Gaussian peaks by amplifiers. Mesytec multichannel amplifiers and Tennelec Amplifiers were used for the HELIOS Si detectors and the IC energy signals, respectively. Furthermore, the timing output signals from the Mesytec amplifier for all Si channels are combined into one Si timing through an "OR" module. The IC timing signal is produced by passing the split preamplifier signal from section 1 through a fast amplifier (fast amplifiers have a shorter response time) and a Constant Fractional Discriminator (CFD), which transforms the Gaussian-shaped signal into a timing signal. The Si timing and IC timing are further processed by a series of logic modules to produce the TAC (time to amplitude converter) signals (amplitudes correspond to the time difference between Si timing and IC timing), and triggers for the DAQ.

Signals collected by the data server include X_{near}, X_{far} and E_{back} from the silicon detector array, the timing signal between silicon detector array and the RF timing, the timing between silicon detector array and the first IC section, and all IC energy signals (data from both regular grids and position sensitive grids when in use). All analog signals are transformed into digital signals by Philips 7166H peak sensing analog-to-digital converters (ADCs) [61].

The DAQ (Fig. 2.24) is triggered by the OR of the timing signals from the silicon detector array and the downscaled signal from the first IC section. The IC counting rate is typically more than 100 kHz, which is orders of magnitude higher than the rates from the silicon detector array and this rate will overwhelm the data server. This prohibits triggering on the direct IC signal, but information about the beam components is useful to obtain as a reference point for data analysis and is also a good indicator of equipment performance. Thus, the downscaled timing signals of the IC are also fed into the trigger.

One key point is that the data server usually can not handle a high rate (more than a few kHz). When the data server is busy saving previous data, a veto signal is produced and fed into the DAQ system to prevent additional events from being processed. This causes an additional loss of efficiency. To compensate for the efficiency loss from this dead time, the raw trigger rate before the veto is recorded by a scaler. The live trigger rate also recorded by the scaler, and the ratio between these two rates is used to correct for this dead time in the calculation of the absolute reaction cross section.

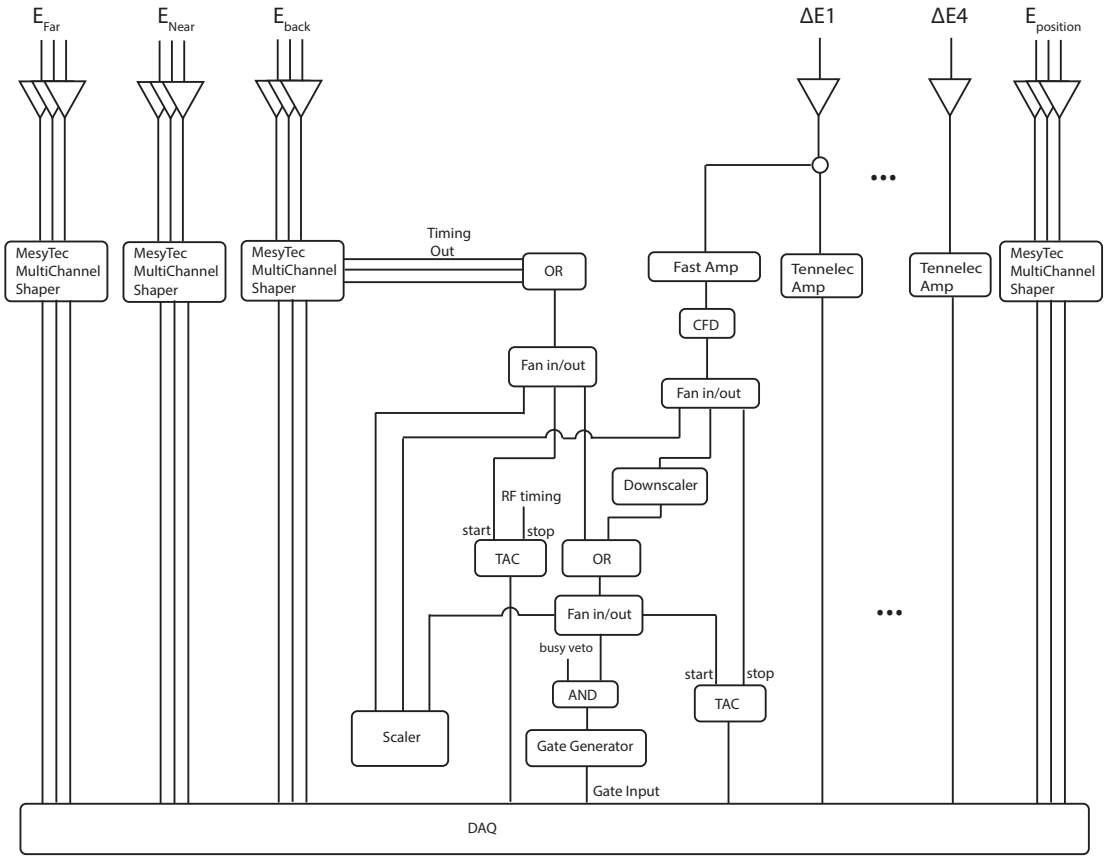

Figure 2.24: The electronics schematic showing the processing of detector signals between the detector outputs and the DAQ. See text for more details.

2.6 Experiment Overview

The full experimental setup described above was used to directly measure the ^{4}He(^{20}Ne,p)^{23}Na reaction in inverse kinematics in order to better understand Type Ia SNe nucleosynthesis. In Type Ia SNe with a typical white dwarf mass 1.2 $M_{\odot}$, the temperature range where (α,p) reactions are active is 2-5.5 GK [39]. Within this temperature range, Gamow peak energies and the corresponding beam energies needed in inverse-kinematics reaction experiments can be estimated using Eq.1.12. The estimated results are plotted in Fig. 2.25.

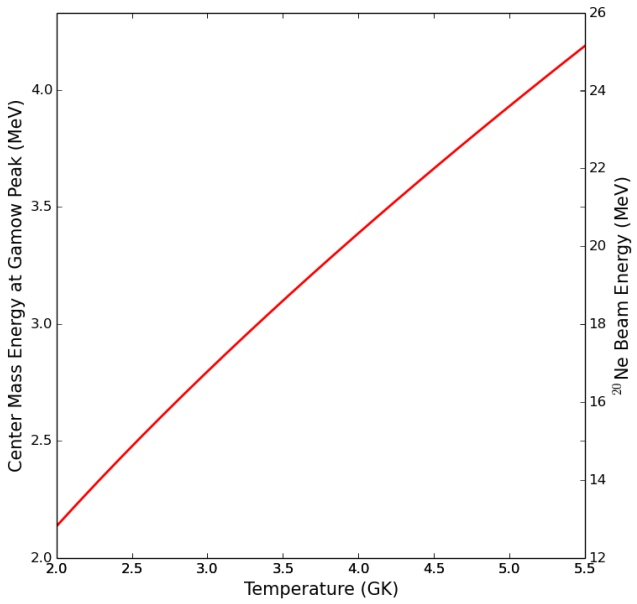

Figure 2.25: Gamow peak energy and the corresponding beam energy of ^{20}Ne in inverse kinematics setup vs temperature.

From the estimated results, ^{20}Ne beam energies at the reaction point of less than 24 MeV are needed to produce measurements in the astrophysically relevant energy regime. Unfortunately, reaction cross-sections at these low energies may be extremely small as the reaction energy is below the Coulomb barrier, making the measurement unfeasible due to the time needed to collect adequate statistics. Though calculating the exact barrier height can be complicated, an upper limit can be estimated by the following equation,

$$V_{\text{Coulomb}} = k\frac{Z_1 Z_2}{R_0} \tag{2.3}$$

$$R_0 = 1.2 \text{ fm } (A_1^{1/3} + A_2^{1/3}) \tag{2.4}$$

where Z_1, Z_2 (in C) and A_1, A_2 (in a.m.u) are the charges and masses for each reactant, respectively. As the strong force can actually extend beyond classical

radii, this calculation overestimates the barrier height and the result (5.6 MeV E_{cms} corresponding to a 33.6-MeV ^{20}Ne beam energy) can be used as an upper limit.

Considering this, we started with a high beam energy at 107 MeV (17.8 MeV E_{cms}), which is well above the upper limit of the Coulomb barrier calculated above, and took multiple measurements lowering the beam energy as far as possible. The measurements at high energy points also test the experimental setup with the Si array at the upstream position, which will be used in future (α,p) measurements. During the experiment, we successfully measured this reaction at ^{20}Ne beam energies at the reaction point as low as 30 MeV. Measurements with lower beam energies may be achieved, but were not attempted here due to the limited allocation of beam time.

The experimental data consisted of measurement attempts at three beam energies 107 MeV, 88 MeV and 40 MeV. Calculating the beam energy of the reaction point requires including the energy losses in the window foil of the target and gold foil if used. The beam energies at the reaction point for ^{4}He(^{20}Ne,p)^{23}Na were 100.2 MeV, 80.2 and 30.8 MeV.

As discussed, the experimental setup for the first experimental run consisted of the silicon detector array positioned upstream of the target position (Fig. 2.26a). In this setup, protons emitted at backward angles will be intercepted by the silicon detector array after one cyclotron orbit, and heavy recoils will be detected by the IC positioned further downstream (the configuration of the IC used for the first experimental run is shown in Fig. 2.27). The goal of this setup is to use coincidences between protons and heavy recoils for background elimination.

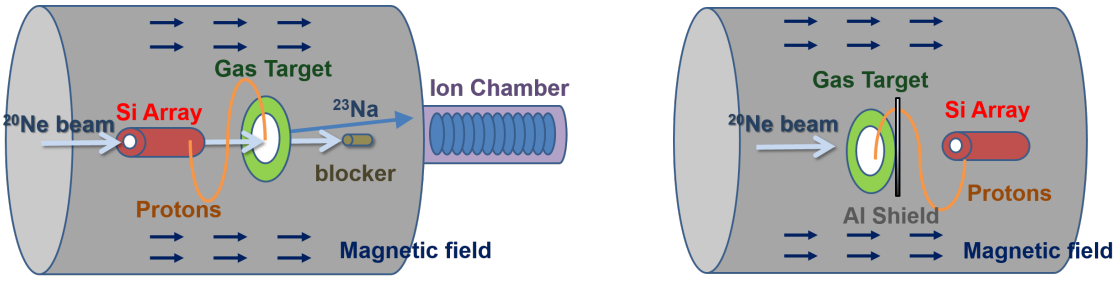

(a) (b)

Figure 2.26: Schematics of the two experimental setups. In setup 1 (a), the silicon detector array is placed at the upstream position relative to the gas target and the ionization chamber is in use. Setup 2 (b) is used for measurements with beam energies lower than 60 MeV at the reaction point, where the silicon detector array is moved to the downstream position. A thin aluminum foil is used in (b) to stop reaction products heavier than ^{4}He and the ionization chamber is removed.

However, as the beam energy decreases, the angles in the lab frame of the emitted protons from the ^{4}He(^{20}Ne,p)^{23}Na reaction will gradually shift from the backward direction to the forward direction and the proton spectrum will move toward the lower right side of Fig. 2.28. In order to achieve maximum coverage of protons, the position of the silicon detector array needs to be changed as the beam energy at the

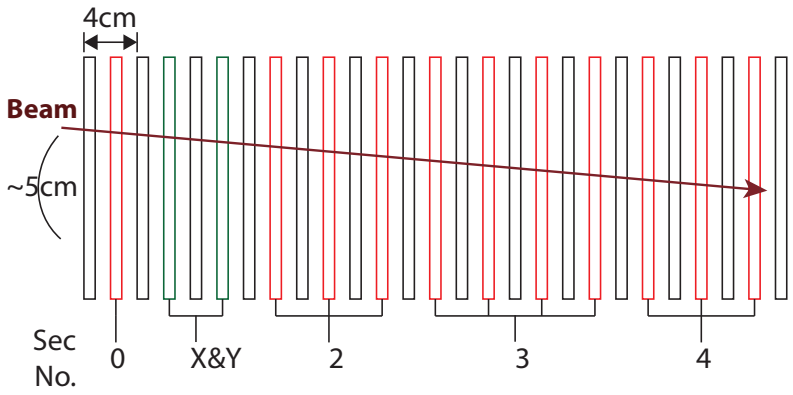

Figure 2.27: Setup of the IC for the first experimental run of the ^{4}He(^{20}Ne,p)^{23}Na experiment.

reaction point becomes lower than 60 MeV. Therefore, for the second experimental run, where E $\leq$ 60 MeV for ^{20}Ne, a different experimental setup was used where the Si array was located downstream of the gas target (see Fig. 2.26b). For this setting, the mount of the silicon detector array will block most heavy recoils and therefore, the ionization chamber was not used. In order to eliminate background despite the loss of the heavy recoil detector, a thin aluminum foil was added right after gas target (Fig. 2.26b). The Al foil (2.7 mg/cm^2) was chosen so that all heavy recoils would be stopped, while light particles, including α particles and protons, would pass through the foil without losing much kinetic energy. Additionally, a gold foil and a LL1 Si detector were installed with setup 2 to monitor the Rutherford scattering of the beam. However, due to complications from the magnetic field, this information was not used during the data analysis.

During the experiment using setup 1, the near side of the silicon detector array was 10 cm from the target frame, which was located at -10 cm with respect to the origin set at the center of HELIOS. The separation between the target frame and the near side of the silicon detector array was 25 cm during the experiment using setup 2.

For normalization and calibration purposes, the d(^{20}Ne,p)^{21}Ne reaction, ^{4}He(^{20}Ne,^{4}He)^{20}Ne scattering and d(^{20}Ne,d)^{20}Ne scattering were also studied during the experimental runs. The data acquired during these experimental runs and the subsequent data analysis will be discussed in the next chapter.

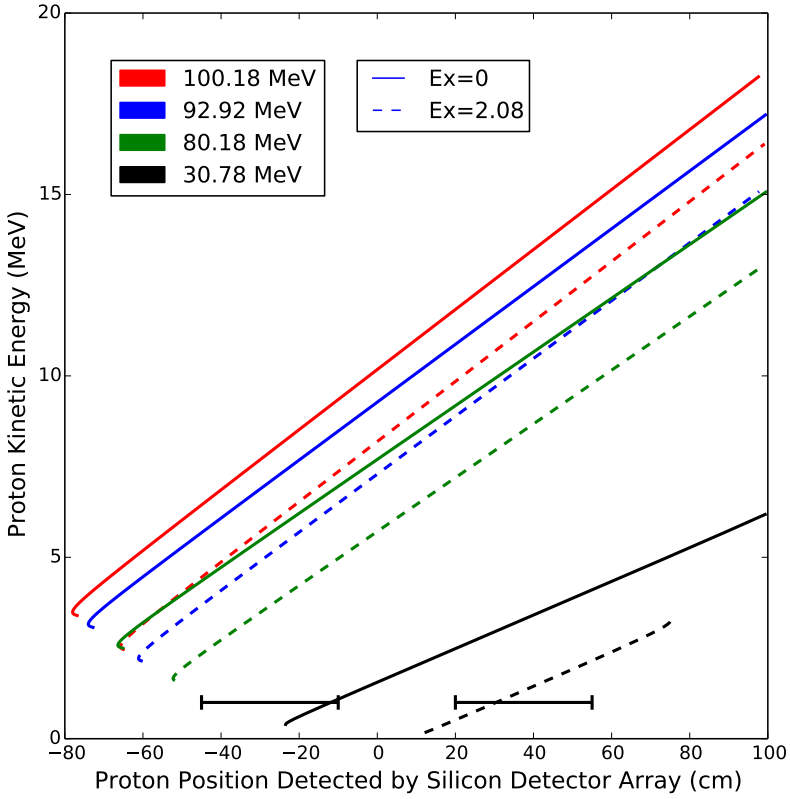

Figure 2.28: Calculation of proton energy vs the position of the protons after one complete cyclotron orbit for multiple beam energies from the ^{4}He(^{20}Ne,p)^{23}Na reactions. Both the ground state (solid line) and the Ex=2.08-MeV excited state (dashed line) spectrum lines are plotted. Lower beam energies will produce spectrum lines toward the lower right hand side of the figure. The target is placed at 0 cm. The segmented lines represent the positions of the Si array for both upstream and downstream setups.

Chapter 3
Data Analysis

3.1 Simulations

A large amount of effort was spent on accurate simulations of the experiment for each experimental setup. The two most important types of simulations are the light particle kinematics calculations and the Geant4 based [74] Monte Carlo simulations (e.g. to determine angular coverage). The kinematic calculations do not include any energy losses in the windows, gold foil or inside the targets, but the simulation results are accurate enough for calibrations using solid target data sets. Thus in Section 3.3, calibrated spectra are only compared with the kinematics calculations. However, energy spectra obtained with the gas target, can not be accurately reproduced with these kinematics calculations, as light particles lose a significant amount of energy exiting the exit window foil. In this situation, Monte Carlo simulations are used. Besides simulating energy losses in materials, the Monte Carlo simulations can reproduce complicated geometric structures of the devices, such as the HELIOS Si array, the gas target and the entrance of the IC. Those geometric shapes have a significant impact on geometric efficiencies.

3.1.1 Kinematic Calculations

A new tool was developed to simulate light particle energies and positions detected in the Si array. The code used for the kinematic calculations is written in Python and designed as a calculation website for HELIOS to obtain instant results. The web site is built using the Django framework and a snap shot of the user interface is presented in Fig. 3.1. This program stores the standard atomic mass compilation [75] in a SQLite database. The user end will automatically fetch new atomic masses from the database, once an atomic number is input to the program. A list of options can be entered, including the display energy range and the position range. The graphic end displays data in interactive charts based on Highchart (a javascript interactive chart), which also provides options for downloading the figures in multiple formats.

The calculation part of the program consists of two major parts: the reaction calculation and the trajectory calculation. The kinematic properties are calculated using relativistic formulas, and a Q value input is not needed. Details of the calculation can be found in any elementary special relativity text book. Calculations are performed for the reaction at one degree intervals in the CMS frame. The reaction calculation results, including angles and kinetic energies for heavy recoils and light

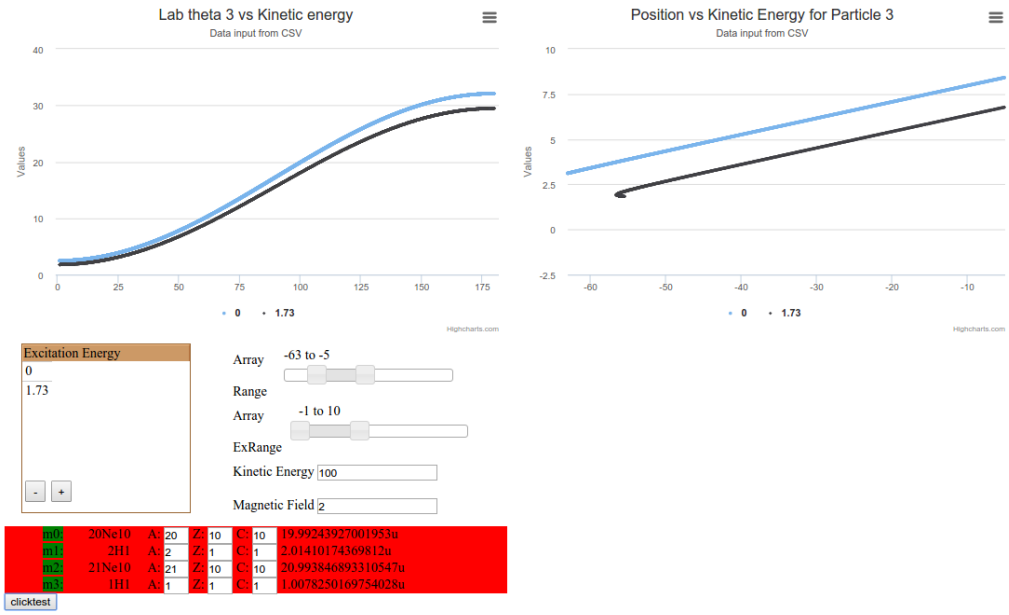

Figure 3.1: User interface of the kinematic calculation web site (http://tbjctest.appspot.com/HELIOS/). In this specific calculation, proton lines from ^{2}H(^{20}Ne,p)^{21}Ne reactions at two excitation energies (0.35 MeV in blue and 1.73 MeV in black) are calculated using an 100-MeV ^{20}Ne beam energy.

products, are then imported into trajectory calculations, which will return proton energies and positions in the HELIOS Si array.

3.1.2 Monte Carlo simulations

A more sophisticated Monte Carlo simulation was developed using the Geant4 toolkit for the needs of calculating geometric efficiencies and energy losses through the target materials.

The basic steps of the program are described here. The program runs the reaction process in a loop, which consists of three stages. In the first stage, a beam particle is created. The beam particle enters the target region and randomly triggers a reaction. The probability of triggering a reaction is uniformly distributed across the target depth and is pre-set by the user. The CMS angles and the excitation energies of the recoils are also randomly generated, according pre-defined distributions. In the simulations presented in this thesis, each excited state is equally generated and an isotropic CMS angular distribution is adopted. If a reaction is triggered, a reaction flag will be set for the next stage. If the beam particle does not trigger a reaction it continues through the target and either enters the IC or is stopped by the HELIOS flange. The energy deposited in the IC by a beam particle is recorded as energy from "scattered beam". If the first stage finishes without a reaction flag being set, the program will directly start another loop after the scattered beam particle is recorded and repeat the same stage again.

After finishing the first stage with a reaction flag set, the program will start the following two stages sequentially by shooting reaction products from the position where the reaction flag was set. The kinematic properties of the two reaction products are calculated through the same kinematic calculation method described in Sec. 3.1.1. This kinematic calculation assumes a uniform angular distribution in the CMS frame, and the statistics detected in each detector merely reflect the geometrical efficiency instead of cross section information.

Geometric volumes in this simulation mimic the exact dimensions of the experimental devices, including the Si array, the IC and the gas target. An overview of the layout of the devices used in the simulation is presented in Fig. 3.2a and a detailed view of the gas target and the Si array is also shown (Fig. 3.2b). The dimensions of the array are taken from J. C. Lighthall's thesis [76]. The complicated shape of the front flange of the IC, which is important in determining the acceptance of heavy recoils, is reproduced by importing the Computer-Aided Design (CAD) file using CADMesh. The shape of the gas target is carefully designed to reproduce the geometry of the real gas target as closely as possible. A schematic of the gas target model is shown in Fig. 3.3. The simulated gas target consists of two circular titanium metal flanges separated by a gap with a depth that is preset by the user (a 1-mm gap is used for this experiment). Between the two titanium pieces is a layer of target gas, sandwiched by two hemispheres of gas to mimic the bowing out of the gas cell windows. The curved surfaces of the hemispheres are covered with a thin window foil. The size of the sphere is determined by a preset user input "$f_{\text{bowing\_out}}$" factor (larger $f_{\text{bowing\_out}}$ means more "bowing out"). This factor is illustrated in Fig. 3.3 and is used to calculated the extruding length t:

$$t = r - \sqrt{r^2 + (\frac{D}{2})^2}, \tag{3.1}$$

where $r = f_{\text{bowing\_out}} \frac{D}{2}$ and D is the diameter of the aperture. Fig. 3.3b is a snapshot of the gas target with $f_{\text{bowing\_out}} = 0.9$ (for illustration purpose). The $f_{\text{bowing\_out}}$ factor will affect the target thickness, and measurements show that the bowing out adds an additional $\sim$1 mm to the target thickness when a Kapton foil (7 μm) and 500 Torr gas is used. This effect will be cancelled out in the normalization method used in Sec. 3.4.1, as the extra thickness exists for both the (α,p) and the calibration reaction. The simulation parameters for the gas target include gas pressure, gas species, window foil material, window thickness and the sphere bow out factor, and can be preset through the user input file, which is written in JavaScript Object Notation (JSON) format.

This Geant4 simulation can reproduce the proton spectrum measured in the Si array using the modeled gas target with good accuracy, and it also serves as a guide to the first preliminary particle ID cuts by predicting the energy losses of the heavy recoils relative to the scattered beam (Fig. 3.4).

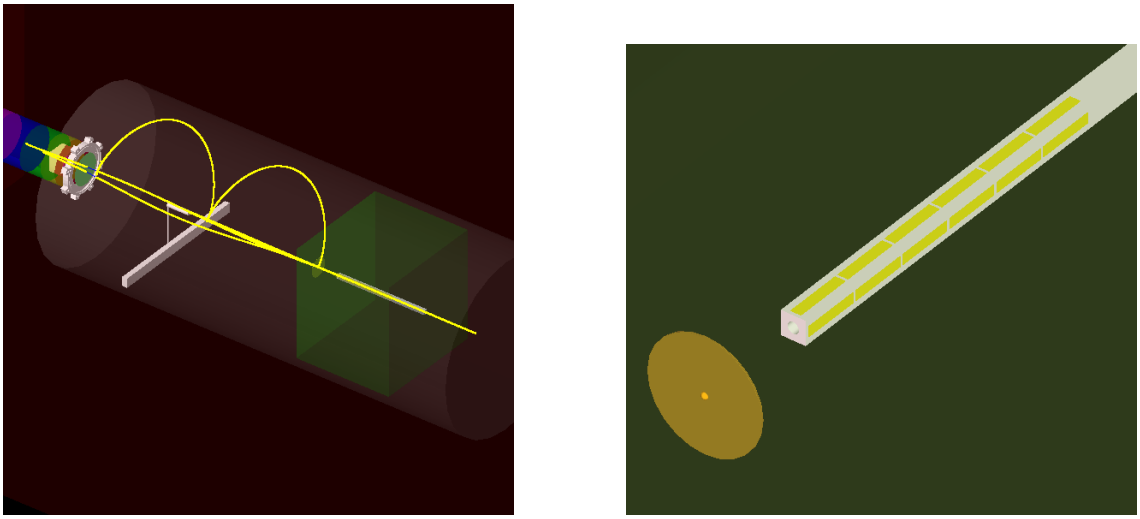

(a) (b)

Figure 3.2: (a) An overview of the Monte Carlo simulation program. The bright yellow lines are the trajectories of ^{20}Ne particles. (b) A close-up view of the gas target and Si array.

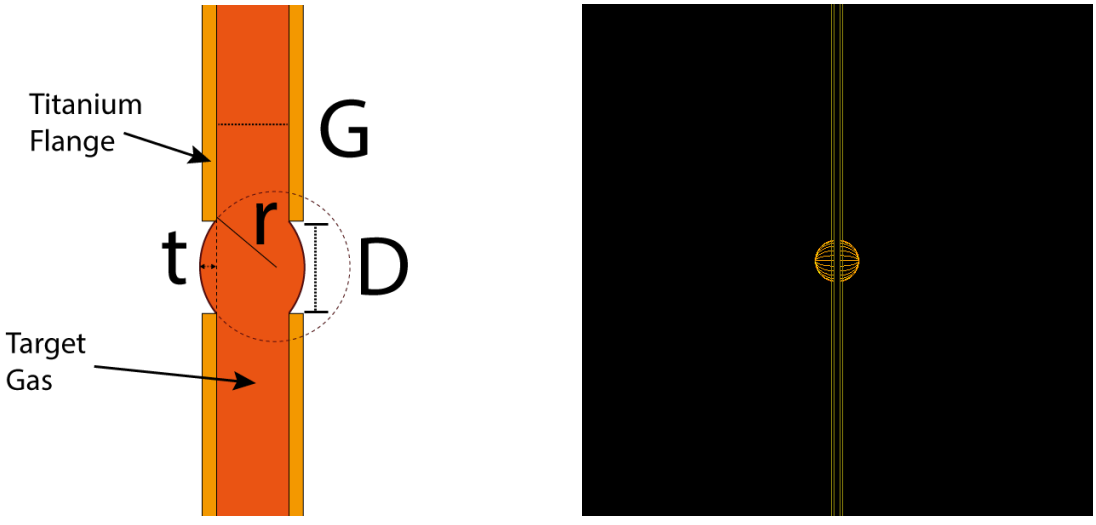

(a) (b)

Figure 3.3: (a) Schematic of the gas target model used in the Monte Carlo simulations and (b) a snapshot of the gas target model with $f_{\text{bowing\_out}} = 0.9$. In the plot, G is the gap width and is not used for cross section calculations.

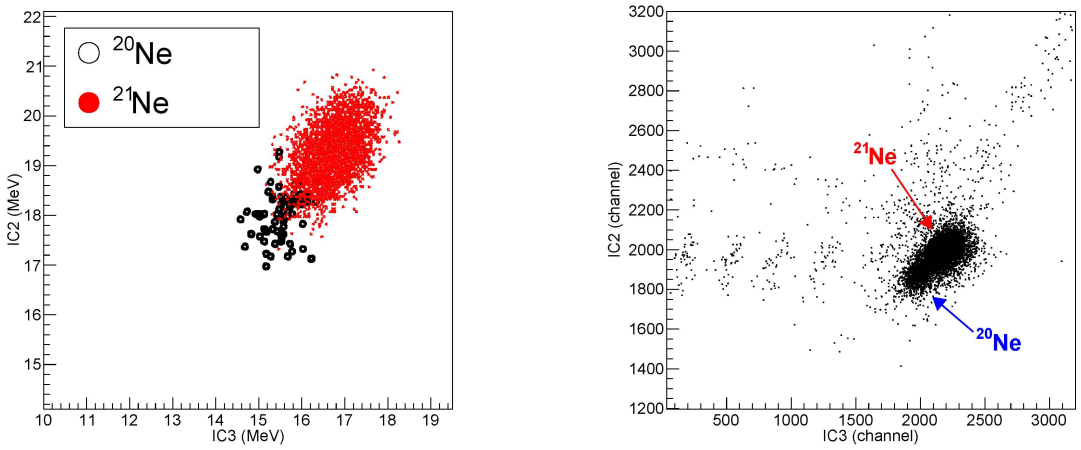

(a) (b)

Figure 3.4: (a) Simulation results of energy deposited in section 2 vs 3 of the IC for ^{2}H(^{20}Ne,p)^{21}Ne using a 107-MeV ^{20}Ne beam and a 131-μg/cm^2 solid target. (b) Spectrum of section 2 vs. 3 of the IC for experimental data from the same reaction and settings.

3.2 DWBA calculations

In this experiment, the statistics obtained from the ^{4}He(^{20}Ne,p)^{23}Na measurement using the first experimental setup are normalized to the ^{2}H(^{20}Ne,p)^{21}Ne reaction (normalization method will be described in Sec. 3.4.1), in order to calculate cross sections. However, no published (d,p) reaction cross sections are available at the energies measured during this experiment. Thus cross sections are obtained from DWBA (Distorted Born Wave Approximation) calculations using Ptolemy [77].

In the DWBA calculation, the optical model parameters of the ^{20}Ne-d interaction are obtained from a published global potential set by An et al. [78], and the p-^{21}Ne potential parameters are taken from Koning et al. [79]. After the calculation, spectroscopic factors taken from National Nulcear Data Center (NNDC) [80] are applied to all cross section data (Table 3.1).

The DWBA calculation is validated using previously published results at other energies. Currently, two publications [81, 82] are available, which measured the ^{20}Ne(d,p) reaction at energies close to those used during our measurements. Heikkinen et al. performed these measurement with 8, 12 and 14 MeV deuteron beams, but only 12 MeV data with two excited states of ^{21}Ne (0.35 and 2.8 MeV) were presented in the paper. In another publication by Datta et al., this reaction was measured with an 11-MeV deuteron beam and the first three excited states were populated. As no quantitative results are provided in either of the two publications, the cross sections are extracted using the graphic tool "WebPlotDigitizer" [83].

The extracted values are then compared to the DWBA calculations using Ptolemy (Fig. 3.5). Figure 3.5 shows that the DWBA calculations can reproduce experimental measurements at low CMS angles with good agreement, but the deviation

Reaction	E_x (MeV)	spin	Spectroscopic Factor [80]
^{2}H(^{20}Ne,p)^{21}Ne	0	1d $\frac{3}{2}$+	0.03
	0.35	1d $\frac{5}{2}$+	0.62
	1.73	2s $\frac{1}{2}$+	0.11
	2.80	2s $\frac{1}{2}$+	0.8
	3.73	1d $\frac{5}{2}$+	0.03

Table 3.1: A summary of the parameters of the ^{21}Ne states used for normalization.

becomes large at angles of θ_{cm} >60°. As our experiment measures the (d,p) reaction at low CMS angles (up to 43° for the first experimental setup), DWBA calculations can be used reliably for the cross section normalization.

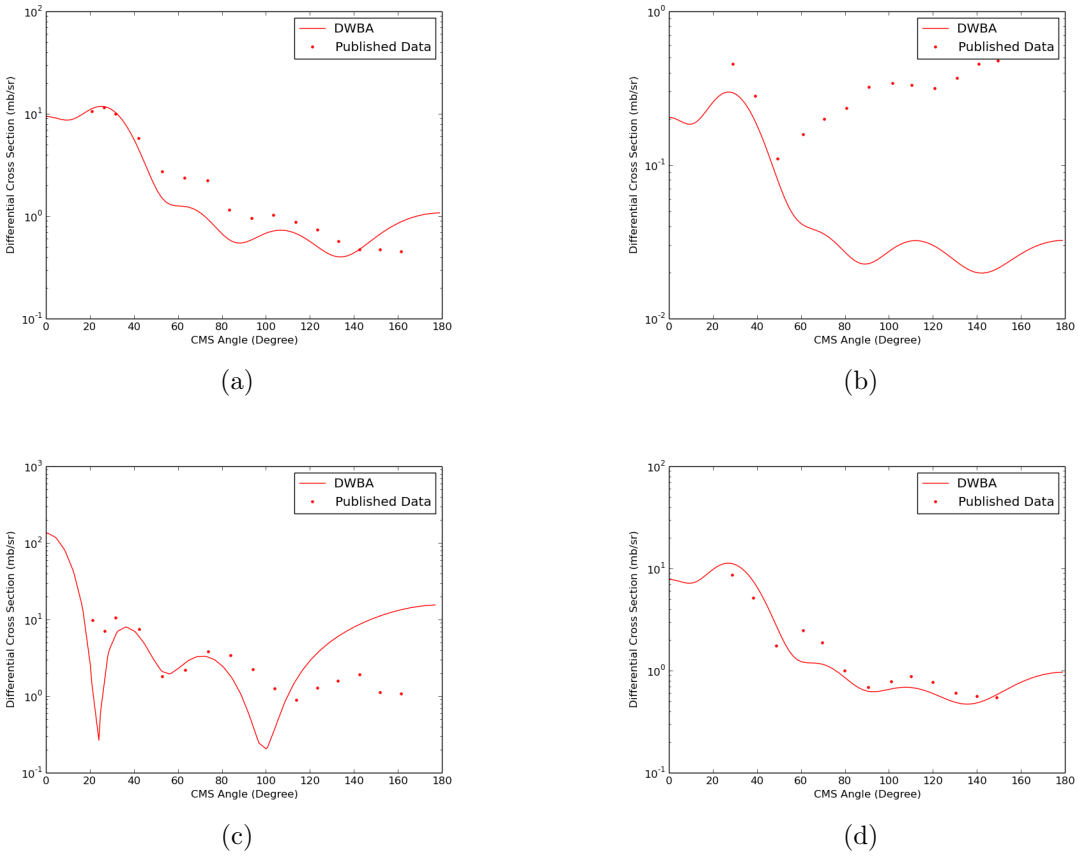

Figure 3.5: A reproduction of the published data and our DWBA calculations for the (a) 0.35-MeV and (c) 2.80-MeV states in ^{21}Ne measured by Heikkinen et al. using a 12-MeV deuteron beam and the (b) ground state and (d) 0.35-MeV state in ^{21}Ne measured by Datta et al. using an 11-MeV deuteron beam.

3.3 Calibration

The calibration procedure consists of several major stages: the preliminary calibration of the energy and position spectrum for the Si detector array using a mixed ^{148}Gd and ^{244}Cm α-source; a fine-tuned energy calibration using (d,p) and (d,d) measurements; TAC timing (between Si detector array and IC detector) alignment; and RF vs. x curvature correction and RF timing calibration.

3.3.1 Si Detector Array α Calibration

The Si detector array in HELIOS is primarily used for detecting light particles, including ^{2}H, ^{1}H, ^{3}He and ^{4}He. Each of the 4×6 detectors produces three signals: near (E_{near}), far (E_{far}) and back (E_{back}) signals. Ideally the charge collected from the back side should be equal to the sum of the near and far signals, which are collected from the front side. However, signal amplitudes can be shifted relative to one another due to different settings in the electronics or different sensitivities of the detectors. Raw spectra of the four sides of the Si array before calibration are presented in Fig. 3.6, where the two energy peaks (5.80 MeV and 3.18 MeV) from the alpha source are misaligned and the positions of the six detectors on each side of the array overlap at some points.

Software was developed to perform the calibration using alpha source data (Fig. 3.7). This software handles both position and energy calibrations. For the position calibration, a linear regression is performed using Eq. 3.2, and a set of parameters of A_{near}, A_{far} and b are returned for each detector segment.

$$E_{back} = A_{near}E_{near} + A_{far}E_{far} + b. \tag{3.2}$$

With the parameters from the regression, calibrated near and far signals can be obtained,

$$E_{far\_cal} = A_{far}(E_{far} + \frac{b}{A_{near} + A_{far}}) \tag{3.3}$$

$$E_{near\_cal} = A_{near}(E_{near} + \frac{b}{A_{near} + A_{far}}), \tag{3.4}$$

and the local position can be calculated using the following equation,

$$X = \frac{L}{2}[1 + \frac{E_{far\_cal} - E_{near\_cal}}{E_{back}}], \tag{3.5}$$

where L is the length of the detector.

After the position calibration, back signals for each detector segment are fed into a one-dimensional histogram, and the histogram is fitted with a double exponentially modified Gaussian distribution function. The equation for a single exponentially

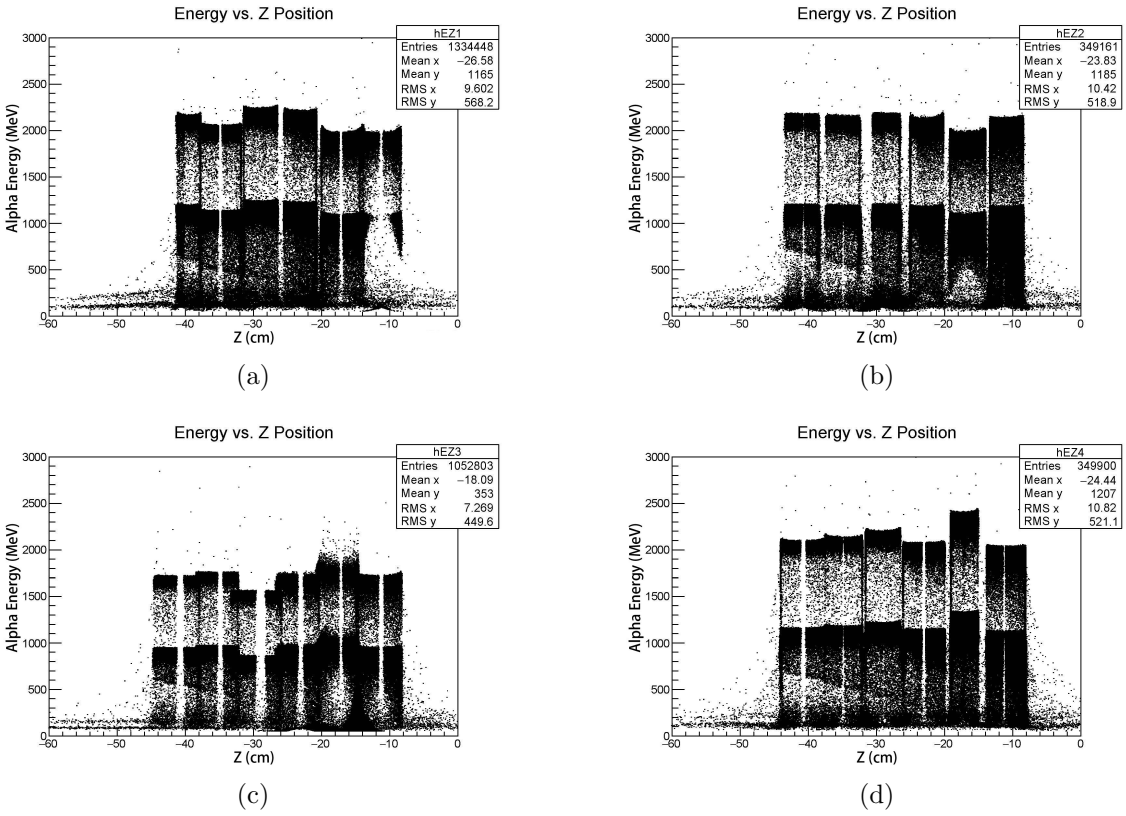

Figure 3.6: Uncalibrated data from the α-source for each side of the Si array.

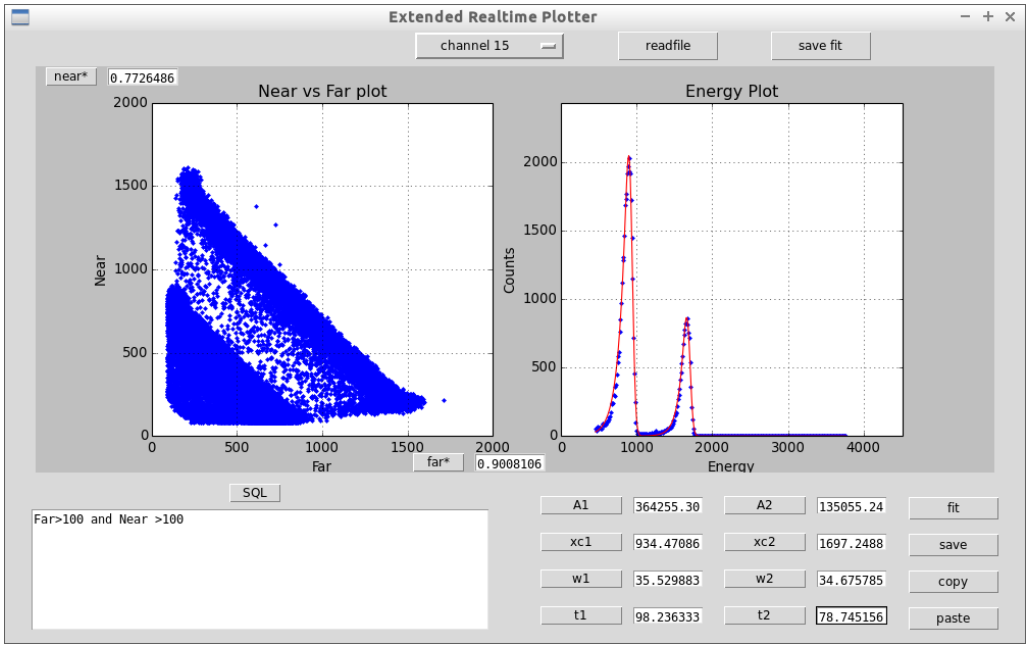

Figure 3.7: User Interface for α calibration software.

modified Gaussian distribution is given below,

$$f(x;\mathrm{A},x_c,w,\tau)=\mathrm{A}\frac{1}{2\tau}e^{\frac{1}{2}(\frac{w}{\tau})^2+\frac{x-x_c}{\tau}}(1+\mathrm{erf}(\frac{1}{\sqrt{2}}(-\frac{x-x_c}{w}-\frac{w}{\tau}))), \tag{3.6}$$

where most parameters do not have a obvious meaning, but x_c from the fitting is used as the peak position. Once the peak positions are obtained for both peaks (x_c for each peak are labeled as x_{c1} and x_{c2}), x_{c1} and x_{c2} are scaled to match the α-particle energies from decays of ^{148}Gd and ^{244}Cm using a linear fit, which yield another set of fitting parameters: the slope k and residue b. Finally, the slope k and residue b are applied back to the data and the α source calibration is complete. After this first stage of calibration, the α spectra show good alignment to the known α decay energies (Fig. 3.8).

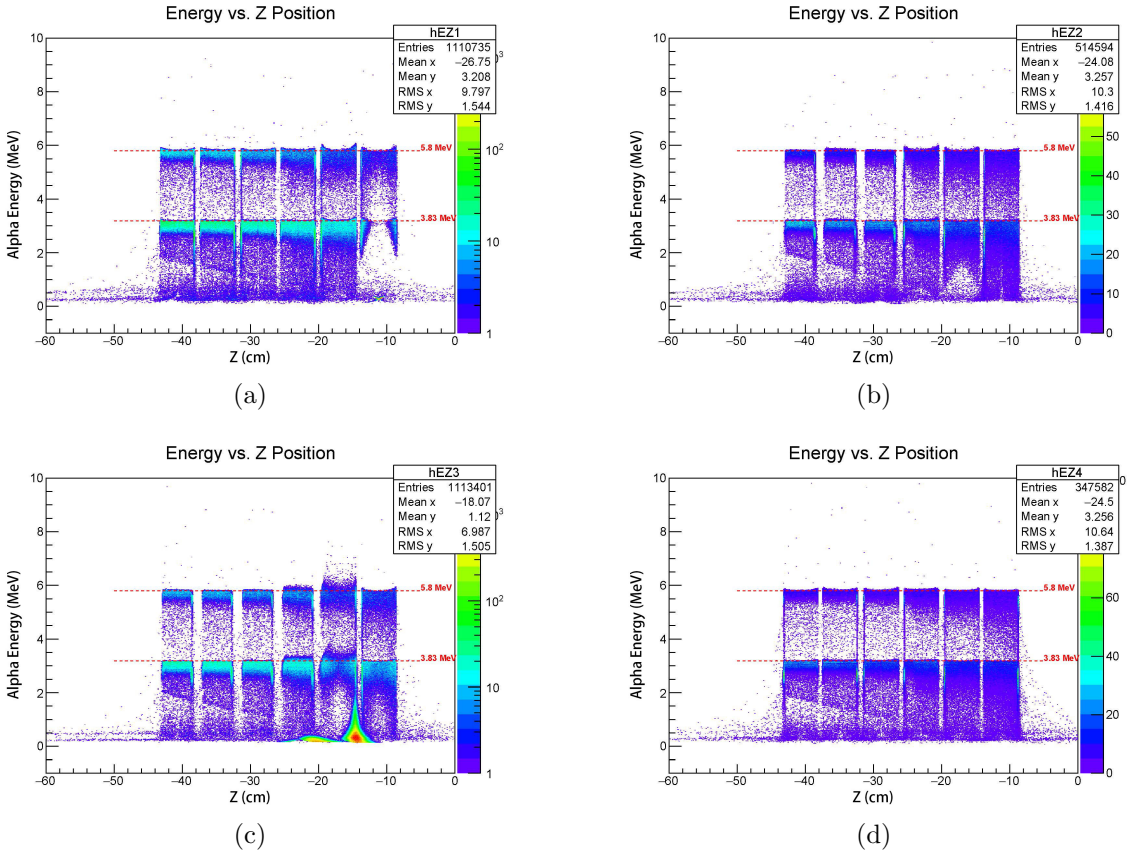

Figure 3.8: Alpha spectra of the four sides of the Si array after the first stage of calibration. The bin content in (a) and (c) was set to be on a log scale for visualization.

3.3.2 TAC alignment using the ^{20}Ne(d,p)^{21}Ne spectrum

The TAC signal is proportional to the time difference between particle detections in the Si detector array and the IC. Gating on this spectrum is important for suppressing background. However, the raw TAC spectrum shows an unexpected double-peaked structure when a single coincidence peak is expected (Fig. 3.9a). This feature is caused by misaligned timing signals from each Si detector segment and can be clearly seen in the 2D TAC spectrum (Fig. 3.9b), where the y axis is the segment number of the Si detector. This misalignment can be corrected by adding a shift factor to the TAC signal for each detector segment, which is obtained by fitting the TAC peak with a Gaussian function for each Si detector.

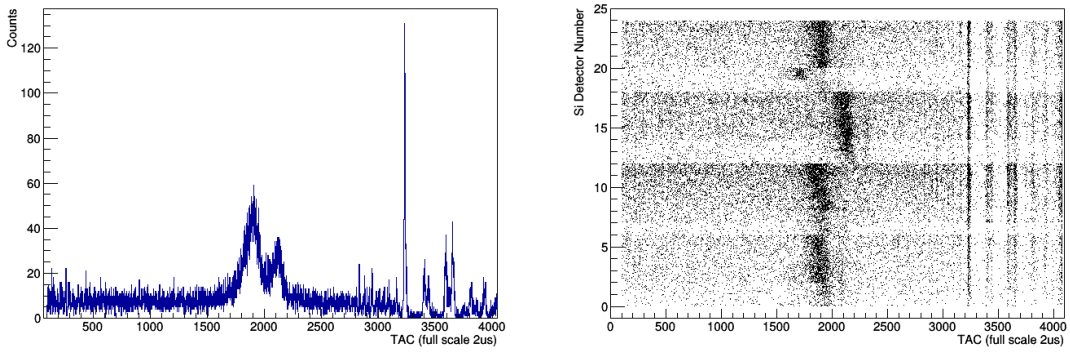

(a) (b)

Figure 3.9: 1D and 2D spectra of raw TAC signals.

After applying the shift factors, the timing of each Si detector relative to the IC (i.e. the TAC signals) are well aligned (Fig. 3.11a) and the background in the proton energy vs. position spectrum is significantly suppressed with a (TAC) timing gate from channels 1700 to 2100 in the corrected TAC spectrum (Fig. 3.11b).

3.3.3 Calibration of the x vs RF Spectrum

The TAC timing cut alone is not enough to sufficiently clean up the background in some cases, especially in the second experimental setup used for the lowest energy data, where the IC was not installed and the TAC signals were not available. The RF timing spectrum is another important tool to reduce background, and this spectrum can also be used to distinguish protons from deuterons/alphas. This allows protons and alpha particles from the (α,p) reaction and (α,α) scattering, respectively, to be distinguished from one another and is important for the cross section normalization of the lowest energy data point.

The RF timing is the time difference between particle detections in the Si array and the accelerator RF timing signal. As the accelerator RF signal is a constant periodic signal with an 82-ns period, the RF timing essentially measures the travel

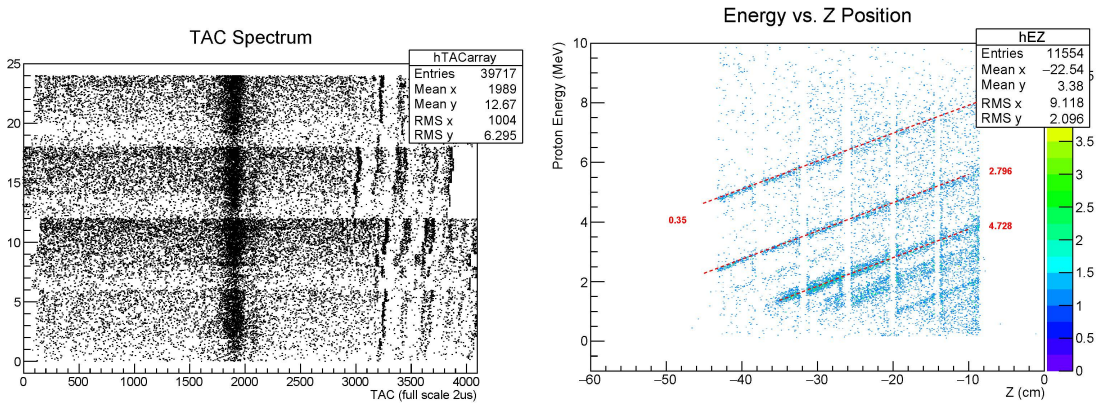

(a) (b)

Figure 3.10: (a) Aligned 2D TAC spectrum and (b) proton energy vs. position for states in ^{21}Ne populated via ^{2}H(^{20}Ne,p)^{21}Ne after gating on the TAC peak.

time of the light particle from the target to the detector, which can be calculated by the cyclotron period equation,

$$T = \frac{2\pi m}{qB} \tag{3.7}$$

(q and m are the charge and mass of the particle, respectively, and B is the magnetic field), which is a constant for particle species with a specific m/q. However, when the Si array detects a particle, the time needed to collect all the charge ionized by the particle can be different depending on the particle's position in the detector. This position dependence produces a curved shape for the RF timing as a function of position in the detector, x, for a specific particle species (Fig. 3.11) and different curves are produced for different particle species. As mentioned, the RF timing is a periodic pulse for each ∼82 ns, thus the RF timing can loop around in the time interval range plotted in an RF spectrum. Thus, some curves can be split into two halves at the edges of the RF spectrum range, which makes the calibration more difficult. To solve this difficulty, each RF timing signal is cloned and the clone is shifted by 82 ns so that a complete curve can be observed for all species (Fig. 3.11).

An example of the RF timing calibration is illustrated using data from measurements using the 2nd experimental setup and a 40-MeV ^{20}Ne beam. The main reactions measured during this experiment include ^{20}Ne(d,p)^{21}Ne, ^{20}Ne(d,α)^{18}F and ^{20}Ne(d,d)^{20}Ne, using a solid CD_2 target. By gating on different curves and comparing the resulting Si energy vs. position spectra with simulations, proton and deuteron/^{4}He RF timing (RF timings for deuteron and ^{4}He are the same) lines can be identified. Once identified, the proton curve in the x vs. RF spectrum is fitted with a 4th order polynomial series and the coefficients are used to correct the curves into straight lines. After the curvature correction, the RF timing lines in different Si detector segments are aligned using the method described in Sec. 3.3.2.

The majority of the background can be eliminated using both RF timing and

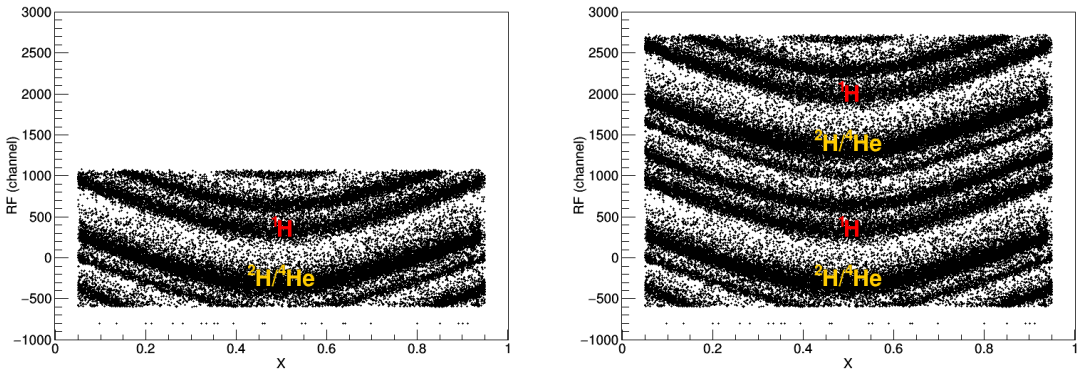

(a) (b)

Figure 3.11: Uncalibrated x vs. RF spectra (a) before and (b) after duplication. Proton and deuteron/helium RF timing curves have been identified and marked in the spectra.

TAC timing cuts, and then a more detailed calibration of the Si energy vs. position spectrum was performed using the (d,p) reaction data, as the proton lines in the (d,p) reaction typically have better energy resolution. However, the same method utilized for the alpha calibration discussed above was used for this (d,p) calibration, thus the details are not discussed here. The quality of the RF timing calibration and the (d,p) calibration is illustrated in the comparison between the experimental and simulated spectra with both (d,d) scattering and the (d,α) reaction data (Fig. 3.12).

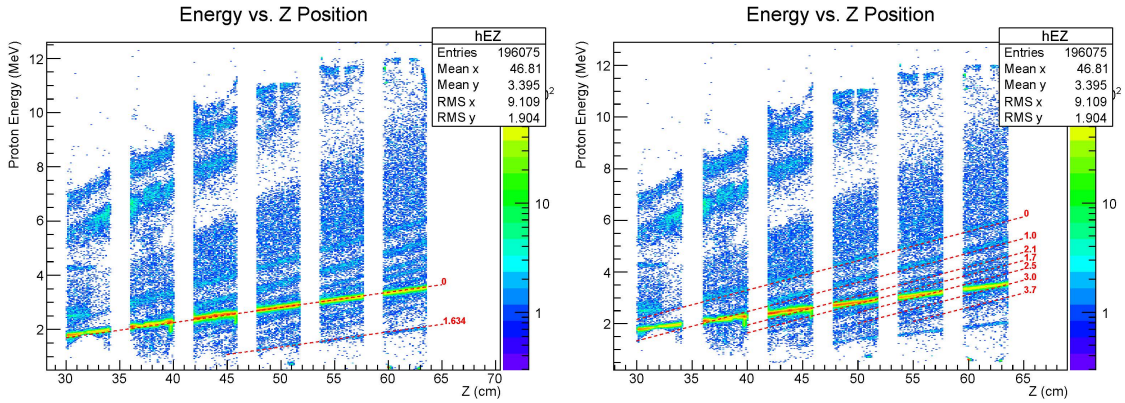

(a) (b)

Figure 3.12: Spectra of (a) (d,d) scattering and (b) the (d,α) reaction after gating on the deuteron/alphas RF timing. The experimental spectra are compared to simulation results, which are shown by red dashed lines. These experimental data are from the second experimental setup with an 88-μg/cm^2 solid CD_2 target and a 40-MeV ^{20}Ne beam.

3.4 Data Processing and Cross Section Calculation

3.4.1 Overview

Spectra and Cuts

The types of cuts used to analyze the three types of data-sets (data from measured ^{2}H(^{20}Ne,p)^{21}Ne with both gaseous and solid targets, and ^{4}He(^{20}Ne,p)^{23}Na with the gas target) using experimental setup 1 are the same. There are two basic types of cuts: 1. cuts on the RF vs TAC spectrum; 2. cuts on the particle ID spectra, namely cuts on energy losses in ionization chamber. For experimental data obtained using setup 2, only the RF timing spectrum will be used to clean up the data.

The RF timing signals in HELIOS have very good resolution (7.3 ns FWHM and 2.6% of the spectrum range in Fig. 3.13), and this timing is directly related to proton cyclotron period, which does not depend upon the energy of the particles. As mentioned previously in Sec. 3.3.3, by gating on RF timing, protons and deuterons/alphas can be selected. Furthermore, this cut can significantly remove background.

The TAC spectrum records the timing difference between particle detections in the HELIOS Si detectors and in the IC. For data-sets with solid targets, most background is removed by gating on the TAC peak. However, the TAC spectra are usually heavily contaminated by scattered beam and byproducts from fusion evaporation reactions and the coincidence peaks may be overwhelmed by heavy background when the gas target is used. A preliminary gate on the proton RF timing can help resolve the TAC peak of interest. The peak resolution in the TAC spectrum is 72.2 ns and 3.0% of the full TAC range (Fig. 3.14). As the timing resolutions are good in both the RF and TAC spectra, it is preferable to apply stringent cuts on the RF vs. TAC spectra.

By contrast, the energy loss spectra from the IC have relatively poor resolution and the shapes of the particle groups can be hard to predict. Thus, the cuts on the particle ID spectra need extra attention and should always be applied after all the other cuts have been implemented. The Monte Carlo simulations can be used to roughly estimate the relative position between scattered beam and recoils, and to predict the shapes of the particle groups. The simulations can also be used to guide the first preliminary cuts on the particle ID spectra. As an example, the particle ID spectrum for the ^{4}He(^{20}Ne,p)^{23}Na data set is presented, where the ^{20}Ne is already identified and marked with a blue polygon in the spectrum, along with the Monte Carlo simulations (Fig. 3.15). The simulations show that ^{23}Na particles deposit more energy in IC sections 1 and 2 than the ^{20}Ne particles do, which matches the experimental data.

Efficiency Corrections

Because of the finite processing time of the DAQ and limited geometric coverage of the detectors, statistics collected from these experiments need to be corrected for a variety of efficiencies. The efficiency corrections in this experiment come from four

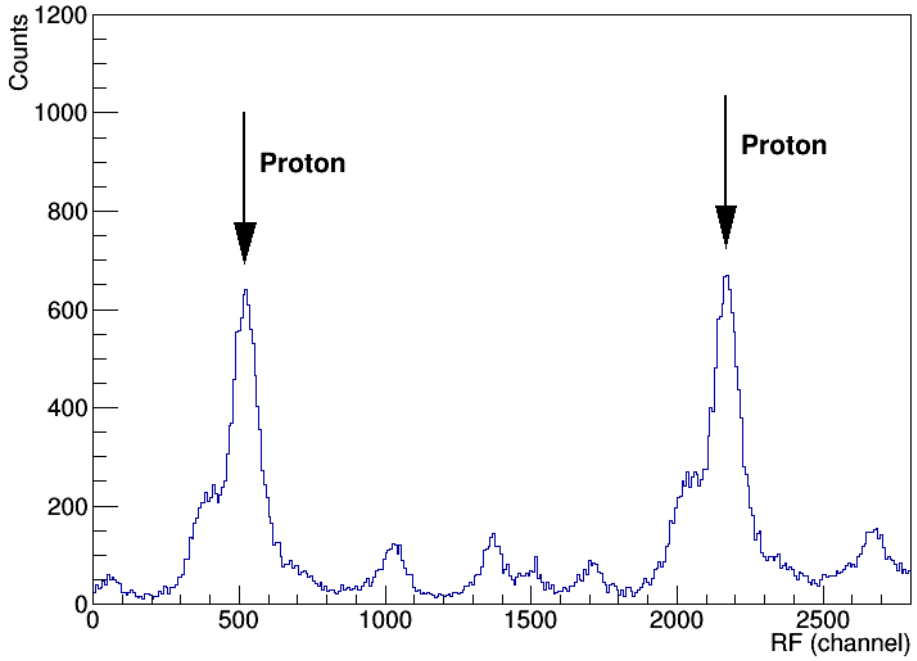

Figure 3.13: Spectrum of the timing between the RF of ATLAS and particle detections in the HELIOS Si array.

categories: dead time correction, ADC pileup correction, wire interception correction and solid angle coverage correction.

In the data collection stage, an event where more than one signal is collected within one gate of the ADC is referred to as "ADC pileup". The ADCs were set to peak sensing mode, where the ADC will scan for the highest voltage over a specified range in time ($\sim$2 μs). In the case of multiple signals within one gate, if the amplitudes of the recoil signals are smaller than those produced by background, such as the scattered beam, the recoil signals will be disregarded and this will result in only the events with larger signal amplitudes being recorded in the particle ID spectra. Thus, if events in the recoil particle group of interest have smaller signals than those in a more intense particle group, one particle ID spectrum cut may not include all of the recoil particles of interest and this "ADC pileup" efficiency loss needs to be corrected. The efficiency can be calculated using the following formula,

$$\varepsilon_{\mathrm{NotPileup}} = (1 - p_{\mathrm{scatter}})^N \tag{3.8}$$

$$= (1 - I_{IC} * 82ns)^N, \tag{3.9}$$

where p_{scatter} is the probability that the IC will detect an event for each beam pulse, I_{IC} is the IC counting rate, which is recorded in the scaler, and N (12 in this experiment) is the number of beam pulses within the ADC gate.

After the ADCs covert pulses into a digital format, the information is transferred to the computer, which will format the information and save it on a hard disk. The

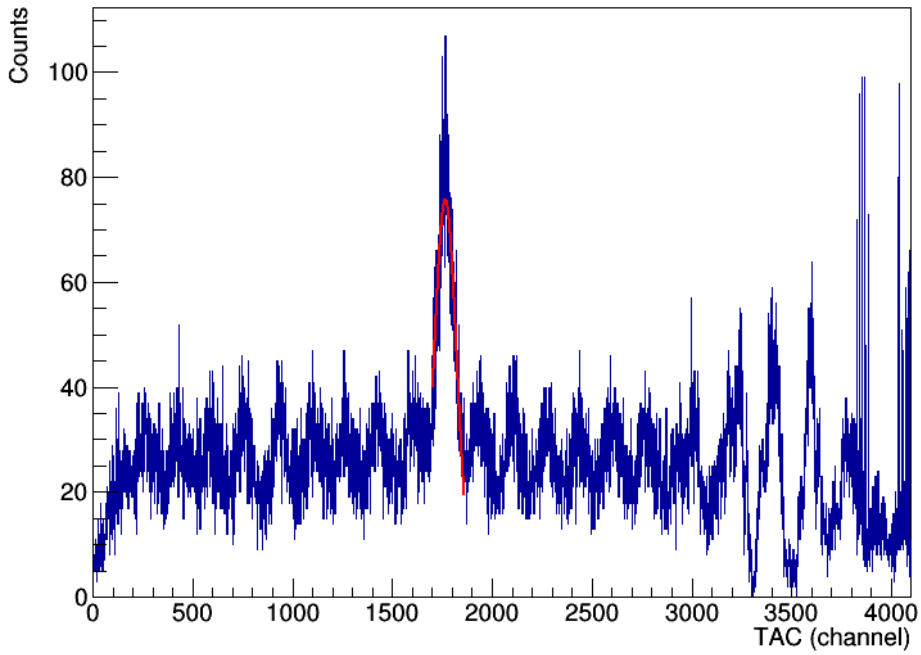

Figure 3.14: Spectrum produced from the time to amplitude convector (TAC), which measures the timing between events in the Si array and the IC. Small peaks are uncoincident detections and the large peak at Channel ∼1750 is the coincidence between detections in the Si array and IC. This spectrum is produced from the ^{2}H(^{20}Ne,p)^{21}Ne data set with the gas target using a 107-MeV ^{20}Ne beam and only a preliminary proton RF timing cut is enforced to help resolve the TAC spectrum. The mean IC counting rate is ∼600 kHz.

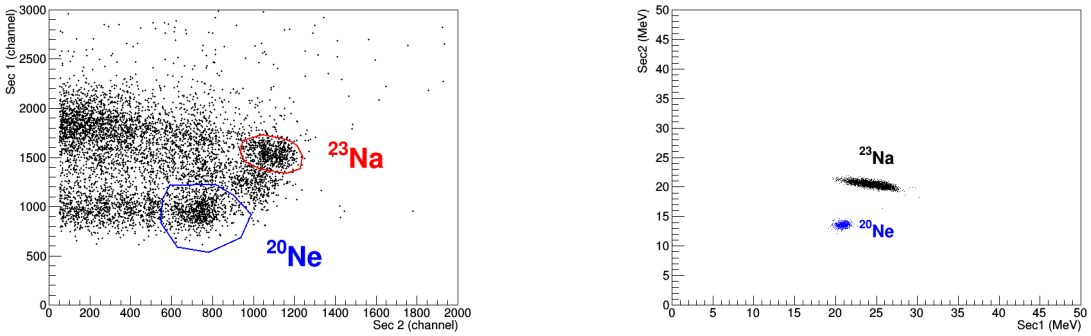

(a) (b)

Figure 3.15: (a) A spectrum of the energy loss in the first section of the IC (Sec 1) as a function of the energy loss in the second IC section (Sec 2) from the ^{4}He(^{20}Ne,p)^{23}Na data set with a 107-MeV ^{20}Ne beam, vs. (b) the simulation results. The data set is gated on the RF vs TAC spectrum and ΔE3 <300. The ^{20}Ne and ^{23}Na particle groups are marked.

time for this processing is ∼1 ms and during this time, the system will send a "veto" signal to block incoming events and any detections during this time will be lost. This time duration is called "Dead Time". To compensate for this loss of data, a scaler was used to record both the number of events detected and the number of events actually collected by the DAQ. The ratio between the two numbers is used to correct for this efficiency loss.

The wire interception efficiency loss occurs when a particle is intercepted by one of the wires of the IC before it is completely stopped by the gas. This phenomenon causes two subtypes of efficiency loss depending on the specific analysis method. If the particle is intercepted by the wires before the triggering section of the IC, a TAC signal from this event will not be produced and thus this event will not be included in the TAC cut. If the particle is intercepted by the wires after the triggering section, this event will have a correct TAC signal, but its position in the particle ID spectrum will be in one of the "interception" groups at lower channels, not in the main particle group (described in Sec. 2.4). This will result in the events not being included in the particle ID cut and will cause a loss of efficiency. The efficiency loss can be calculated using the number of grids in each section used in the IC. In the first scenario, the number of grids in front of the triggering section is recorded for efficiency loss, otherwise the number of grids before the stopping position of the particle group is recorded. After obtaining this number, given by N, the efficiency can be calculated by the following formula,

$$\varepsilon_{\text{NotStopped}} = (1 - p_{\text{stop}})^N, \tag{3.10}$$

where p_{stop} is the probability of particles stopping on one grid wire, which can be calculated from the experimental data by "Interception Island Counts"/total number of entries. In this experiment, p_{stop}=0.6%.

The angular coverage comes from two aspects, the first of which is the angular coverage of the HELIOS Si array with a solid target. This coverage can be directly calculated through two body kinematics calculations or simulated through the Geant4 simulation. The Geant4 simulation studied the effects due to a misalignment between the Si array and the solid target, by moving the reaction point away from the center in 1 mm steps up to 3 mm in each direction. The statistics for each detector segment can vary up to 40%, but the sum of the four sides is constrained within a 5% uncertainty. Thus, in the following analysis, it is always assumed that good alignment exists between the array and the target. The second component of the angular coverage is from the emmitance of the gas target. As mentioned previously, the emmittance of the gas target is different depending on the emitting angles and the reaction positions. The overall efficiency is also studied through the Geant4 simulations discussed above. In this simulation the beam location is moved in 1 mm steps up to 2 mm from the target's center and the geometrical efficiency for each state and detector segment is recorded (see below for results).

(α,p) Reaction Normalization

The general relation between the cross section and the detector counts, ΔN, is given by,

$$\Delta N = \varepsilon \Delta\Omega \frac{\mathrm{d}\sigma}{\mathrm{d}\Omega} I_{beam} \Delta t n l \tag{3.11}$$

$$= \varepsilon \Delta\Omega I_{beam} \frac{\mathrm{d}\sigma}{\mathrm{d}\Omega} \Delta t \frac{m\rho l}{M} \mathrm{N_A}, \tag{3.12}$$

where ε is the overall efficiency, Δt is the time of the run, I_{beam} is the beam rate, n the target particle density, l is the target thickness, $\mathrm{N_A}$ is Avogadro's constant, M is the molar mass of helium gas and m the number of target atoms in a molecule (helium gas is monatomic gas and $m = 1$). Typically, the beam rate on the target is measured directly through a Faraday cup or indirectly using Rutherford scattering off a gold foil. However, these methods are not applicable when using the gas target in HELIOS.

As the window thickness on each side of the gas target is $\sim$1 mg/cm^2, approximately an order of magnitude thicker than a typical solid target ($\sim$100 $\mu g/cm^2$), the windows result in a large amount of contamination from scattering and fusion reactions, and much of this heavy ion (beam) scattering contamination will enter the IC. As the IC can not handle counting-rates of more than $\sim$800 kHz, the IC rate tolerance limits the intensity of the beam current we can apply on the gas target. This limit is well below the amount of current that a Faraday cup can detect. Thus a direct beam current measurement was not possible.

An indirect Rutherford scattering measurement using gold foil is also not feasible as the strong magnetic field of HELIOS will distort the trajectories of the scattered beam. Depending on the charge states populated in the scattered beam, the distortion of the trajectories will differ and, as a result, the position distribution of the scattered beam can not be calculated using the Rutherford scattering function.

Thus, an alternative normalization method is adopted. The method starts with transforming Eq. 3.11 using the ideal gas law formula $PV = NRT$,

$$\Delta N = \Delta\Omega I_{beam} \frac{\mathrm{d}\sigma}{\mathrm{d}\Omega} \Delta t \frac{m\rho l}{M} \mathrm{N_A} \tag{3.13}$$

$$= \Delta\Omega I_{beam} \frac{\mathrm{d}\sigma}{\mathrm{d}\Omega} \Delta t \frac{mP}{RT} l \mathrm{N_A}. \tag{3.14}$$

A similar equation can be obtained for (d,p) reactions with the gas target.

As the pressure and temperature were set the same for both (α,p) and (d,p) reactions, by dividing Eq. 3.14 for (d,p) and (α,p) reactions, temperature, pressure, target thickness and all constants cancel out,

$$\frac{\Delta N_{(\alpha,p)}}{\Delta N_{(d,p)}} = \frac{I_{(\alpha,p)} \Delta t_{(\alpha,p)}}{I_{(d,p)} \Delta t_{(d,p)}} \frac{m_{(\alpha,p)}}{m_{(d,p)}} \frac{\frac{\mathrm{d}\sigma_{(\alpha,p)}}{\mathrm{d}\Omega}(\theta_1) \Delta\Omega_{(\alpha,p)}}{\frac{\mathrm{d}\sigma_{(d,p)}}{\mathrm{d}\Omega}(\theta_2) \Delta\Omega_{(d,p)}}. \tag{3.15}$$

The ratio between the integrated beam on target for each gas used is proportional

to the ratio of protons detected from fusion evaporation reactions between the beam and the gas target windows in each case ($\frac{\text{Fusion}_{(\alpha,p)}}{\text{Fusion}_{(d,p)}} = \frac{I_{(\alpha,p)}\Delta t_{(\alpha,p)}}{I_{(d,p)}\Delta t_{(d,p)}}$, where Fusion_x is the number of protons detected from fusion evaporation), which can be selected by gating on proton RF timing. Thus, the equation is further simplified to,

$$\frac{\Delta N_{(\alpha,p)}}{\Delta N_{(d,p)}} = \frac{1}{2}\frac{\text{Fusion}_{(\alpha,p)}}{\text{Fusion}_{(d,p)}}\frac{\frac{\mathrm{d}\sigma_{(\alpha,p)}}{\mathrm{d}\Omega}(\theta_{(\alpha,p)})\Delta\Omega_{(\alpha,p)}}{\frac{\mathrm{d}\sigma_{(d,p)}}{\mathrm{d}\Omega}(\theta_{(d,p)})\Delta\Omega_{(d,p)}}. \tag{3.16}$$

Then the (α,p) reaction cross section can be calculated as,

$$\frac{\mathrm{d}\sigma_{(\alpha,p)}}{\mathrm{d}\Omega}(\theta_{(\alpha,p)}) = 2\frac{\text{Fusion}_{(d,p)}}{\text{Fusion}_{(\alpha,p)}}[\frac{\Delta N_{(\alpha,p)}}{\Delta\Omega_{(\alpha,p)}/(4\pi)}/\frac{\Delta N_{(d,p)}}{\Delta\Omega_{(d,p)}/(4\pi)}]\frac{\mathrm{d}\sigma_{(d,p)}}{\mathrm{d}\Omega}(\theta_{(d,p)}) \tag{3.17}$$

$$= 2\frac{\text{Fusion}_{(d,p)}}{\text{Fusion}_{(\alpha,p)}}\frac{\Delta N_{(\alpha,p)}/\eta_{(\alpha,p)}}{\Delta N_{(d,p)}/\eta_{(d,p)}}\frac{\mathrm{d}\sigma_{(d,p)}}{\mathrm{d}\Omega}(\theta_{(d,p)}) \tag{3.18}$$

$$= 2\frac{\text{Fusion}_{(d,p)}}{\text{Fusion}_{(\alpha,p)}}\frac{\frac{\Delta N_{(\alpha,p)}}{\eta_{(\alpha,p)}}}{\frac{\Delta N_{(d,p)}}{\eta_{(d,p)}}/\frac{\mathrm{d}\sigma_{(d,p)}}{\mathrm{d}\Omega}(\theta_{(d,p)})}, \tag{3.19}$$

where η is the solid angle coverage efficiency and it is equal to $\Delta\Omega/(4\pi)$.

According to the above equation, by performing the measurements for both the (d,p) and (α,p) reactions using the gas target, the differential cross section for ^{4}He(^{20}Ne,p)^{23}Na can be normalized to the (d,p) reaction cross section. As the ^{2}H(^{20}Ne,p)^{21}Ne reaction has been measured previously and the cross section can be obtained through a DWBA calculation, our measurements of the (α,p) reaction can be well constrained.

For the second experimental setup, the gas target uses Ti foils for the windows and this forbids the use of deuterium gas (discussed in Sec. 2.3). Therefore the normalization reaction [^{2}H(^{20}Ne,p)^{21}Ne] used in first experimental setup can not be used here. As the Si array is now placed in the downstream position, the detection of α scattering and negative Q-value reactions is possible for this geometry. The ^{4}He(^{20}Ne,^{4}He)^{20}Ne reaction is the perfect reaction for normalization, and this reaction happens concurrently with (α,p). As a result, the ratio of integrated beam on target will be 1 and Eq. 3.15 becomes

$$\frac{\mathrm{d}\sigma_{(\alpha,p)}}{\mathrm{d}\Omega}(\theta_{(\alpha,p)}) = \frac{\Delta N_{(\alpha,p)}/\eta_{(\alpha,p)}}{\Delta N_{(\alpha,\alpha)}/\eta_{(\alpha,\alpha)}}\frac{\mathrm{d}\sigma_{(\alpha,\alpha)}}{\mathrm{d}\Omega}(\theta_{(\alpha,\alpha)}). \tag{3.20}$$

In summary, when the first experimental setup is used, separate measurements with ^{2}H(^{20}Ne,p)^{21}Ne gas target are needed for normalizing the ^{4}He(^{20}Ne,p)^{23}Na reaction cross sections. While for the second setup, the measurements will be normalized to ^{4}He(^{20}Ne,^{4}He)^{20}Ne scattering, which happens at the same time as the (α,p) reactions. Below, the details of the experimental data and the analysis at each beam energy will be discussed in depth.

3.4.2 The ^{2}H(^{20}Ne,p)^{21}Ne reaction with solid targets with 107-MeV ^{20}Ne

The ^{2}H(^{20}Ne,p)^{21}Ne measurements were taken with a 107-MeV ^{20}Ne beam energy and a 131-μg/cm^2 solid CD_2 target. The results are used to examine the experimental setup and to validate our DWBA calculation, thus only the two most populated states are evaluated (the 0.35 MeV and 2.80 MeV states). Cross sections for the ^{2}H(^{20}Ne,p)^{21}Ne reaction are large ($\sim$10 mb) compared to (α,p) reactions and, unlike gas target measurements that are heavily contaminated by scattering and fusion reactions, this setup allows for higher incident beam current (600 epA in this measurement). Proton lines are visible only after a rough timing cut of TAC>100 (Fig. 3.16). Nevertheless, it is important to mention that the "knees" of the proton lines, which are located to the bottom left of Fig. 3.16, are cut off when using this TAC gate. These protons coincide with the ^{21}Ne recoils with small opening angles, which are blocked from entering the IC and thus do not produce a TAC signal, while protons are still detected in the HELIOS Si array.

To analyze this data set, a narrow TAC gate alone is enough to eliminate most contamination (Fig. 3.17). To evaluate the statistics, it is necessary to align the proton lines along the energy axis. The energy vs. position spectrum can be aligned according to the fitting of any of the proton lines and the statistics can be obtained by projecting the aligned spectrum to the Y axis. The resulting histogram is divided into reaction and background zones, where a background subtraction is performed (Fig. 3.18) and the data are presented in Table 3.2.

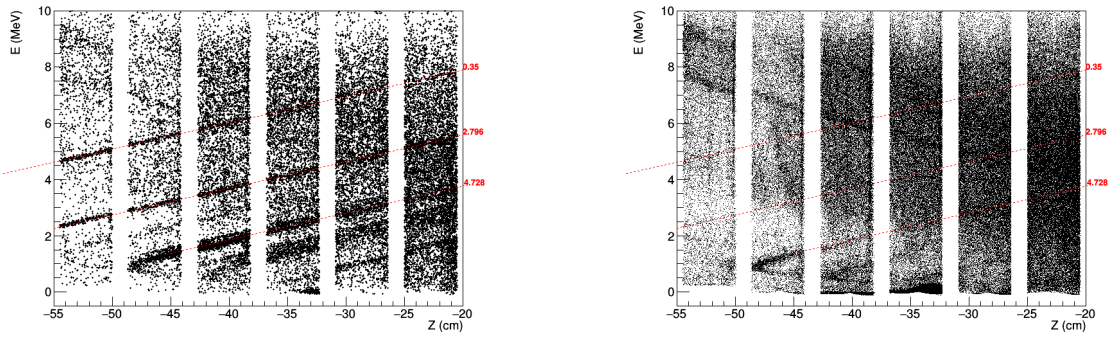

(a) (b)

Figure 3.16: Spectrum of proton energy as a function of axial distance from the center of HELIOS as detected in the HELIOS Si array with (a) TAC>100 and (b) TAC<100. Dashed red lines are simulated proton lines from excited states of ^{21}Na at 0.35, 2.796 and 4.728 MeV.

As only one TAC cut is applied in this data-set, two efficiency corrections need to be applied to calculate the cross sections: the dead time correction, which can be calculated by "Live Triggers"/"All Triggers"$\approx$0.82%, and the wire interception efficiency factor (as no PID spectrum cut is used, only the 12 grids before the triggering IC section are needed for this calculation) is calculated to be 93%.

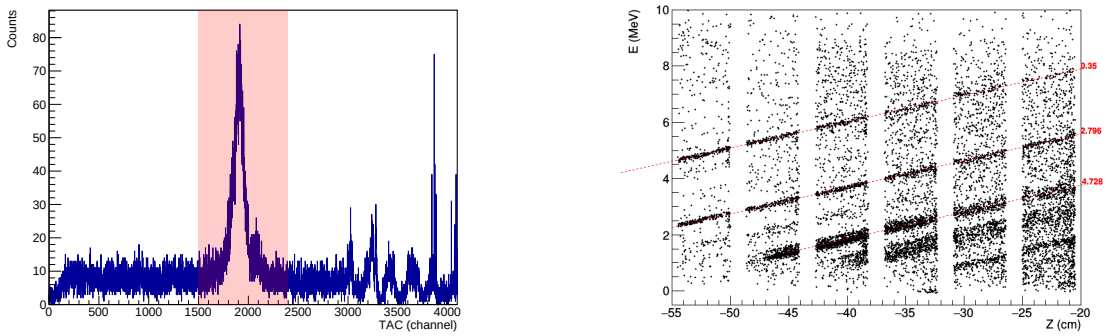

(a) (b)

Figure 3.17: (a) TAC spectrum and (b) energy vs. position spectrum after the TAC cut, which is shown in pink in (a) for the ^{2}H(^{20}Ne,p)^{21}Ne reaction at 107 MeV with a solid CD_2 target.

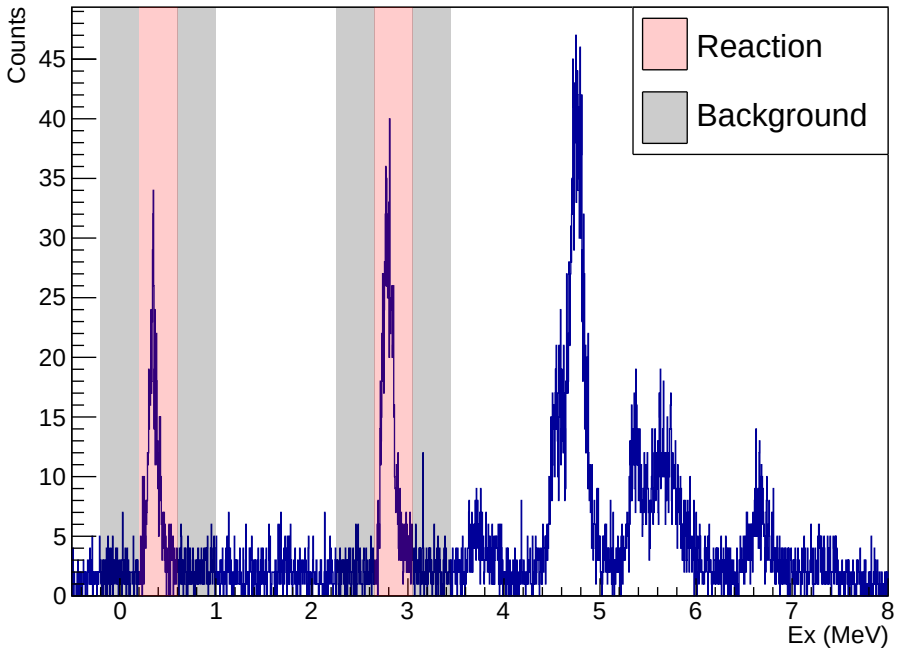

Figure 3.18: Excitation energy spectrum from the ^{2}He(^{20}Ne,p)^{21}Ne reaction taken with a 107-MeV ^{20}Ne beam and a solid CD_2 target. Statistics in highlighted regions are used for the cross section calculations (red) and background subtractions (grey). Only cross sections for 0.35 and 2.80 MeV states are calculated.

	0.35 MeV		2.80 MeV	
Region (cm)	CMS Angle	Final Counts	CMS Angle	Final Counts
[-54.5, -50.0]	33.1°	188±14	22.5°	172±14
[-48.7, -44.1]	36.6°	152±13	27.9°	175±14
[-42.7, -38.2]	40.0°	126±13	32.6°	193±15
[-36.8, -32.3]	43.0°	90±12	36.4°	181±15
[-30.9, -26.4]	45.9°	51±10	40.1°	132±14
[-25.0, -20.5]	48.8°	23±9	43.7°	134±14

Table 3.2: A summary of counts for the ^{2}He(^{20}Ne,p)^{21}Ne measurements with 107 MeV beam energy and solid CD_2 target. Regions shown are the position coverage in cm of each detector segment. Only statistical uncertainties are given

Geometric efficiencies for each segment of the Si array are obtained using Geant4 simulations and the results are listed in Table 3.3.

State	1 (%)	2 (%)	3 (%)	4 (%)	5 (%)	6 (%)
0.35 MeV	0.83	0.80	0.80	0.72	0.80	0.87
2.80 MeV	0.88	0.89	0.92	0.83	0.81	0.98

Table 3.3: Simulated solid angular coverage (in percentage of 4π) for each segment (summed for all 4 sides) of the HELIOS Si array for ^{2}He(^{20}Ne,p)^{21}Ne reactions with a solid target and 107-MeV beam energy. The numbers in the first row are the segment number, counting from the upstream position.

With all efficiency corrections applied, the cross sections can be calculated through the general cross section formula (Eq. 3.11), where the beam current was read out using a Faraday cup and is ∼600 epA. The calculated cross sections are compared to DWBA calculations and previously published results for both the 0.35-MeV and 2.8-MeV excited states of ^{21}Ne (Fig. 3.19). In this measurement, the equivalent deuteron beam energy is 10.8 MeV, which is close to the 11-MeV data presented in Datta et al. [84], but the measurements at 2.8-MeV excitation energy are not available in the paper. Thus, data from Heikkinen et al. [81] with a 12-MeV deuteron beam energy are used. Though the currently adopted value for the spectroscopic factor for the 0.35-MeV state is 0.62, our measured absolute cross sections better agree with the DWBA calculation with a spectroscopic factor of 1. This deviation could be due to uncertainties, including inaccurate target thickness.

3.4.3 107 MeV ^{2}H(^{20}Ne,p)^{21}Ne with the gas target

The same reaction is measured again using gas target filled with 500 Torr D_2 gas at room temperature. The energy vs. position spectrum before any data analysis is dominated by background, and the three strongest proton lines (0.35, 2.80 and

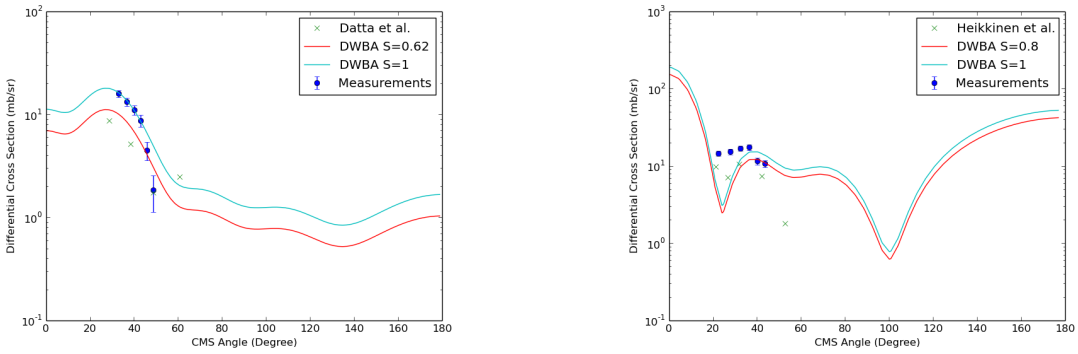

(a) (b)

Figure 3.19: Measured cross sections of ^{2}H(^{20}Ne,p)^{21}Ne with solid targets using a 107-MeV ^{20}Ne beam. The measurements are compared to other published results and DWBA calculations with spectroscopic factors of (a) 0.62 and 1 for the 0.35-MeV state and of (b) 0.8 and 1 for the 2.8-MeV state. The data published by Datta et al. was with an 11-MeV deuteron beam and the publications by Heikkinen used a 12-MeV deuteron beam.

4.73 MeV) are barely visible (Fig. 3.20). This spectrum can be effectively cleaned by gating on the most intensive group in the the timing spectrum (Fig. 3.21). The effectiveness of this cut is further confirmed by comparing the energy vs. position spectra after this cut and the anti-cut (with TAC>100) in Fig. 3.22.

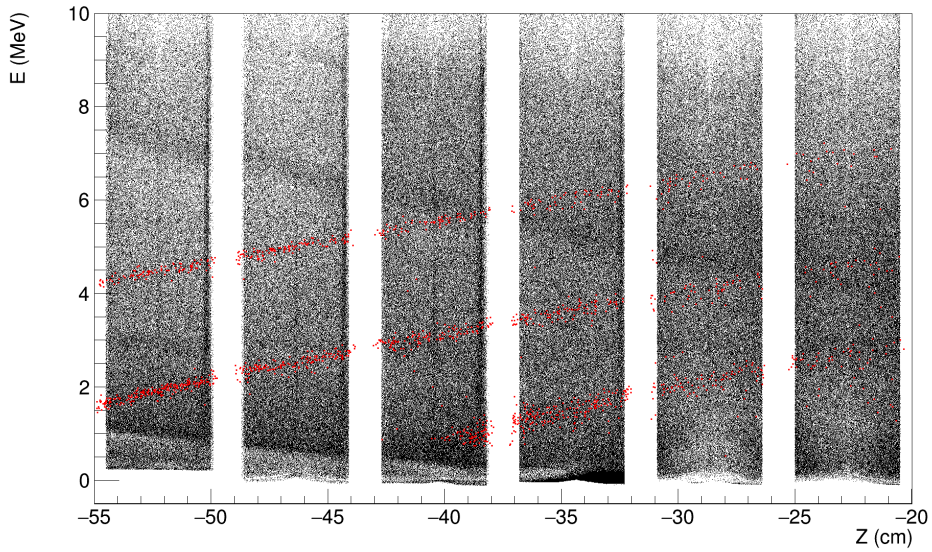

Figure 3.20: Energy vs. position spectrum before any cuts. Red markers are from simulations with ^{21}Ne in three excited states (0.35, 2.80 and 4.73 MeV).

After the timing cut, the structures in the spectrum of the energy losses of

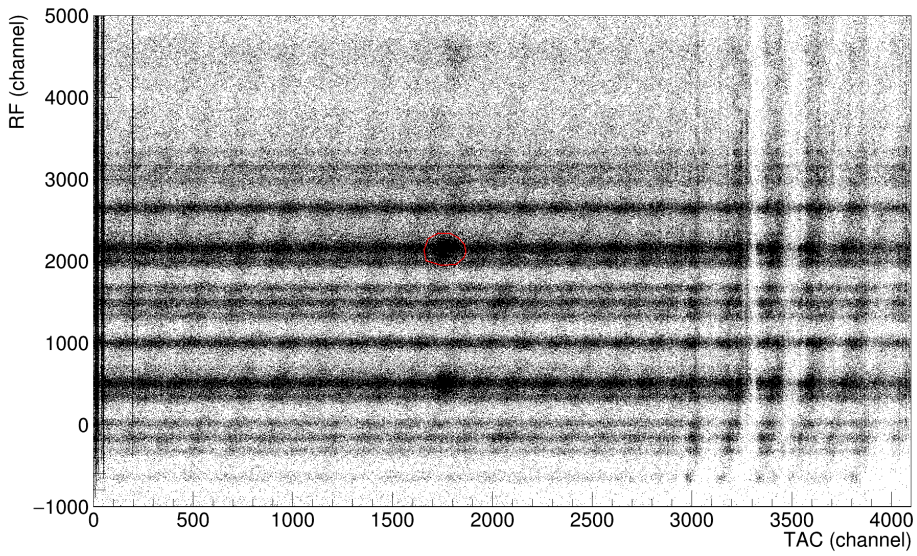

Figure 3.21: TAC vs. RF spectrum without any cuts. The red polygon shows the cut we applied to select the most intense group in this spectrum, which is associated with the ^{2}H(^{20}Ne,p)^{21}Ne reaction. The repeated pattern between the upper and lower half of the histogram is artificial (described in Sec. 3.3.3) and it is preferable to gate on the group close to the center of the histogram.

particles in Section 2 vs. Section 3 of the IC spectrum become much more clear. The ^{21}Ne particle group, which is marked with a red polygon in Fig. 3.23, can be identified by selecting intense proton lines in the energy vs. position spectrum (Fig. 3.22). By selecting this particle group, the energy vs. position spectrum is cleaned up and the proton lines perfectly match Geant4 simulations (Fig. 3.24). The statistics are summarized in Table 3.4.

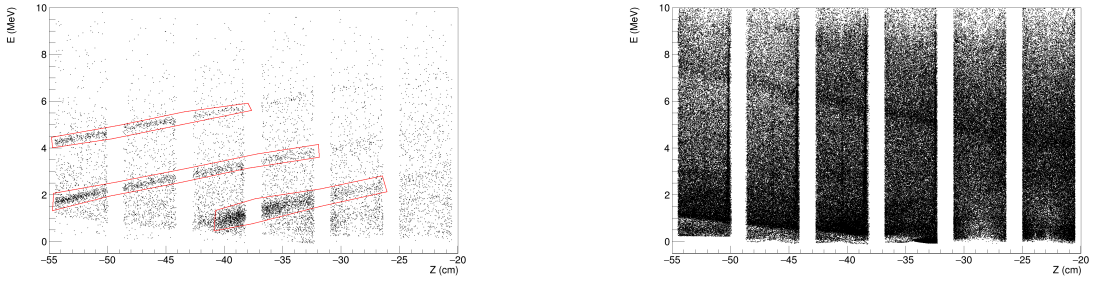

(a) (b)

Figure 3.22: (a) Energy vs. position spectrum after applying the cut in Fig. 3.21 and (b) energy vs. position spectrum with the anti-cut (i.e. everything outside the polygon shown in Fig. 3.21) and TAC>100. Red gates in (a) are applied in the next step to study the features of the IC spectrum.

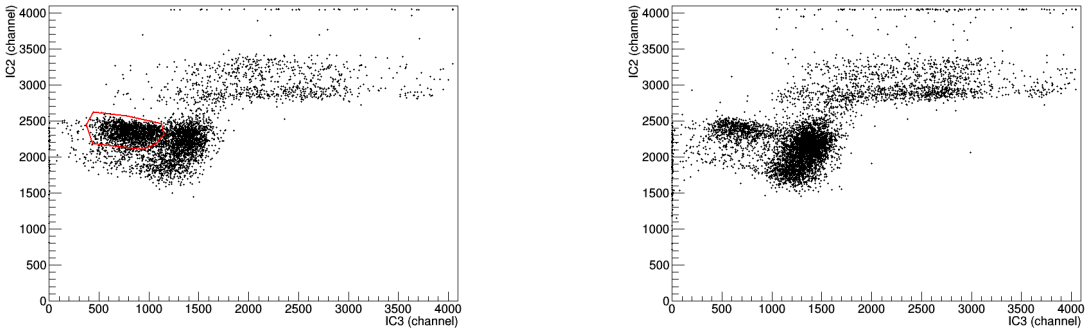

(a) (b)

Figure 3.23: (a) The spectrum of the energy losses of particles in Section 2 vs. Section 3 of the IC after the red cut on the TAC vs. RF spectrum (Fig. 3.21) and cuts on the energy vs. position spectrum (Fig. 3.22a); (b) the spectrum of the energy losses of particles in Section 2 vs. Section 3 after the red cut on TAC vs. RF spectrum and anti-cuts on energy vs. position spectrum. In (a), the position of ^{21}Ne particle group is marked in red.

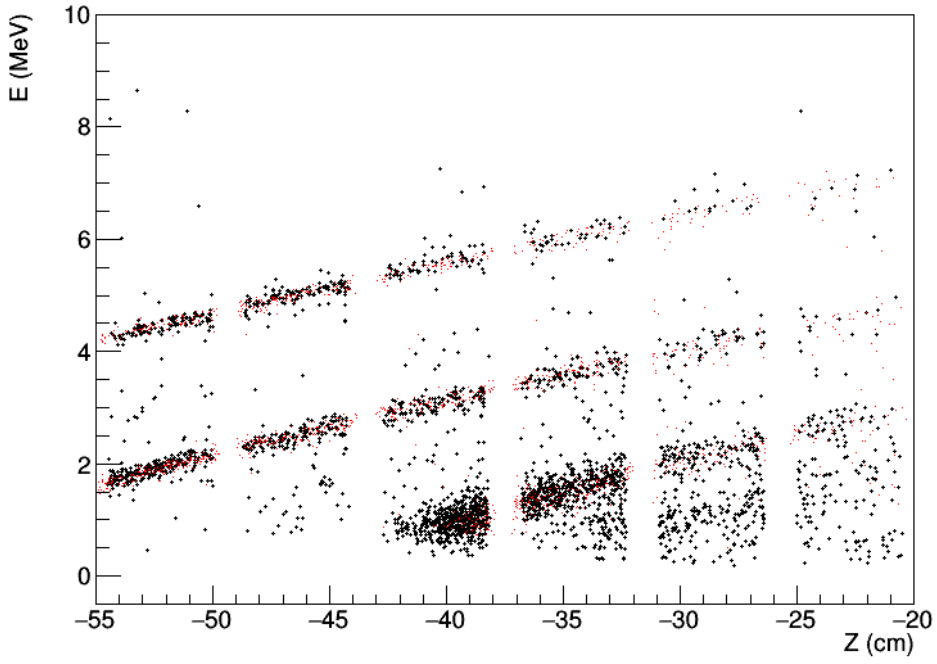

Figure 3.24: Energy vs. position spectrum after the TAC vs. RF spectrum cut (shown in Fig. 3.21) and the particle ID cut (shown in Fig. 3.23). Red markers are from simulations with ^{21}Ne in three excited states (0.35, 2.80 and 4.73 MeV).

Region (cm)	0.35 MeV Final Counts	2.80 MeV Final Counts
[-54.5, -50.0]	104±10	211±15
[-48.7, -44.1]	108±10	137±12
[-42.7, -38.2]	59±8	129±11
[-36.8, -32.3]	36±6	85±9
[-30.9, -26.4]	12±3	42±6
[-25.0, -20.5]	5±2	9±3

Table 3.4: A summary of counts for the ^{2}He(^{20}Ne,p)^{21}Ne measurements with a 107-MeV ^{20}Ne beam and the gas target. Only statistical uncertainties are shown.

Due to the "ADC pileup" efficiency loss described in Sec. 3.4.1, a significant portion of the ^{21}Ne particles are outside the particle ID gate (most are associated with the scattered beam and pileup groups) and this efficiency factor can be calculated using Eq. 3.8. The method of calculating the "ADC pileup" efficiency is discussed here. The number of ^{21}Ne before this "ADC pileup" can be obtained by counting the number of protons without a PID cut in Fig. 3.23. By comparing the resulting proton yield to the proton yield with the particle ID gate applied to the ^{21}Ne particle group (red polygon in Fig. 3.23), we can obtain the "ADC pileup" efficiency. This procedure is repeated for all individual runs for the (d,p) measurements with the gas target and 107-MeV ^{20}Ne beam energy. The results (Table 3.5) show good consistency between calculations using direct experimental data and Eq. 3.8. According to Eq. 3.8, the overall efficiency is 37±17% with average IC counting rate of 590.5±271.3 kHz for all 107-MeV (d,p) runs using the gas target.

Run#	IC Rates (kHz)	ε_1 (%)	ε_2 (%)	ε (%)
33	471.3±175.8	48±6	51±5	45±14
34	513.7±241.7	45±6	43±4	42±17
35	858.2±232.8	15±3	21±3	23±10

Table 3.5: Calculations of efficiencies using experimental data at 0.35 MeV (ε_1) and 2.80 MeV (ε_2) and using Eq. 3.8 (ε).

Additionally, the data also need to be corrected for the dead time efficiency ("Live Triggers"/"All Triggers"=70.40±0.03%), the wire interception efficiency (89.7%), and the solid angle coverage.

The solid angle coverage is obtained using Geant4 simulations, and a variety of beam positions were used for a series of simulations. The final solid angle coverage is the average of all the simulations and the standard deviations are evaluated. All of the statistics are presented in Table 3.6.

As mentioned in Sec. 3.4.1, the purpose of performing this ^{2}H(^{20}Ne,p)^{21}Ne measurement with the gas target is to normalize the (α,p) reaction products using the factor $\frac{\Delta N_{(d,p)}}{\eta_{(d,p)}} / \frac{d\sigma_{(d,p)}}{d\Omega}(\theta_{(d,p)})$. Currently, there is no published data for ^{2}H(^{20}Ne,p)^{21}Ne at a 10-MeV deuteron energy. Thus the cross sections are taken from DWBA cal-

0.35 MeV state						
Angle	32.5°	36.4°	39.8°	42.9°	46.3°	49.1°
ε(%)	0.76±0.04	0.71±0.04	0.50±0.04	0.39±0.02	0.35±0.03	0.28±0.07
2.80 MeV state						
Angle	17.4°	26.1°	31.3°	35.5°	40.3°	43.6°
ε(%)	1.17±0.07	1.05±0.08	0.77±0.13	0.57±0.09	0.47±0.05	0.35±0.03

Table 3.6: Simulated mean CMS angles and solid angle coverage in percentage of 4π for each segment of the HELIOS Si array for the ^{2}He(^{20}Ne,p)^{21}Ne reaction using a gas target and a 107-MeV ^{20}Ne beam.

culations with published spectroscopic factors (0.62 for 0.35 MeV and 0.8 for 2.8 MeV) and the cross sections are presented in Table 3.7 for angles corresponding to each segment of the Si array.

0.35 MeV state						
Angle	32.5°	36.4°	39.8°	42.9°	46.3°	49.1°
$\frac{d\sigma}{d\Omega}$(mb/sr)	10.1	8.8	7.2	5.7	4.3	3.1
2.80 MeV state						
Angle	17.4°	26.1°	31.3°	35.5°	40.3°	43.6°
$\frac{d\sigma}{d\Omega}$(mb/sr)	49.5	15.1	15.9	18.8	20.8	21.2

Table 3.7: Cross sections from DWBA calculations using Ptolemy.

The final value of $\frac{\Delta N_{(d,p)}}{\eta_{(d,p)}} / \frac{d\sigma}{d\Omega}(\theta_{(d,p)})_{(d,p)}$ is the average of the results calculated for each segment of the HELIOS Si array, weighted by the proton counts for each state. The final value to be used for the normalization of the ^{20}Ne(α,p) data is $\frac{\Delta N_{(d,p)}}{\eta_{(d,p)}} / \frac{d\sigma}{d\Omega}(\theta_{(d,p)})_{(d,p)}$= 4200±700 $(\frac{mb}{sr})^{-1}$.

3.4.4 107 MeV ^{4}He(^{20}Ne,p)^{23}Na

The initial spectra for the ^{4}He(^{20}Ne,p)^{23}Na reaction before any cuts are presented in Fig. 3.25 and Fig. 3.26, which show the position of the scattered ^{20}Ne particle group. Based on the initial particle ID spectra and the Geant4 simulations (Fig. 3.27), a set of preliminary cuts are attempted to reduce background, which include ΔE3<900, ΔE2>50, ΔE1>50, e(proton energy loss in Si)>0.5 MeV and TAC<900.

With the preliminary cuts on the particle ID spectra, the structure of the timing spectrum becomes clear. As proton RF timing is the same for protons from all reactions, it is expected that the known RF timing cuts deduced from the ^{2}H(^{20}Ne,^{1}H)^{21}Ne data set with the gas target can also be used for the (α,p) reaction data. Furthermore, Geant4 simulations show that the time difference for recoils traveling from the target to the IC between (α,p) and (d,p) reactions is ~10 ns, which is well less than the FWHM of the TAC peak (72 ns). In other words,

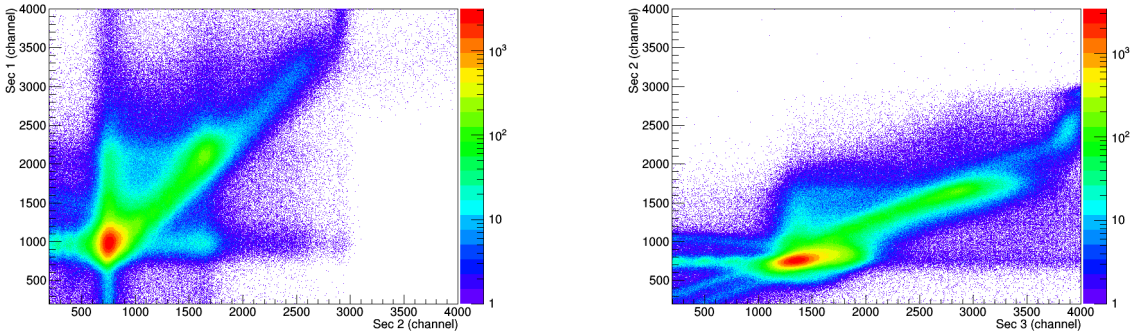

(a) (b)

Figure 3.25: The raw IC spectra of energy losses in (a) section 1 vs section 2 and (b) section 2 vs section 3 of the IC.

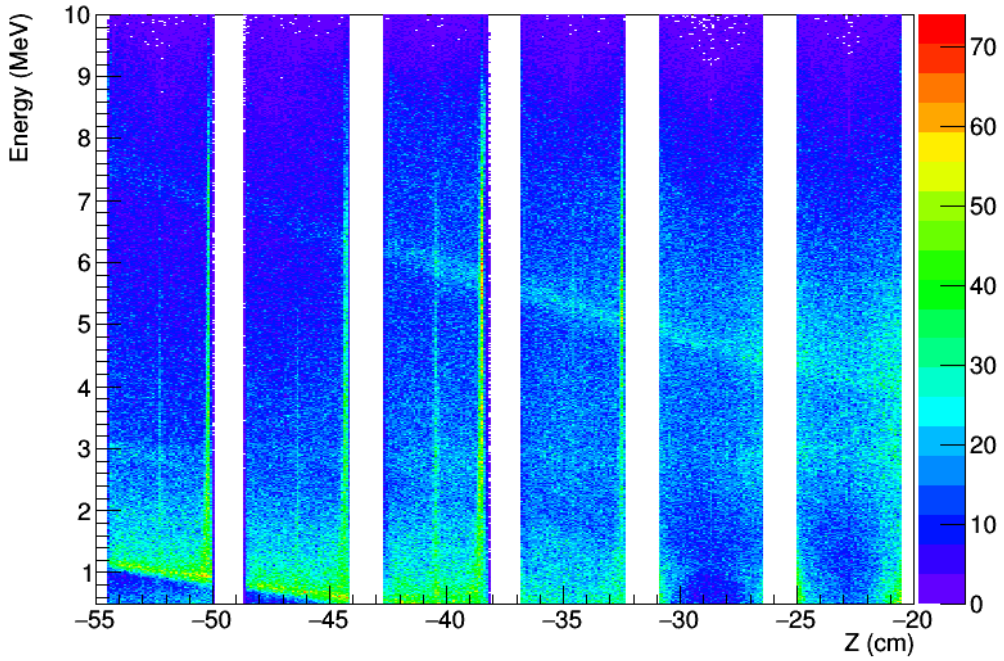

Figure 3.26: The raw spectrum of energy vs. position in the Si detector array for the ^{4}He(^{20}Ne,p)^{23}Na measurement with a 107-MeV ^{20}Ne beam.

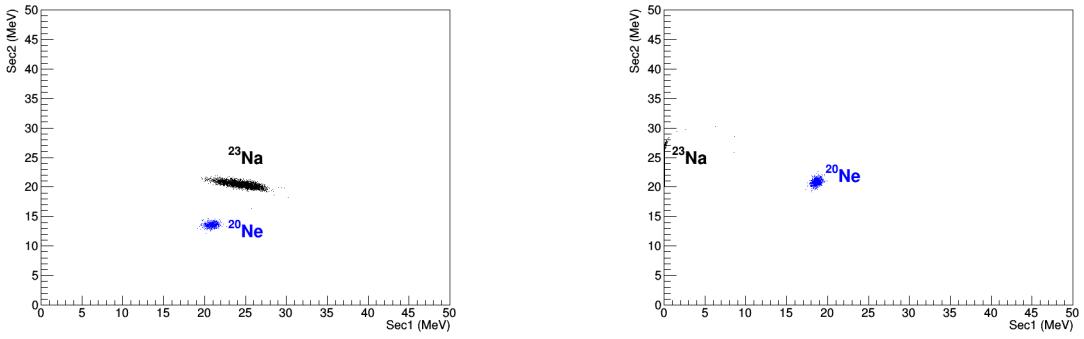

(a) (b)

Figure 3.27: Simulations of energy losses of ^{23}Na recoils from the ^{4}He(^{20}Ne,p)^{23}Na reaction in (a) section 1 vs section 2 and (b) section 2 vs section 3 of the IC.

locations of particle groups from (α,p) and (d,p) reactions are inseparable in the RF and TAC timing spectra. Thus, the same timing gate on the RF vs. TAC spectrum from the (d,p) reaction is applied to the (α,p) reaction data set (Fig. 3.21). Fine tuning of the cuts will be discussed later in this section.

After the backgrounds in the IC spectra are significantly reduced by the timing cut, a more stringent particle ID cut can be attempted. To study the features in the particle ID spectrum, the spectrum of energy loss in Section 1 vs. Section 2 of the IC is compared to the same spectrum after the anti-timing cut and also to the spectrum of the empty gas cell data set with same time cut. The comparison (Fig. 3.28) shows that one particular particle group exists only when ^{4}He gas fills the target. Furthermore, both this particle group and the simulated ^{23}Na particle group are located in a similar position relative to ^{20}Ne. The identification of the particle group is confirmed by a perfect match between the energy vs. position spectrum after the particle ID and timing cuts are applied, and the simulated energy vs. position spectrum (Fig. 3.28). The aligned 1D spectrum is presented in Fig. 3.29.

After the preliminary cuts needed to obtain a clean energy vs. position spectrum for the (α,p) reaction data are applied, the cuts can be further refined using the methods described below.

The first step in this procedure is to quantify the statistics. To obtain quantitative results, proton lines in the energy vs. position spectrum need to be aligned and projected to the Y axis. Typically, the alignment parameters are obtained by fitting a proton line from one specific state. Then the fitting results are applied back to the experimental data with following equation,

$$e_{\text{new}} = e_{\text{data}} - (a * z + b). \tag{3.21}$$

However, the statistics from the (α,p) reaction are so low that a reliable fit can not be obtained. Thus the fitting is performed using the simulated proton lines from different excited states. As the excitation energies of the states we are trying to study cover from 0 to 3.91 MeV, simulated data from the 2.08 MeV proton line are

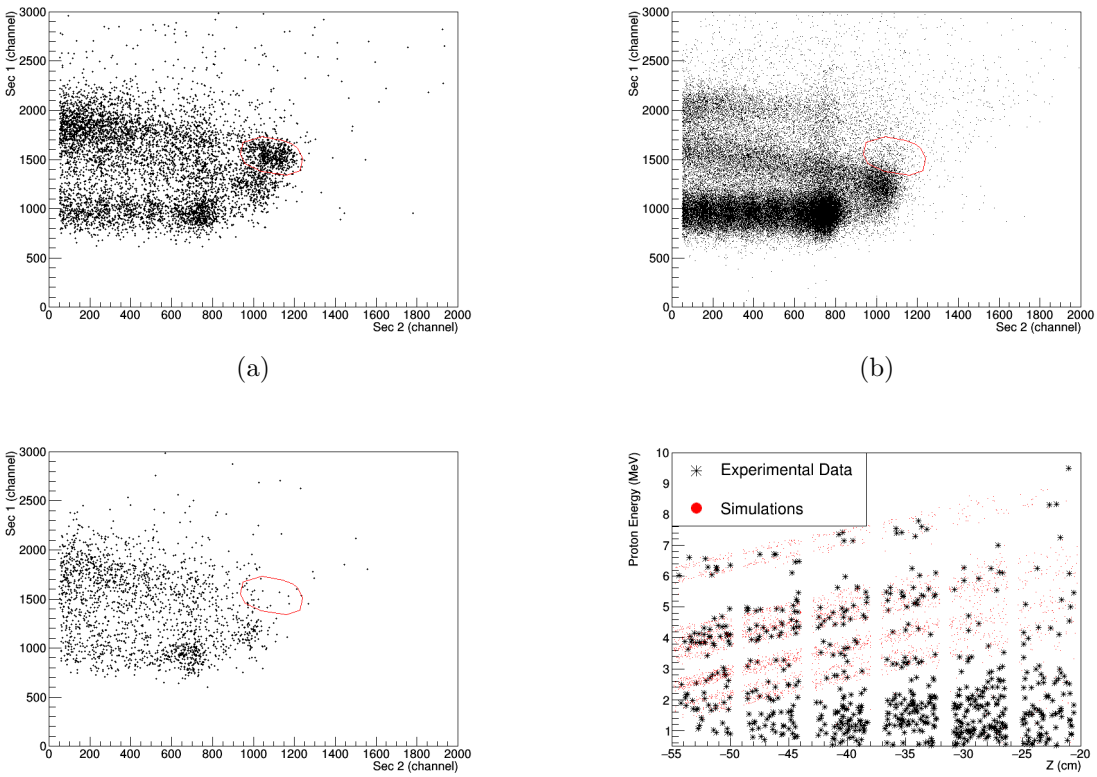

(a) (b)

(c) (d)

Figure 3.28: (a) A particle ID spectrum (section 1 vs section 2) with the timing cut and ΔE3<900 applied; (b) the same spectrum with anti-timing cut; (c) the particle ID spectrum with the empty gas cell data set after the same timing cut and ΔE3<900 are applied; (d) the comparison between measured energy vs. position spectrum (black stars) after gating on the particle group circled in red in (a), and the simulated spectrum (red dots).

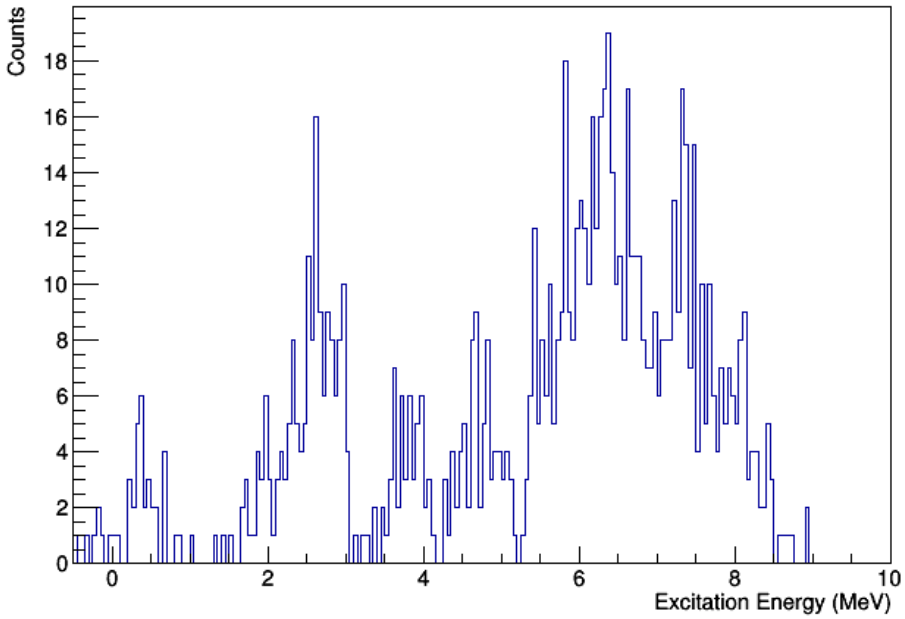

Figure 3.29: The yields of the excitation energy spectrum of ^{23}Na, with 107-MeV ^{20}Ne beam.

selected for the fit.

After the proton lines are aligned and projected, the number of data points below 4 MeV is recorded as the reaction yield. The same procedure is repeated for the empty gas cell data set. In order to determine the amount of background for the equivalent integrated beam on target when the gas target is filled, the yield from the empty gas cell data set is scaled according to the ratio of the fusion reaction counts between the reaction data set and the empty gas cell data set (described in Sec. 3.4.1 and the ratio for this measurement is equal to 2.984±0.005). The resulting number is the amount of background counts to be subtracted from the reaction data.

In order to determine the most appropriate cuts to apply to the data in various spectra, we gradually increase the gate area until the increase in reaction yield matches the increase in background yield. This idea is illustrated with the "Not IC3" cut (ΔE3 < ΔE3$_{\text{limit}}$). The "Not IC3" cut is used because ^{23}Na particles stop in section 2 and do not produce section 3 signals. First, a list of values for ΔE3$_{\text{limit}}$ at 100 Channel intervals starting at Channel 0 are created and the data are repeatedly sorted with each new ΔE3$_{\text{limit}}$ applied, while other cuts remain the same. The reaction yield and the amount of background are recorded using each ΔE3$_{\text{limit}}$ and are presented in Fig. 3.30. The figure shows that the ratio of the reaction yield to the amount of background starts around 750 at ΔE3$_{\text{limit}}$=0 and then dramatically drops to low values around 1. Therefore, ΔE3<100 is selected for the "Not IC3" cut. It is observed that the ratios between a ΔE3$_{\text{limit}}$ of 1100 and 1500 are slightly above 1, and this phenomenon is due to the "ADC pileup" effect described in Section 3.4.1. This is due to ^{23}Na being associated with the scattered

^{20}Ne group, despite not depositing energy in section 3. Therefore, by applying the "Not IC3" cut, some real ^{23}Na events are vetoed with and this needs to be accounted for using the "ADC pileup" correction.

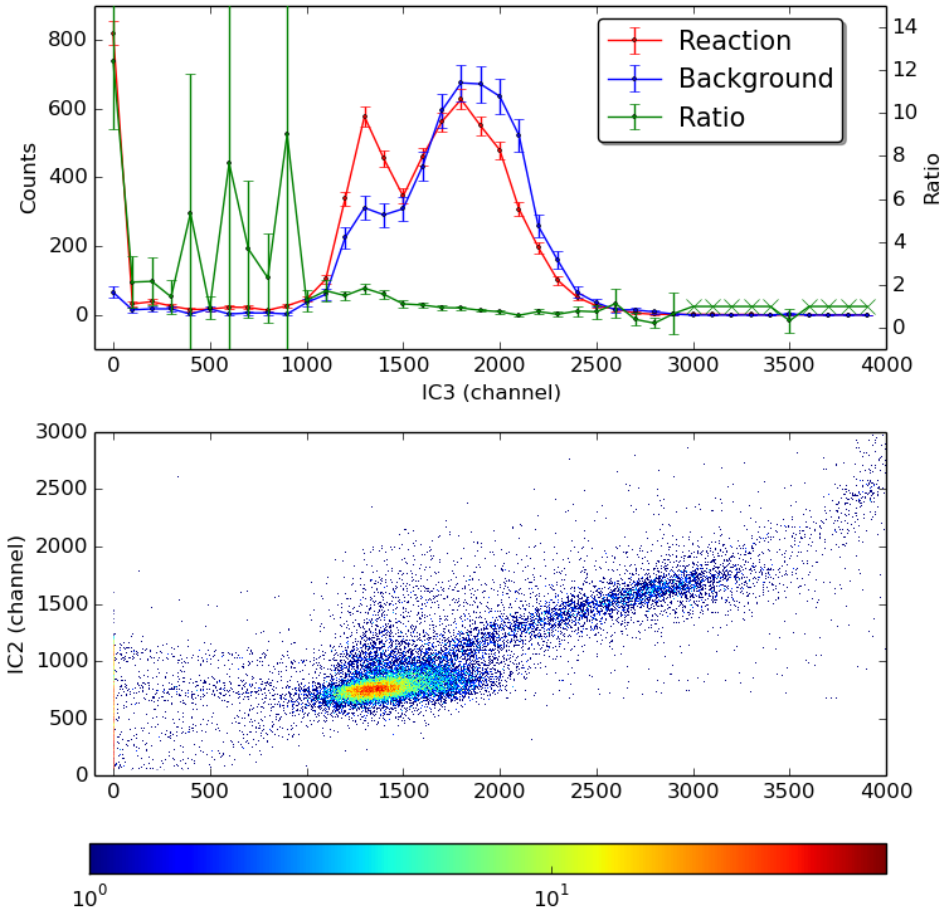

Figure 3.30: In the top figure, rates are calculated as counts/100 channels for the ^{4}He(^{20}Ne,p)^{23}Na reaction data set (red) and empty gas cell data set (blue). The ratio between reaction rates and background rates is presented in green. For the ratio, if background rates are 0, the values are set to 1 and the markers are given by an 'x'. The bottom figure is the ΔE2 vs ΔE3 histogram and the association between data density and color is presented in the colormap. The two figures share the x axis.

The same method is applied to cuts on the particle ID spectrum and the timing spectrum. In this scenario, cuts with slightly different sizes are attempted to evaluate the systematic uncertainties. The graphical cuts are plotted in the bottom halves of Fig. 3.36a and Fig. 3.36b and the statistics of the differences between each pair of neighboring cuts are presented in the top half. For example, the bars labeled A show the statistics of data points between cut A and cut B. These two figures show

that cut D in Fig. 3.36a and cut C in Fig. 3.36b are the most appropriate cuts to apply to the particle ID and TAC vs. RF spectra, respectively.

-

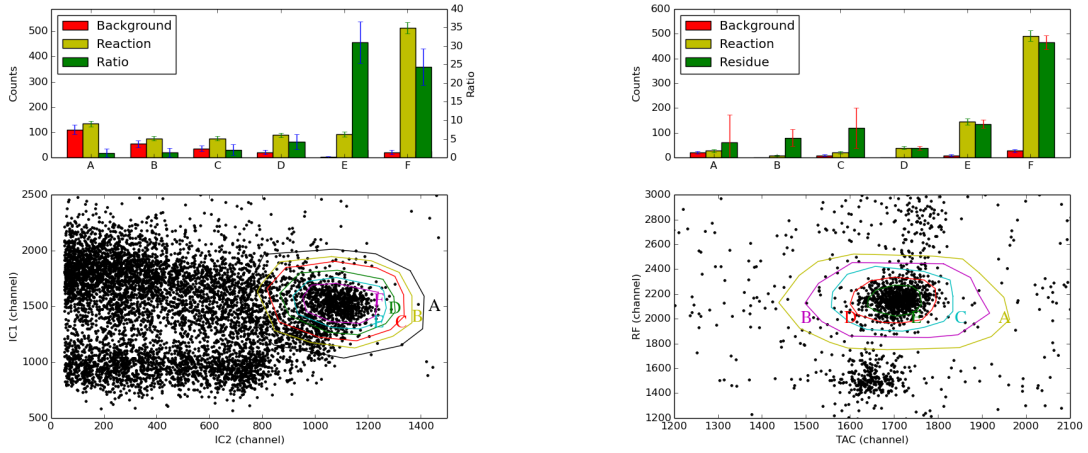

(a) (b)

Figure 3.31: (a) Results from fine-tuning the cut on the ΔE1 vs. ΔE2 PID spectrum, where multiple cuts are plotted on the bottom panel and the statistics are evaluated between each pair of cuts in the top panel (e.g. the statistics shown for D are the statistics for the differences between cuts C and D). (b) Similar fine-tuning analysis for the cut on the timing spectrum. Instead of the ratios between reaction yields and the amount of background, the differences (Residue) between the two numbers are plotted. The counts and the associated uncertainties of the bars labeled A, B and C are magnified by a factor of 10 for better visualization.

After optimizing all the applied cuts, statistics for all the proton lines corresponding to excited states populated via the ^{4}He(^{20}Ne,p)^{23}Na reaction can be evaluated. As statistics are very low, proton lines from states separated by less than 0.3 MeV in excitation energy are inseparable and the statistics are summarized for each group of excited states in Table 3.8. In this table, the "Final Counts" are calculated as "counts" - "Background Rate"$*$"Area", where the "Background Rate" is the counts per MeV in the energy spectrum from the empty gas cell data set and can be calculated simply as 2.948 (fusion reaction ratio) × counts/MeV at Ex<=5 MeV in the empty gas cell spectrum (e.g. 8 counts in the background spectrum below 5 MeV give counts/MeV equal to 8 counts *2.948/5 MeV = 4.7 counts/MeV).

The interception efficiency is 89.7% for the 18 grids before the stopping position of the particle group of ^{23}Na; the "ADC pileup" efficiency is 47±5% based on the average IC rate being 448±65 kHz; the dead time efficiency is 75.89±0.02%.

As the statistics for (α,p) reactions are very low, geometrical efficiencies for each group of states are presented across the whole range of the Si detector array, instead of for single detector segment. Thus, only one global solid angle coverage is provided for each state shown in Table 3.9.

States (MeV)	Region (MeV)	Counts	Final Counts
0,0.44	[-0.25, 0.69]	35	31±6
2.08,2.39,2.64,2.70,2.98	[1.83, 3.23]	146	139±12
3.68,3.85,3.91	[3.43, 4.16]	46	42±7
4.43,4.77	[4.18, 5.02]	68	64±8

Table 3.8: A summary of yields. Regions are where the reaction yields are evaluated. The "Counts" are proton numbers from the energy vs. position spectrum with refined cuts and "Final Counts" are the proton yields after background subtraction, where the background is evaluated from the empty gas cell data set. Uncertainties shown are statistical uncertainties only.

States (MeV)	Angular Range (CMS)	ε (%)
0	[38.5°,55.2°]	2.7±0.1
0.44	[37.4°,54.2°]	2.7±0.1
2.08	[31.0°,53.2°]	3.2±0.2
2.39	[30.1°,53.1°]	3.3±0.2
2.64,2.70	[25.1°,51.9°]	3.5±0.1
2.98	[26.3°,50.3°]	3.7±0.2
3.68	[14.4°,49.7°]	4.0±0.2
3.85,3.91	[19.6°,49.6°]	4.2±0.1
4.43	[15.6°,49.4°]	4.6±0.2
4.77	[3.7°,46.5°]	5.0±0.2

Table 3.9: A summary of geometric efficiencies for the ^{4}He(^{20}Ne,p)^{23}Na measurement with a 107-MeV beam energy and gas target.

Additionally, the fusion evaporation reaction ratio between the (d,p) and (α,p) reactions can be obtained using the method described in Sec. 3.4.1 and this ratio is equal to 4.728±0.006.

With all the above efficiencies and the results from section 3.4.3, the (α,p) cross section can be calculated using Eq. 3.17 and the results are listed in Table 3.10.

States (MeV)	Average Angle	Angular Range	$\frac{d\sigma}{d\Omega}$ (mb/sr)
0,0.44	40.1°	[26.2°,52.5°]	0.36±0.10
2.08,2.39,2.64,2.70,2.98	39.2°	[28.4°,52.8°]	1.35±0.27
3.68,3.85,3.91	36.0°	[23.5°,51.7°]	0.33±0.07
4.43,4.77	33.3°	[17.1°,49.3°]	0.42±0.10

Table 3.10: Final cross section results for the ^{4}He(^{20}Ne,p)^{23}Na measurements with a 107-MeV beam energy and gas target after all efficiency corrections.

3.4.5 88 MeV ^{4}He(^{20}Ne,p)^{23}Na

This measurement uses the same settings as the 107-MeV study, but the gas target was cooled to 93 K. The procedure for analyzing the 88-MeV data set is similar to the one used for the 107-MeV data set (including the analysis for the (d,p) data set with both gas targets and solid targets) and the explanation of these steps is not repeated here . As this measurement uses a lower beam energy, the proton lines are shifted to higher Z values and lower proton energies in the energy vs. position spectrum (Fig. 3.32), where proton lines are more difficult to separate and background is greater. Thus, statistics and cross sections of only two groups of states are presented in Fig. 3.34 and in Table 3.11. Additionally, the efficiencies used for the calculations are included in Table. 3.12. For completeness, this section also includes the comparison of PID spectra of reaction data and empty gas cell data (Fig. 3.33), and the analysis of the systematic uncertainties of the cuts used (Fig. 3.35).

Excitation Energies (MeV)	Average Angle	Angular Range	$\frac{d\sigma}{d\Omega}$(mb/sr)
0,0.44	42.0°	[29.6°,55.2°]	1.3±0.2
2.08,2.39,2.64,2.70,2.98	40.7°	[27.8°,53.4°]	1.7±0.3

Table 3.11: Resulting cross sections for the ^{4}He(^{20}Ne,p)^{23}Na measurement using an 88-MeV ^{20}Ne beam and the gas target after all efficiency corrections.

3.4.6 40 MeV ^{4}He(^{20}Ne,p)^{23}Na and ^{4}He(^{20}Ne,^{4}He)^{20}Ne Studies

In the final part of the experiment, the ^{4}He(^{20}Ne,p)^{23}Na reaction was measured using a 40-MeV ^{20}Ne beam, and the gas target was filled with 710 Torr ^{4}He gas at

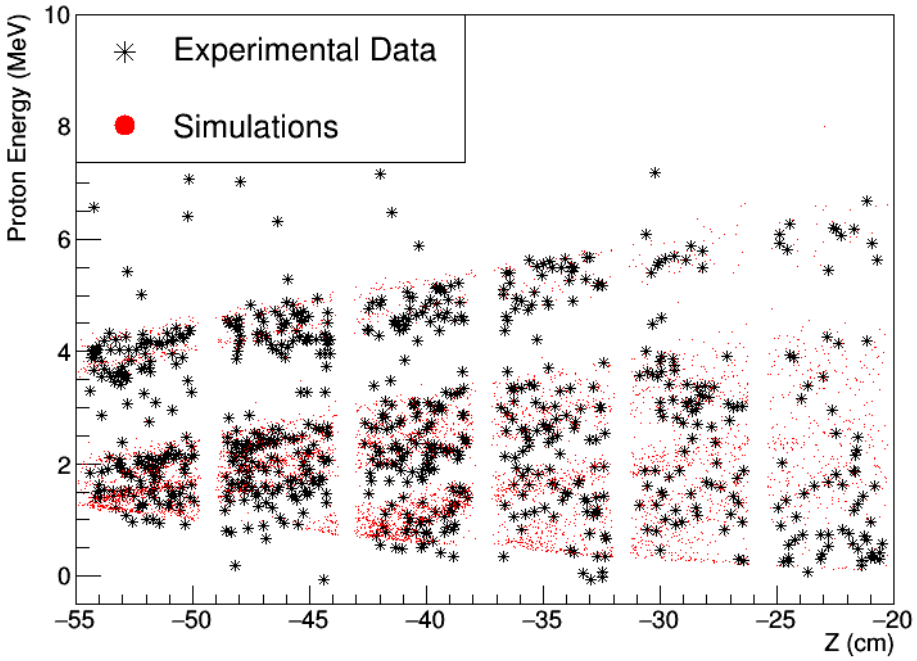

Figure 3.32: Energy vs. position spectrum after applying particle ID cuts and timing cuts. With the lower 88-MeV beam energy, the proton lines shift to lower energy and higher z in the spectrum, compared to the 107-MeV spectrum (Fig. 3.28d).

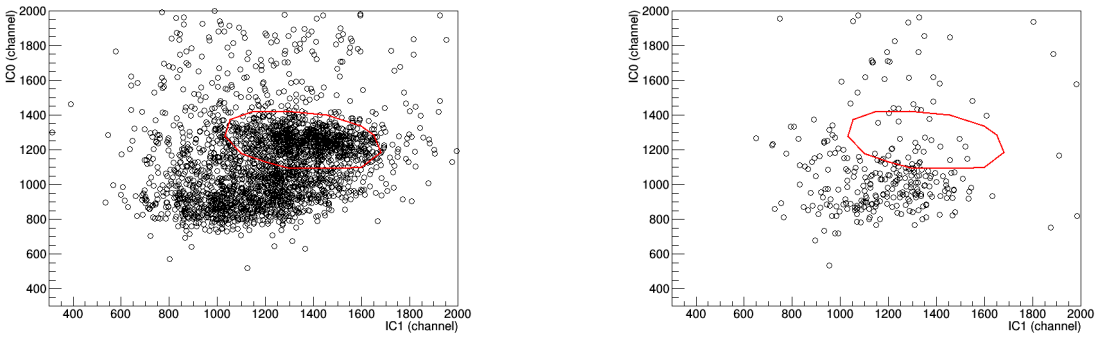

(a) (b)

Figure 3.33: (a) A particle ID spectrum (section 0 vs section 1) with the timing cut, ΔE2<500 and ΔE3<500 applied; (b) the same spectrum with an anti-timing cut applied.

DeadTime (%)	ADC Pileup (%)	Interception (%)
88.48±0.04	68±9	92±1

Table 3.12: Efficiencies obtained for the ^{4}He(^{20}Ne,p)^{23}Na measurement using an 88-MeV ^{20}Ne beam.

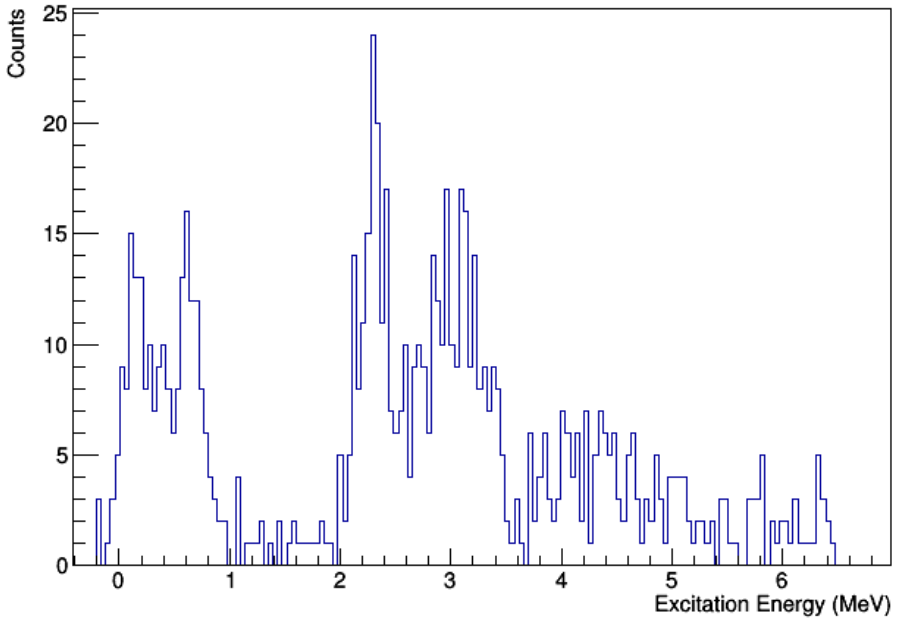

Figure 3.34: Yields of the excitation energy spectrum of ^{23}Na from the 88-MeV measurement.

room temperature. The gas target had an 88-μg/cm^2 gold foil placed upstream of the target and a 2.7 mg/cm^2 aluminum foil downstream of the target. Thus the beam energy inside the gas target was ∼31 MeV.

In this measurement, data from the ^{4}He(^{20}Ne,p)^{23}Na and ^{4}He(^{20}Ne,^{4}He)^{20}Ne reactions were collected simultaneously. As described in Chapter 2, the HELIOS Si array was positioned downstream of the gas target, and the IC was not installed. In this setup, the beam intensity was not limited by the counting ability of the IC, and significantly higher statistics are obtained for the (α,p) reaction. The main cut used to eliminate most background was applied to the RF spectrum. As mentioned previously, by gating on RF timing for protons and deuterons/alphas products from the (α,p) or (α,α) reactions, respectively can be selected (Fig. 3.37). The statistics for each reaction are summarized in Tables 3.13 and 3.14, where the background statistics are evaluated in the region next to the ground state where no strong states exists.

Unfortunately, one side of the Si array is shadowed by an aluminum frame, which was used to support the Faraday cup. Thus, only statistics from the other three sides (1, 2 and 4) are evaluated. Once again, the geometrical efficiencies are simulated with different beam positions. Because of the loss of one side of the array, the uncertainties of the simulated geometric efficiencies are larger. The simulated geometrical efficiencies for both the (α,p) reaction and (α,α) scattering are presented in Table 3.15.

As discussed in Sec. 3.4.1, the (α,p) measurements at 40 MeV are normalized to (α,α) scattering using Eq. 3.20. The (α,α) scattering cross sections are obtained

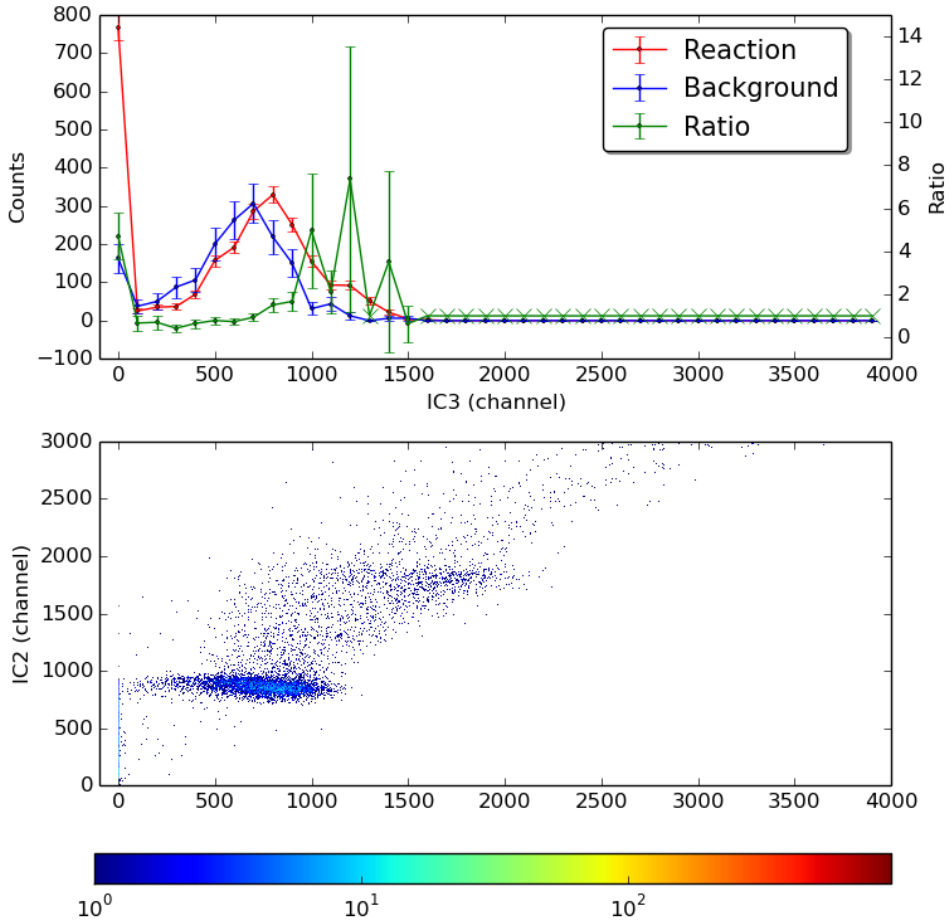

Figure 3.35: Top figure shows the rates calculated as counts/100 channels for the ^{4}He(^{20}Ne,p)^{23}Na reaction data set (red) and empty gas cell data using an 88-MeV ^{20}Ne beam (blue). The ratios between reaction rates and background rates are presented in green. For the ratio, if background rates are 0, the values are set to 1 and the markers are given by an 'x'. The bottom figure is the ΔE2 vs ΔE3 histogram and the association between data density and color is presented in the colormap. The two figures share the x axis.

Side	1	2	3	4	5	6
1	193±18	201±18	234±19	NA	NA	NA
2	315±22	307±22	302±21	229±19	255±20	221±18
3	84±10	NA	NA	NA	NA	NA
4	154±16	114±16	128±14	NA	NA	NA

Table 3.13: A summary of counts for ^{4}He(^{20}Ne,p)^{23}Na measurements with a 40-MeV beam energy and gas target for each side of the Si array. NA is given for a detector segment where proton lines can not be separated from background.

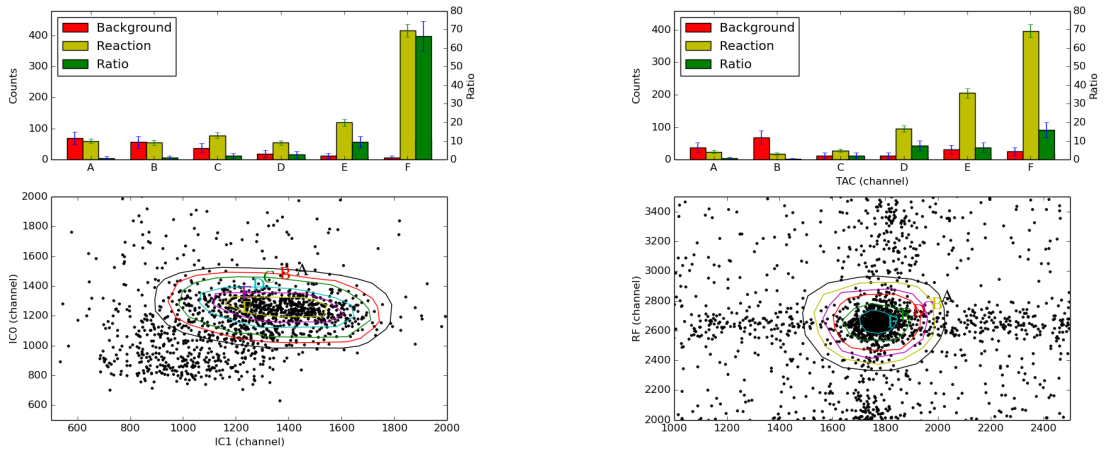

(a) (b)

Figure 3.36: Similar systematic study of cuts for the PID spectrum (ΔE0 vs. ΔE1) and RF vs. TAC timing spectrum for 88-MeV (α,p) data set, as shown in Fig. 3.31.

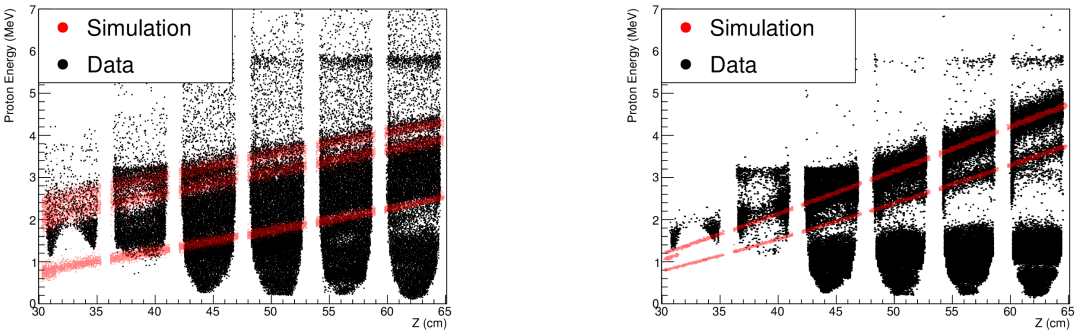

(a) (b)

Figure 3.37: (a) Proton energy vs. position spectrum from (α,p) reactions after gating on proton RF timing and (b) proton energy vs. position spectrum from (α,α) scattering after gating on deuteron/alphas RF timing. The red dots are simulated proton lines and the black dots are experimental data from the 40-MeV experimental run using setup 2.

Side	1	2	3	4	5	6
1	2766±53	3208±57	2954±54	2965±54	NA	NA
2	3580±60	3803±62	4205±65	NA	NA	NA
3	577±24	993±32	1511±39	3248±57	NA	NA
4	1666±41	1593±40	1414±38	NA	1899±44	NA

Table 3.14: A summary of counts for ^{4}He(^{20}Ne,^{4}He)^{20}Ne measurements with 40 MeV beam energy and gas target for each side of the Si array.

(α,α) scattering						
state (MeV)	1 (%)	2 (%)	3 (%)	4 (%)	5 (%)	6 (%)
0	0.75±0.09	0.68±0.09	0.62±0.08	0.55±0.07	0.47±0.06	0.51±0.07
1.633	0.83±0.11	0.73±0.09	0.66±0.08	0.59±0.07	0.51±0.07	0.19±0.03
(α,p) reaction						
state (MeV)	1 (%)	2 (%)	3 (%)	4 (%)	5 (%)	6 (%)
0	1.29±0.09	1.2±0.1	1.2±0.1	1.2±0.1	1.2±0.1	1.3±0.2
0.44	1.4±0.1	1.4±0.1	1.3±0.1	1.3±0.2	1.2±0.2	1.4±0.2

Table 3.15: Simulated geometrical efficiencies (given as percentage of 4π) of 3 sides of the HELIOS Si array for ^{4}He(^{20}Ne,^{4}He)^{20}Ne and ^{4}He(^{20}Ne,p)^{23}Na using the gas targets and a 40-MeV beam energy. The uncertainties are the standard deviation of simulated efficiencies for all beam position shifts (1 mm step for each direction and up to 2 mm distance from the center of the gas target.)

from Ref. [84], where a list of reaction energies and the associated cross sections of the ^{20}Ne(^{4}He,^{4}He)^{20}Ne reaction are presented. Cross sections from [84] are adopted if the energy points are within 2 sigma (1 sigma is 0.23 MeV) of the simulated mean energy of the reaction point in the gas cell. The average (±the standard deviation) of the selected cross sections are 48±21 mb at 80°.

After the above procedures are applied, the cross sections at three different angles for the (α,p) reaction studied with a 40-MeV ^{20}Ne beam are presented in Table 3.16. Though the proton lines from the ^{4}He(^{20}Ne,p$_1$)^{23}Na reaction are visible (p$_1$ refers to the reaction measurement populating ^{23}Na recoils in the first excited state), the statistics can not be extracted due to heavy background contamination (Fig. 3.37b).

Angle	Cross Sections (mb/sr)
105.0°	1.9±1.1
100.4°	1.8±1.1
95.9°	1.9±1.2

Table 3.16: Measured differential cross sections for ^{4}He(^{20}Ne,p)^{23}Na reactions at a 31-MeV ^{20}Ne beam energy, populating the ground state of ^{23}Na only. Because of higher statistics, cross sections are calculated at three angles.

For the final result, the cross sections from the 40-MeV ^{20}Ne beam measurements populating the ground state of ^{23}Na only are averaged into one cross section (1.9±0.7 mb/sr) and this number is compared to the published result from Vanhoy et al. [56] (Fig. 3.38), assuming an isotropic angular distribution for this reaction. The average cross section of the data from Vanhoy et al. folding in the energy distribution of the ^{20}Ne at reaction points is ∼1.6 mb/sr and is agreement with our value of 1.9±0.7 mb/sr.

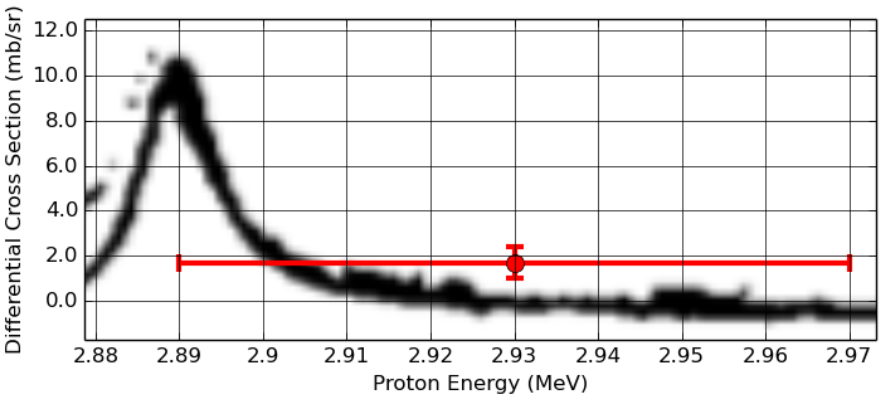

Figure 3.38: A comparison between the cross section measured in this experiment and published data of the inverse reaction by Vanhoy et al. [56]. The red marker represents the data point from this measurement and the scattered black dots are measurements by Vanhoy et al. Previously published data are fit using R-matrix code with the results shown by the thick black line (see [56] for more details).

Chapter 4
Conclusions and Future Work

The (α,p) and (p,α) reactions are important in astrophysics for their significant impact on energy output and on the final abundances produced in various astrophysical sites, such as classical novae, X-Ray Burst, and several types of Supernovae. Among all (α,p) reactions, the ^{20}Ne(α,p)^{23}Na reaction is a critical one in Type Ia Supernovae. We studied this reaction in inverse kinematics at Argonne National Laboratory using the HELIOS beam line. In the experiment a cryogenic gas target is used for producing (α,p) reactions, the HELIOS Si array is used to measure the energies and positions of protons and a fast position sensitive ionization chamber is used to detect the heavy recoils (^{23}Na). Three sets of measurements were performed using ^{20}Ne beam energies of 107, 88, and 40 MeV (100, 80 and 31 MeV at the reaction point), and the cross sections of this reaction populating the ground state of ^{23}Na are presented in Fig. 4.1 for all three beam energies, along with a TALYS cross section calculation [85], a statistical Hauser-Feshbach (HF) calculations of the cross sections. The measurements agree with the TALYS calculation, but the energy-cross section trend is atypical, as the cross section increases with lower reaction energies. We speculate that other reactions compete with the (α,p) reaction at higher beam energies, which results in a decrease in the cross sections of ^{20}Ne(α,p)^{23}Na reaction.

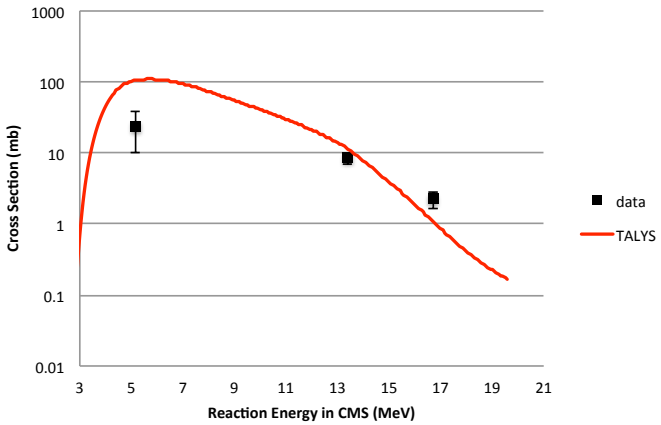

Figure 4.1: Total cross sections of the ^{4}He(^{20}Ne,p)^{23}Na reaction populating ^{23}Na in the ground state. The cross sections for beam energies of 107 and 88 MeV are obtained by multiplying the combined differential cross sections from ^{23}Na states at 0 and 0.44 MeV in Table 3.10 and Table 3.11 by 0.5. The measurements are compared to the TALYS cross section calculations.

Future work are listed here: examining uncertainties from the DWBA calculations by comparing several different models, such as FRESCO, DWUCK4 and PTOLEMY; determining contributions of excited states compared to the ground

state and comparing to HF calculations; determining reaction rates from the cross sections and using the rates in SNe simulations to study the effect of the ^{20}Ne(α,p)^{23}Na reaction on the nucleosynthesis process.

The ^{20}Ne(α,p)^{23}Na reaction cross section has been measured at three different beam energies directly. This direct measurement is the first direct measurement of this reaction approaching astrophysically relevant energies for Type Ia Supernovae. As it has been shown to be one of the most influential reactions for these astrophysical events, we plan to continue studies of this reaction at lower energies in the future, in addition to expanding this new technique for other direct (α,p) reaction measurements of astrophysical interest.

The measured cross section at the lowest energy point agrees with published data (shown in Fig. 3.38), and this is a proof-of-principle success of the experimental setup for (α,p) reaction measurements. The inability to obtain cross section measurements populating excited states of ^{23}Na at this energy shows the significance of the IC in providing reaction coincidences. For reactions such as ^{18}Ne(α,p)^{21}Na (a break out reaction from the hot CNO cycle) and ^{30}S(α,p)^{33}Cl (a reaction of interest for waiting points in Type I X-Ray Bursts), measurements within the astrophysical regime can be achieved using the 1st experimental setup with the IC and cross section information from excited states populated in the heavy recoils can be expected. An upgrade to the inflight facility is under development at Argonne National Laboratory. This set of devices will allow the production of radioactive ion beams with high purity, and a series of (α,p) reactions of astrophysical interest can be measured using this setup in the future.

Bibliography

[1] Bradley W Carroll and Dale A Ostlie. *An introduction to modern astrophysics and cosmology*, volume 1. 2006.

[2] Christian Iliadis. *Nuclear physics of stars*. John Wiley & Sons, 2015.

[3] Borexino Collaboration et al. Neutrinos from the primary proton-proton fusion process in the sun. *Nature*, 512(7515):383–386, 2014.

[4] http://faculty.tamuc.edu/cbertulani/ast/lectures/Lec10.pdf.

[5] James W Truran. Abundance evolution with cosmic time. *Reviews in Modern Astronomy: The Cosmic Circuit of Matter, Volume 16*, pages 261–274, 2003.

[6] T Rauscher, N Dauphas, I Dillmann, C Fröhlich, Zs Fülöp, and Gy Gyürky. Constraining the astrophysical origin of the p-nuclei through nuclear physics and meteoritic data. *Reports on Progress in Physics*, 76(6):066201, 2013.

[7] Bradley S Meyer. The r-, s-, and p-processes in nucleosynthesis. *Annual Review of Astronomy and Astrophysics*, 32:153–190, 1994.

[8] Jacob Lund Fisker, Friedrich-Karl Thielemann, and Michael Wiescher. The nuclear reaction waiting points: 22mg, 26si, 30s, and 34ar and bolometrically double-peaked type i x-ray bursts. *The Astrophysical Journal Letters*, 608(1): L61, 2004.

[9] Christopher Sneden, John J Cowan, James E Lawler, Inese I Ivans, Scott Burles, Timothy C Beers, Francesca Primas, Vanessa Hill, James W Truran, George M Fuller, et al. The extremely metal-poor, neutron capture-rich star cs 22892-052: A comprehensive abundance analysisbased on observations made at four facilities:(1) the nasa/esa hubble space telescope (hst), obtained at the space telescope science institute (stsci), which is operated by the association of universities for research in astronomy, inc., under nasa contract nas 5-26555;(2) the keck i telescope of the wm keck observatory, which is operated by the california association for research in astronomy (cara, inc.) on behalf of the university of california and the california institute of technology;(3) the hj smith telescope of mcdonald observatory, which is operated by the university of texas at austin; and (4) the very large telescope of the european southern observatory at paranal, chile, from uves commissioning data and program 165. n-0276 (a). *The Astrophysical Journal*, 591(2):936, 2003.

[10] Alexei V Filippenko. Optical spectra of supernovae. *Annual Review of Astronomy and Astrophysics*, 35(1):309–355, 1997.

[11] G Israelian and M De Groot. P cygni: an extraordinary luminous blue variable. *Space Science Reviews*, 90(3-4):493–522, 1999.

[12] R Pakmor, M Kromer, Stefano Taubenberger, Stuart A Sim, FK Röpke, and Wolfgang Hillebrandt. Normal type ia supernovae from violent mergers of white dwarf binaries. *The Astrophysical Journal Letters*, 747(1):L10, 2012.

[13] Ken'ichi Nomoto and Yoji Kondo. Conditions for accretion-induced collapse of white dwarfs. *The Astrophysical Journal*, 367:L19–L22, 1991.

[14] https://ned.ipac.caltech.edu/level5/March03/Filippenko/frames.html.

[15] SE Woosley and Thomas A Weaver. The evolution and explosion of massive stars. ii. explosive hydrodynamics and nucleosynthesis. *The Astrophysical Journal Supplement Series*, 101:181, 1995.

[16] IA Acharova, Yu N Mishurov, and VV Kovtyukh. Galactic restrictions on iron production by various types of supernovae. *Monthly Notices of the Royal Astronomical Society*, 420(2):1590–1605, 2012.

[17] N Mennekens, D Vanbeveren, and JP De Greve. Progenitors of type ia supernovae and the metallicity distribution of g-type dwarfs. *arXiv preprint arXiv:1212.0313*, 2012.

[18] J Craig Wheeler and Robert P Harkness. Type i supernovae. *Reports on Progress in physics*, 53(12):1467, 1990.

[19] A Reiss, W Press, and R Kirshner. Using type ia supernova light curve shapes to measure the hubble constant astrophys. *J*, 438:L17–L20, 1995.

[20] Mark M Phillips. The absolute magnitudes of type ia supernovae. *The Astrophysical Journal*, 413:L105–L108, 1993.

[21] Mario Hamuy, MM Phillips, Nicholas B Suntzeff, Robert A Schommer, José Maza, and R Aviles. The hubble diagram of the calan/tololo type ia supernovae and the value of ho. *arXiv preprint astro-ph/9609062*, 1996.

[22] Wendy L Freedman, Barry F Madore, Brad K Gibson, Laura Ferrarese, Daniel D Kelson, Shoko Sakai, Jeremy R Mould, Robert C Kennicutt Jr, Holland C Ford, John A Graham, et al. Final results from the hubble space telescope key project to measure the hubble constant based on observations with the nasa/esa hubble space telescope, obtained at the space telescope science institute, which is operated by aura, inc., under nasa contract nas5-26555. *The Astrophysical Journal*, 553(1):47, 2001.

[23] B Leibundgut, R Schommer, M Phillips, A Riess, B Schmidt, J Spyromilio, J Walsh, N Suntzeff, M Hamuy, J Maza, et al. Time dilation in the light curve of the distant type ia supernova sn 1995k. *The Astrophysical Journal Letters*, 466(1):L21, 1996.

[24] Peter M Garnavich, Robert P Kirshner, Peter Challis, John Tonry, Ron L Gilliland, R Chris Smith, Alejandro Clocchiatti, Alan Diercks, Alexei V Filippenko, Mario Hamuy, et al. Constraints on cosmological models from hubble space telescope observations of high-z supernovae. *The Astrophysical Journal Letters*, 493(2):L53, 1998.

[25] Chiaki Kobayashi, Takuji Tsujimoto, Ken'ichi Nomoto, Izumi Hachisu, and Mariko Kato. Low-metallicity inhibition of type ia supernovae and galactic and cosmic chemical evolution. *The Astrophysical Journal Letters*, 503(2):L155, 1998.

[26] Peter Nugent, E Baron, David Branch, Adam Fisher, and Peter H Hauschildt. Synthetic spectra of hydrodynamic models of type ia supernovae. *The Astrophysical Journal*, 485(2):812, 1997.

[27] Paolo A Mazzali, Friedrich K Röpke, Stefano Benetti, and Wolfgang Hillebrandt. A common explosion mechanism for type ia supernovae. *Science*, 315 (5813):825–828, 2007.

[28] Benjamin J Shappee, KZ Stanek, RW Pogge, and PM Garnavich. No stripped hydrogen in the nebular spectra of nearby type ia supernova 2011febased on data acquired using the large binocular telescope (lbt/mods). *The Astrophysical Journal Letters*, 762(1):L5, 2012.

[29] Zhanwen Han and Ph Podsiadlowski. A single-degenerate model for the progenitor of the type ia supernova 2002ic. *Monthly Notices of the Royal Astronomical Society*, 368(3):1095–1100, 2006.

[30] Benjamin J Shappee, CS Kochanek, and KZ Stanek. Type ia single degenerate survivors must be overluminous. *The Astrophysical Journal*, 765(2):150, 2013.

[31] Mario Livio. The progenitors of type ia supernovae. *arXiv preprint arXiv:astro-ph/9903264*, 1999.

[32] Bradley E Schaefer and Ashley Pagnotta. An absence of ex-companion stars in the type ia supernova remnant snr 0509-67.5. *Nature*, 481(7380):164–166, 2012.

[33] R Mochkovitch and M Livio. The coalescence of white dwarfs and type i supernovae-the merged configuration. *Astronomy and Astrophysics*, 236:378–384, 1990.

[34] AM Khokhlov. Delayed detonation model for type ia supernovae. *Astronomy and Astrophysics*, 245:114–128, 1991.

[35] Stanford E Woosley, W David Arnett, and Donald D Clayton. The explosive burning of oxygen and silicon. *The Astrophysical Journal Supplement Series*, 26:231, 1973.

[36] Frank X Timmes, Edward F Brown, and JW Truran. On variations in the peak luminosity of type ia supernovae. *The Astrophysical Journal Letters*, 590(2): L83, 2003.

[37] David A Chamulak, Edward F Brown, and Francis X Timmes. The laminar flame speedup by 22ne enrichment in white dwarf supernovae. *The Astrophysical Journal Letters*, 655(2):L93, 2007.

[38] Dean M Townsley, Aaron P Jackson, Alan C Calder, David A Chamulak, Edward F Brown, and FX Timmes. Evaluating systematic dependencies of type ia supernovae: The influence of progenitor 22ne content on dynamics. *The Astrophysical Journal*, 701(2):1582, 2009.

[39] Eduardo Bravo and Gabriel Martínez-Pinedo. Sensitivity study of explosive nucleosynthesis in type ia supernovae: Modification of individual thermonuclear reaction rates. *Physical Review C*, 85(5):055805, 2012.

[40] Anuj Parikh, Jordi José, Ivo R Seitenzahl, and Friedrich K Röpke. The effects of variations in nuclear interactions on nucleosynthesis in thermonuclear supernovae. *Astronomy & Astrophysics*, 557:A3, 2013.

[41] CL Jiang, BB Back, H Esbensen, RVF Janssens, KE Rehm, and RJ Charity. Origin and consequences of c 12+ c 12 fusion resonances at deep sub-barrier energies. *Physical review letters*, 110(7):072701, 2013.

[42] James Daniel Larson and RH Spear. Gamma radiation from the alpha particle bombardment of c12. *Nuclear Physics*, 56:497–511, 1964.

[43] R Kunz, M Jaeger, A Mayer, JW Hammer, G Staudt, S Harissopulos, and T Paradellis. C 12 (α, γ) o 16: The key reaction in stellar nucleosynthesis. *Physical review letters*, 86(15):3244, 2001.

[44] AS Kachan, IV Kurguz, IS Kovtunenko, VM Mischenko, and VA Panin. Total strength of the magnetic dipole resonance in 31p. *Bulletin of the Russian Academy of Sciences: Physics*, 73(11):1506–1510, 2009.

[45] P Schmalbrock, HW Becker, L Buchmann, J Görres, KU Kettner, WE Kieser, H Kräwinkel, C Rolfs, HP Trautvetter, JW Hammer, et al. Stellar reaction rate of 20 ne (α, γ) 24 mg. *Nuclear Physics A*, 398(2):279–307, 1983.

[46] Carmen Angulo, Marcel Arnould, Marc Rayet, Pierre Descouvemont, D Baye, C Leclercq-Willain, Alain Coc, Slimane Barhoumi, P Aguer, Claus Rolfs, et al. A compilation of charged-particle induced thermonuclear reaction rates. *Nuclear Physics A*, 656(1):3–183, 1999.

[47] Richard Longland, Christian Iliadis, AE Champagne, Joseph R Newton, Claudio Ugalde, Alain Coc, and Ryan Fitzgerald. Charged-particle thermonuclear reaction rates: I. monte carlo method and statistical distributions. *Nuclear Physics A*, 841(1):1–30, 2010.

[48] Christian Iliadis, Richard Longland, AE Champagne, Alain Coc, and Ryan Fitzgerald. Charged-particle thermonuclear reaction rates: Ii. tables and graphs of reaction rates and probability density functions. *Nuclear Physics A*, 841(1): 31–250, 2010.

[49] Christian Iliadis, Richard Longland, AE Champagne, and Alain Coc. Charged-particle thermonuclear reaction rates: Iii. nuclear physics input. *Nuclear Physics A*, 841(1):251–322, 2010.

[50] Christian Iliadis, Richard Longland, AE Champagne, and Alain Coc. Charged-particle thermonuclear reaction rates: Iv. comparison to previous work. *Nuclear Physics A*, 841(1):323–388, 2010.

[51] Richard H Cyburt, A Matthew Amthor, Ryan Ferguson, Zach Meisel, Karl Smith, Scott Warren, Alexander Heger, RD Hoffman, Thomas Rauscher, Alexander Sakharuk, et al. The jina reaclib database: its recent updates and impact on type-i x-ray bursts. *The Astrophysical Journal Supplement Series*, 189(1):240, 2010.

[52] CR Bingham, K van der Borg, RJ de Meijer, and A van der Woude. Structure studies of 23na from the 20ne (α, p) 23na reaction at eα= 39.5 mev. *Nuclear Physics A*, 323(1):26–44, 1979.

[53] SE Hale, AE Champagne, C Iliadis, VY Hansper, DC Powell, and JC Blackmon. Investigation of the na 23 (p, γ) mg 24 and na 23 (p, α) ne 20 reactions via (he 3, d) spectroscopy. *Physical Review C*, 70(4):045802, 2004.

[54] PM Endt. Energy levels of a= 21–44 nuclei (vii). *Nuclear Physics A*, 521:1–400, 1990.

[55] Christian Iliadis, Richard Longland, AE Champagne, and Alain Coc. Charged-particle thermonuclear reaction rates: Iii. nuclear physics input. *Nuclear Physics A*, 841(1):251–322, 2010.

[56] JR Vanhoy, EG Bilpuch, CR Westerfeldt, and Gary E Mitchell. Proton resonances in mg 24 from e x= 12.7 to 15.7 mev. *Physical Review C*, 36(3):920, 1987.

[57] http://www.phy.anl.gov/atlas/facility/.

[58] G Savard, S Baker, C Davids, AF Levand, EF Moore, RC Pardo, R Vondrasek, BJ Zabransky, and G Zinkann. Radioactive beams from gas catchers: The caribu facility. *Nuclear Instruments and Methods in Physics Research Section B: Beam Interactions with Materials and Atoms*, 266(19):4086–4091, 2008.

[59] James E Stevens. Electron cyclotron resonance plasma sources. *High Density Plasma Sources*, pages 312–379, 1995.

[60] B Harss, RC Pardo, KE Rehm, F Borasi, JP Greene, RVF Janssens, CL Jiang, J Nolen, M Paul, JP Schiffer, et al. Production of radioactive ion beams using the in-flight technique. *Review of Scientific Instruments*, 71(2):380–387, 2000.

[61] JC Lighthall, BB Back, SI Baker, SJ Freeman, HY Lee, BP Kay, ST Marley, KE Rehm, JE Rohrer, JP Schiffer, et al. Commissioning of the helios spectrometer. *Nuclear Instruments and Methods in Physics Research Section A: Accelerators, Spectrometers, Detectors and Associated Equipment*, 622(1): 97–106, 2010.

[62] KE Rehm and FLH Wolfs. A focal plane detector for reactions with medium weight projectiles. *Nuclear Instruments and Methods in Physics Research Section A: Accelerators, Spectrometers, Detectors and Associated Equipment*, 273 (1):262–272, 1988.

[63] G Savard, RC Barber, C Boudreau, F Buchinger, J Caggiano, J Clark, JE Crawford, H Fukutani, S Gulick, JC Hardy, et al. The canadian penning trap spectrometer at argonne. In *Atomic Physics at Accelerators: Mass Spectrometry*, pages 223–230. Springer, 2001.

[64] Robert VF Janssens. Gammasphere at atlas: physics at the limits. *Nuclear Physics A*, 685(1):209–220, 2001.

[65] in: I.Y. Lee (Ed.) J.P. Schiffer. 1998.

[66] BB Back, SI Baker, BA Brown, CM Deibel, SJ Freeman, BJ DiGiovine, CR Hoffman, BP Kay, HY Lee, JC Lighthall, et al. First experiment with helios: The structure of b 13. *Physical review letters*, 104(13):132501, 2010.

[67] https://en.wikipedia.org/wiki/Helical_orbit_spectrometer#/media/File:B12_schem.png.

[68] Daniel Jay Blumenthal. A study of cooling following compound nuclear reactions. 1994.

[69] KE Rehm, JP Greene, B Harss, D Henderson, CL Jiang, RC Pardo, B Zabransky, and M Paul. Gas cell targets for experiments with radioactive beams. *Nuclear Instruments and Methods in Physics Research Section A: Accelerators, Spectrometers, Detectors and Associated Equipment*, 647(1):3–9, 2011.

[70] K Kimura, T Izumikawa, R Koyama, T Ohnishi, T Ohtsubo, A Ozawa, W Shinozaki, T Suzuki, M Takahashi, I Tanihata, et al. High-rate particle identification of high-energy heavy ions using a tilted electrode gas ionization chamber. *Nuclear Instruments and Methods in Physics Research Section A: Accelerators, Spectrometers, Detectors and Associated Equipment*, 538(1):608–614, 2005.

[71] KY Chae, S Ahn, DW Bardayan, KA Chipps, B Manning, SD Pain, WA Peters, KT Schmitt, MS Smith, and SY Strauss. Construction of a fast ionization

chamber for high-rate particle identification. *Nuclear Instruments and Methods in Physics Research Section A: Accelerators, Spectrometers, Detectors and Associated Equipment*, 751:6–10, 2014.

[72] William C Sailor and SG Prussin. A model for electron/ion recombination in ionization chambers. *Nuclear Instruments and Methods in Physics Research Section A: Accelerators, Spectrometers, Detectors and Associated Equipment*, 274(1):305–313, 1989.

[73] Bradley Efron and Robert J Tibshirani. *An introduction to the bootstrap*. CRC press, 1994.

[74] Ludovica Sartini, F Simeone, P Pani, N Lo Bue, G Marinaro, A Grubich, A Lobko, G Etiope, A Capone, P Favali, et al. Nuclear instruments and methods in physics research section a: Accelerators, spectrometers, detectors and associated equipment. *Nuclear Instruments and Methods in Physics Research A*, 2010.

[75] Georges Audi, Meng Wang, AH Wapstra, FG Kondev, M MacCormick, X Xu, and B Pfeiffer. The ame2012 atomic mass evaluation. *Chinese physics C*, 36 (12):1287, 2012.

[76] Jonathan C Lighthall. *Commissioning of the Helical Orbit Spectrometer: A new device for measuring nuclear reactions in inverse kinematics*. Ph. D. thesis, Western Michigan University, 2011.

[77] DH Gloeckner, MH Macfarlane, and Steven C Pieper. Ptolemy, a program for heavy-ion direction-reaction calculations. Technical report, Argonne National Lab., 1976.

[78] Haixia An and Chonghai Cai. Global deuteron optical model potential for the energy range up to 183 mev. *Physical Review C*, 73(5):054605, 2006.

[79] AJ Koning and JP Delaroche. Local and global nucleon optical models from 1 kev to 200 mev. *Nuclear Physics A*, 713(3):231–310, 2003.

[80] http://www.nndc.bnl.gov/.

[81] DW Heikkinen and RE Pixley. (d, p) reaction on ne 20. *Physical Review C*, 3 (4):1696, 1971.

[82] SK Datta, GPA Berg, and PA Quin. Coupled-channels and fluctuations analysis of deuteron stripping and deuteron scattering on 20 ne. *Nuclear Physics A*, 332 (1):125–143, 1979.

[83] http://arohatgi.info/WebPlotDigitizer/.

[84] R Abegg and CA Davis. Mg 24 states observed via ne 20 (α, α 0) 20 ne. *Physical Review C*, 43(6):2523, 1991.

[85] Arjan Koning, Stephane Hilaire, and Stephane Goriely. Talys-1.8. 2011.